Radiometric Correction in Range-SPECAN SAR Processing

by

Haleh Hobooti
B.A.Sc. EE., The University of Windsor, 1992

A THESIS SUBMITTED IN PARTIAL FULFILLMENT OF
THE REQUIREMENTS FOR THE DEGREE OF
MASTER OF APPLIED SCIENCE

in

THE FACULTY OF GRADUATE STUDIES
DEPARTMENT OF ELECTRICAL ENGINEERING

We accept this thesis as conforming
to the required standard

THE UNIVERSITY OF BRITISH COLUMBIA
May 1995

In presenting this thesis in partial fulfilment of the requirements for an advanced degree at the University of British Columbia, I agree that the Library shall make it freely available for reference and study. I further agree that permission for extensive copying of this thesis for scholarly purposes may be granted by the head of my department or by his or her representatives. It is understood that copying or publication of this thesis for financial gain shall not be allowed without my written permission.

Department of Electrical Engineering

The University of British Columbia
Vancouver, Canada

Date May 3/1995

Abstract

This thesis investigates the reasons for, and proposes correction methods to reduce the scalloping inherent in the range dimension in images processed using the SPECAN SAR processing algorithm. These corrections methods are successfully tested using ERS-1 satellite data.

The SPECAN algorithm was developed in 1979 by MacDonald Dettwiler and Associates, as a multilook version of the deramp/FFT method of pulse compression. The algorithm provides an efficient method of producing spaceborne SAR imagery of modest resolution, which makes it ideal for quicklook imaging. Widespread use of the algorithm in quicklook imaging, however, is hindered by the scalloping present in both the range and azimuth dimensions of the image.

This thesis concentrates on correction of range scalloping by presenting explanations for the two types of scalloping present in the range dimension of SPECAN processed images. The basic scalloping present in all scenes is due to the time variation in the envelope of the transmitted signal. The extra scalloping seen in some scenes is due to clipping of the ERS-1 raw data.

Because of the geometry of the SPECAN processing cycles, the radiometry of the output is sensitive to the transmitted chirp amplitude. The 0.5 *dB* power difference between the beginning and end of the transmitted chirp is reflected in each compressed output segment, creating a periodic lightening and darkening throughout the image. This banding effect is especially noticeable in low contrast scenes. This problem is corrected using the chirp replica which is embedded in the data header as an estimate of the pulse shape.

The extra scalloping observed in some high reflectivity scenes is attributed to the clipping of the ERS-1 raw data in these scenes. Clipping causes attenuation in the output power. This power loss varies along range according to the degree of saturation, and is different for each compressed data block, thereby creating a discontinuity between adjacent compressed segments

which adds to (or subtracts from) the basic scalloping effect. This problem is corrected using the relationship between power loss and degree of saturation in the Gaussian distributed raw data.

Contents

List of Figures

List of Tables

Acknowledgments

I would like to thank Dr. Ian Cumming for his supervision during this thesis and for recommending this interesting and challenging topic. I also wish to thank Gordon Davidson, Mike Seymour, and Dave Michelson for their technical feedback during the progress of this thesis, and Rick Dorbolo for his valuable suggestions and help in proof reading.

I would like to acknowledge the technical assistance of Paul Lim, Melanie Dutkiewicz and Frank Wong of MacDonald Dettwiler. ERS-1 data has been provided by ESA. Financial support for the work has been provided by the University of Windsor, NSERC, BC Advanced Systems Institute, BC Science Council, and MacDonald Dettwiler.

Chapter 1 Introduction

This thesis concerns an efficient, real-time synthetic aperture radar processing algorithm used for fast processing of radar data in earth imaging applications. The algorithm, Spectral Analysis (SPECAN), was developed for quicklook processing by MacDonald Dettwiler and Associates, Ltd. in 1979 [1], under contract to the European Space Agency [2]. Despite its computational efficiency this algorithm has not had widespread use because images obtained by it show an unacceptable amount of degradation. This thesis investigates the causes for the poor image quality and implements a new method of correcting for the degradation which does not significantly detract from the algorithm's main advantage which is efficiency in computation.

Section 1.1 What is Radar Remote Sensing?

Remote sensing, as explained by Wall, et al. [3], refers to the monitoring of the earth's surface or atmosphere from a distant location. Remote sensing can be performed either *passively* or *actively*. Passive systems do not provide target illumination, but operate by measuring the amount of a certain type of radiation from the earth's surface or atmosphere (Hovannessian [4]). The most useful passive remote sensing tools are optical multispectral sensors which operate in the visible and infrared regions. Such systems need only to be equipped with a receiver. Active systems, such as laser and radar imaging systems, provide a controlled source of target illumination. These systems must be equipped with both transmitter and receiver.

A potentially very useful active imaging tool is the synthetic aperture radar, which operates by transmitting a microwave beam, receiving, and measuring the strength and time delay of the echo from the surface. The power returned is a function of the *reflection coefficient* of the ground and depends on the geometric and dielectric properties of the medium (see Rees [5, p. 61]. Digital signal processing techniques are used on the returned signal to extract the ground

reflectivity map. The image obtained in this manner is a function of the physical properties, including orientation, roughness, topography, and moisture content of the objects on the imaged surface.

Optical systems are widely used because of the very high resolution they provide. Optical images are a measure of the chemical composition of the imaged surface. However, they are useless at night and through cloud cover. Microwaves are not affected by atmospheric moisture, making them ideal for imaging planet surfaces through cloud cover. In the Magellan mission, as described by Johnson [6], a synthetic aperture radar was used to image the surface of Venus through its very dense atmosphere.

Radar remote sensing by satellite offers wide coverage of land at fixed intervals regardless of weather, clouds or time of the day. The European Remote-Sensing satellite (ERS-1), for example, has different orbital patterns with repeat periods of 3, 35, and 176 days where each individual orbit in the pattern will last approximately 100 minutes, Francis, et al. [7, p. 28]. This includes coverage of areas which are inaccessible by other means due to political, or geographical difficulties.

1.1.1 Real Aperture Radar

Radar has been used for many years in military applications for tracking targets, in air traffic control, speed measurement and other uses. From military applications the term "target" has been used to refer to the aircraft or ship being tracked. In remote sensing, "target" refers to the area of ground from which the backscatter is received. A radar (as described by Tomiyasu [8]) is an electromagnetic wave sensor having a pulsed microwave transmitter, antenna and receiver. The antenna can be time shared between the transmitter and receiver. A pulse is transmitted, reflected off the target and received. The antenna is carried by the aircraft and produces a fan beam to the side of the flight track.

In real aperture radar (RAR) the antenna is unfocused because the receiver does not accurately conserve the phase of each reflected pulse. For this type of imaging system a high resolution will be obtained by transmitting a very narrow beam, or effectively, by having a small wavelength, large antenna, and smallest possible distance to target. Wavelengths of microwave beams are from 3 *cm* to 30 *cm*, and the distance from the satellite to ground is on the order of hundreds of kilometers. Thus the only way to increase the resolution is to increase the size of the antenna.

The resolution of both RAR and optical systems is of the order of the beamwidth, $\lambda R/l$, where R is the range to the target, λ is the wavelength, and l is the diameter of the antenna aperture or lens (Ulaby [9, p. 651]). For example, for a resolution of *100 m*, with $\lambda = 0.03$ *m* and $R = 700$ *km*, the antenna length would have to be approximately *200 m*! Such an antenna would be extremely costly, and would have power and stability problems in space. Optical systems, however, acquire good resolution with reasonable sized antennas because of the very small wavelength of the electromagnetic energy, Elachi [10].

1.1.2 Synthetic Aperture Radar

The principles of synthetic aperture radar (SAR) were first introduced by Carl Wiley in 1951 with the observation that a radar carried on board a moving platform with its beam oriented at an angle to the platform velocity would receive signals which are offset from the radar frequency due to the motion of the radar which causes the Doppler effect. By filtering this signal the beamwidth can be made effectively narrower (or equivalently, the aperture will be longer). This technique enables very high resolution images to be obtained without a need to increase the antenna's physical size.

In SAR the demodulation of the signal return to baseband is performed very accurately to conserve the phase between adjacent samples. This phase history is used to filter the data in the along-track dimension, whereas in RAR filtering is only performed in the across-track dimension.

1.1.3 Other Uses of SAR Data

Besides two-dimensional terrain imaging, SAR data is used in *polarimetry* and *interferometry*. Polarimetry is based on the principle that different types of terrain and ground cover have different radar reflectivity based on the polarization of the transmitted beam. Most SAR antennas are linearly polarized, that is, they send and receive the same polarization. In polarimetric SAR the complete polarization response of the target is measured by interleaving orthogonally polarized radar pulses on transmission and measuring the amplitude and phase of the co-polar and cross-polar returns on reception. The ratio of like to cross polarized return can be used to extract significant geophysical and biophysical parameters such as surface roughness, moisture content of soil, biomass content of a forest, or thickness of thin sea ice. For a detailed discussion on the applications of polarimetry to geoscience refer to Ulaby, et al. [11].

Interferometry is the process of estimating terrain topography from SAR images by using two complex images of the same scene taken from different angles. After the images have been shifted appropriately to align identical points, the phase difference between the two images (called the interferogram) is calculated and used along with other parameters such as the angle and position shift of the sensor to calculate the height of each pixel. For more explanation on interferometry refer to Graham, et al. [12], and Zebker, et al. [13].

1.1.4 Summary of Advantages and Disadvantages of SAR Imagery

Some advantages of a microwave imaging system can be listed as:

- Continuous coverage (at night and through cloud cover).
- Continuous, homogeneous coverage of large areas which would not be possible by other means. That is, SAR imagery provides the "big picture".
- High resolution imagery is obtainable independent of radar distance to target.
- Controlled polarization allows classification of features.

- Terrain height estimation is possible by interferometry. This is especially useful for snow covered mountainous areas where terrain height cannot be "seen".
- Some features are distinguished only by a microwave beam. For example, ancient drainage channels under desert sand would not have been detected by an optical system. Also, the microwave beam will provide a picture of the physical surface roughness which is useful in distinguishing such things as effects of erosion and different land coverage.

Some disadvantages are as follows:

- Images are degraded by speckle. (Speckle noise is a result of the coherent reflection from each point target in the resolution cell adding constructively or destructively in a random fashion; multilooking will reduce speckle at the expense of resolution, see Ulaby [9, p. 585], and Kirk [14]).
- The resolution is not as high as can be achieved in an optical system.
- Some visible features are not easily noticed because they are imaged differently from an optical system. For example, mountain ranges perpendicular to the flight path will not be recognizable as such.
- SAR does not measure the chemical properties of the surface. For example, healthy and rotten vegetation is imaged identically, whereas Landsat-type sensors can distinguish them by their different infrared reflectivity.
- Geometric distortion in the range dimension. For example, if two points are located (for example on a slope) such that the range from radar to both points is the same they will be registered as the same point.

In summary, the type and scale of the phenomenon to be studied will determine the optimum choice of sensor, platform, and operational parameters used. Figure 1.1, adapted from Rees [5, p. 173], illustrates this by showing a short summary of various applications and their requirements in terms of repeats per day and resolution.

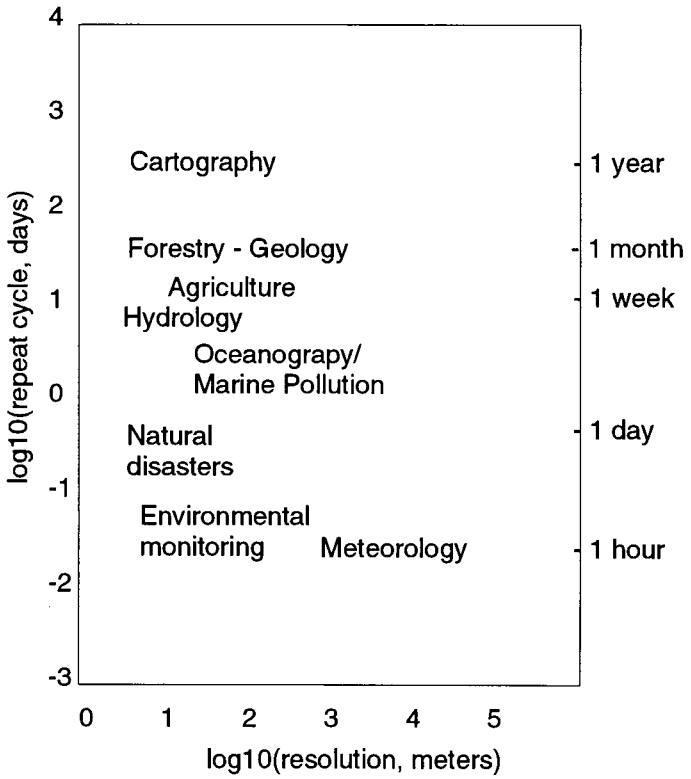

Figure 1.1 Observational requirements for various applications

Section 1.2 Thesis Overview

The remainder of this thesis is organized as follows. Chapter 2 will describe the basic geometry of the SAR system. SAR image formation is described and the basis of pulse compression is explained. The fast convolution method of SAR compression and the deramp/FFT methods are both briefly explained.

Chapter 3 describes the motivation and details of the Spectral Analysis (SPECAN) algorithm, both mathematically and graphically. The efficiency advantages of SPECAN are compared with fast convolution.

Chapter 4 describes and shows examples of the degradation in SPECAN processed images. The cause of the problem is analyzed using the geometry of the SPECAN algorithm and a correction function is derived. The correction is tested in a point target simulation.

Chapter 5 derives the correction vector corresponding to the ERS-1 satellite SAR. The correction is then tested on real SAR data and its performance evaluated on different types of terrain. In some scenes residual scalloping remains after the basic correction.

Chapter 6 analyses the impact of raw data saturation on SPECAN image quality and the residual scalloping. A theory is formed to explain the effect of raw data saturation on scalloping, and the results of a raw data simulation are presented which verify the theory. A correction scheme is proposed and tested on the worst case of saturation seen in Chapter 5.

Chapter 7 will provide a summary and describe the significance of this work. Also, methods to reduce saturation are proposed, and the need for a practical implementation of the method is discussed.

Chapter 2 Fundamentals of Synthetic Aperture Radar

This chapter explains the basic geometry of the SAR system, the mathematical form of the ideal received SAR signal, the basis of pulse compression, and current signal processing methods used to generate an image from SAR raw data.

Section 2.1 SAR Components

The main components of the SAR system are the antenna, pulsed transmitter, and coherent receiver, carried on a platform which is either a satellite, or an airplane. The satellite or airplane carrying the SAR antenna moves across the surface of the earth at a constant velocity while transmitting microwave pulses at regular intervals and receiving the returned pulse.

The boresight of the antenna is aligned perpendicular to the flight path, and to one side of the platform. The direction of travel of the antenna is called the *azimuth* direction. The direction of travel of the transmitted pulse is referred to as the *range* direction (which is perpendicular to the direction of travel). Pulses are transmitted at the *pulse repetition frequency* (PRF) and the echo is received and stored for processing. The received data can be modelled as a matrix where each row is the echo from one transmitted pulse. These transmissions build up in the azimuth direction to form the matrix. Each row, or pulse echo, is a function of *fast time, t*, and each column is a function of *slow time,* η. The image is formed by measuring the range distance of the echo. Because the antenna and the imaged swath are on different planes, the distance measured is in *slant range* as seen in Figure 2.1.

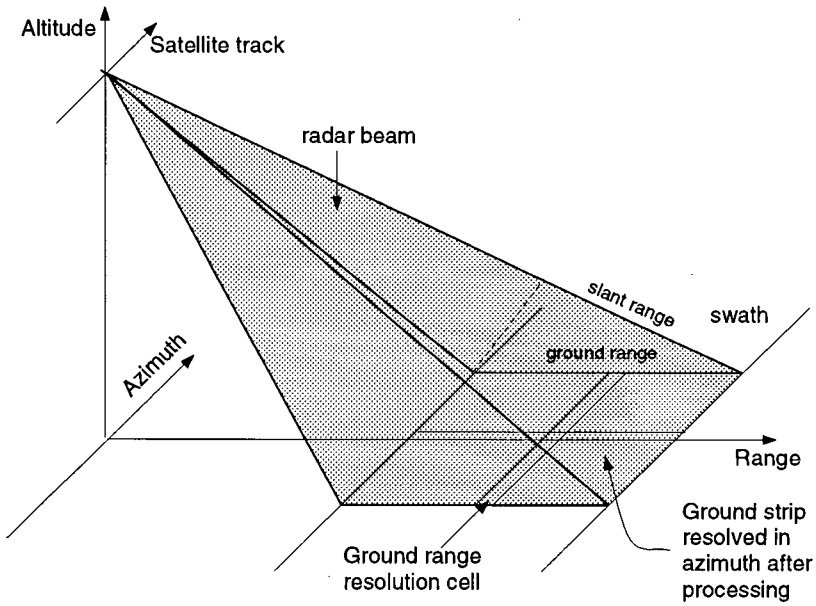

Figure 2.1 Synthetic aperture radar geometry.

The data used in this thesis was acquired by the ERS-1 satellite. In describing the physical components of a SAR system, we will use the example of the ERS-1 active microwave instrument as described by Brooks, et al. [15], Francis et al. [7], and Austin, et al. [16]. Figure 2.2, adapted from Francis et al. [7, p. 41], shows the block diagram of the instruments constituting the ERS-1 SAR.

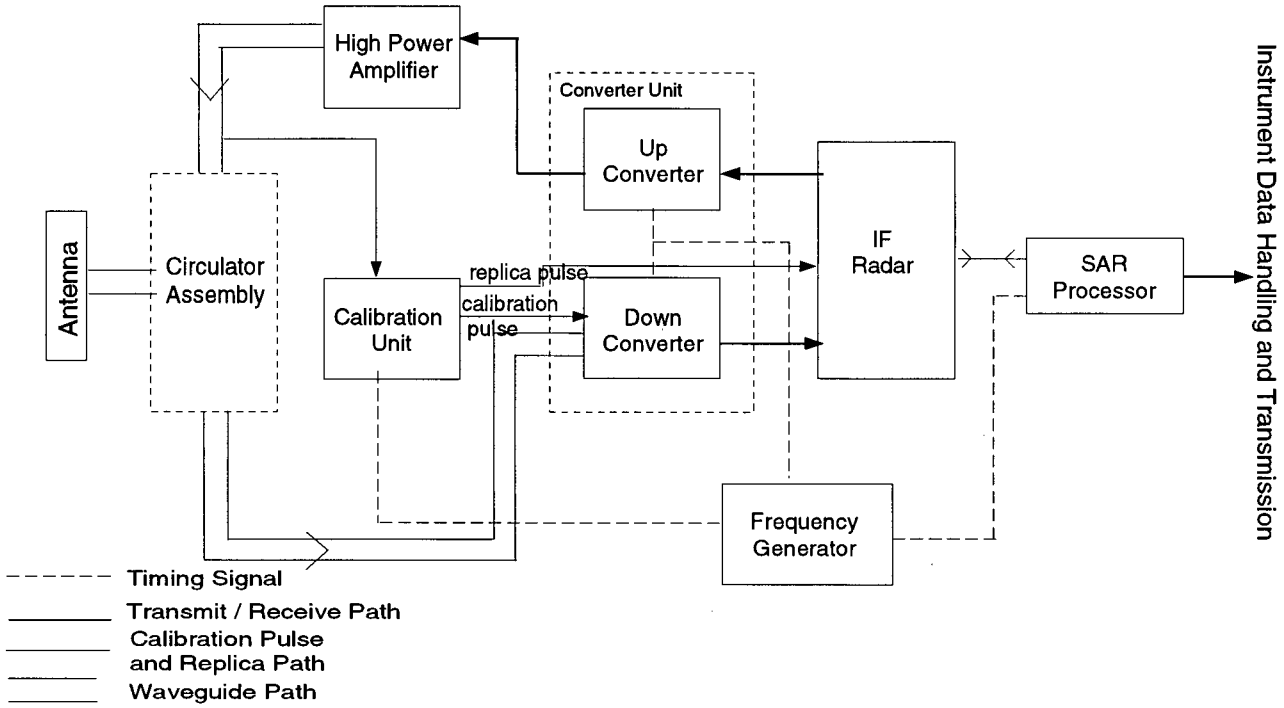

Figure 2.2 SAR system onboard satellite or aircraft

In the SAR imaging mode the transmit timing pulse is obtained from the SAR processor and provided to the intermediate frequency (IF) radar. The IF radar produces a linear frequency modulated (FM) pulse[1]. This pulse is fed to the up-converter to produce the radio frequency signal which is fed to the high power amplifier. The circulator assembly routes the signal to the SAR antenna. In the receive path the signal is downconverted to baseband, quantized and either sent to a ground station, or recorded for future transmission.

Section 2.2 The SAR Signal

As explained by Munson, et al. [17] the radar signal must be a pulse with enough power that the received signal has good signal-to-noise ratio. An impulse like waveform would have these qualities, but would require very high peak power. In SAR systems a large bandwidth dispersed-energy pulse is transmitted and the received signal is processed to a narrow pulse by a

[1] By means of a surface acoustic wave (SAW) device.

method called *pulse compression.* The waveform generally used for transmission is the linear FM chirp. A study has been done by Marcus, et al. [18] in using a coherent laser pulse instead of a linear FM chirp in a one-dimensional SAR, however this work is still in the experimental stages.

The two-dimensional point target equation will be developed in the following sections. The point target equation is the recieved signal if only one scatterer were present on ground. The SAR is a linear system to which the principle of superposition applies, therefore the process developed for a point target can be applied to the real recieved signal where the received signal is modelled as the sum of many point targets.

The Azimuth Signal In real aperture radar, the transmitted pulse must be very narrow in order to illuminate each target separately. Because the beam widens with distance, the resolution in the azimuth direction will also depend on the distance between sensor and target. SAR takes advantage of the fact that the motion of the antenna with respect to ground causes each target to have a different Doppler signature with respect to adjacent targets. By using digital signal processing the different Doppler signals can be resolved to form a narrow pulse at the location of each target. This has been covered in more detail by Curlander [19], Bonfield, et al. [20], and Tomiyasu [8].

Figure 2.3 shows how the range of a target to the radar changes as the beam passes over the target. Note that the perspective of this figure is a position above the satellite.

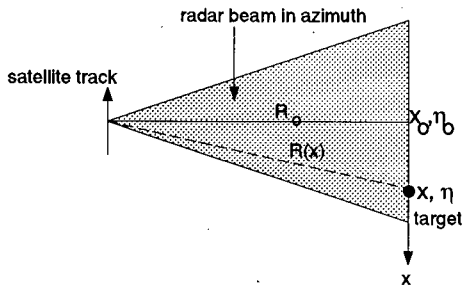

Figure 2.3 Doppler frequency determination

As the target passes through the radar beam the range distance, and therefore the phase of the received signal from the target changes. It is this change in phase with respect to time that constitutes the Doppler frequency. The simple expression for the Doppler frequency ignoring the effects of earth curvature and motion is derived as follows.

From the geometry of Figure 2.3, the target is at its closest range, R_o, to the satellite at time $\eta = \eta_o$. When the target is at some arbitrary position x with respect to the satellite, the separation $R(x)$ is calculated as:

$$R(x) = \left[(x - x_o)^2 + R_o^2\right]^{1/2} \tag{2.1}$$

From the satellite velocity, V_s, the distance can be written as $(x - x_o) = V_s(\eta - \eta_o)$, where η is the time variable corresponding to the position x. Because $R_o >> (x - x_o)$ equation (2.1) can be written using the first two terms of the binomial series:

$$R(\eta) \simeq R_o + \frac{V_s^2(\eta - \eta_o)^2}{2R_o} . \tag{2.2}$$

The phase, $\phi_a(t)$, of the returned signal in azimuth is:

$$\phi_a = \frac{-4\pi R(\eta)}{\lambda} . \tag{2.3}$$

The Doppler frequency, $\omega_D(\eta)$, is the rate of change of the phase with time:

$$\omega_D(\eta) = \frac{d\phi_a(\eta)}{d\eta} \simeq \frac{-4\pi V_s^2(\eta - \eta_o)}{\lambda R_o} \quad rad/s \tag{2.4}$$

So the received signal in the azimuth dimension is a linear chirp centered on zero frequency. The FM rate of this signal, K_a, will be:

$$K_a = \frac{-2V_s^2}{\lambda R_o} \tag{2.5}$$

The value of R_o changes for each range bin, therefore the FM rate of the azimuth signal changes also, and this must be taken into account when processing the data from different range locations.

The Range Signal The signal reflected from a point target is a delayed version of the transmitted signal. This delay, t_d, is calculated as

$$t_d = \frac{2R(\eta)}{c} , \tag{2.6}$$

where $R(\eta)$ is the range from the antenna to the target at time η, and c is the speed of light. The phase of the received range signal will be:

$$\phi_r(t) = \pi K_r (t - T_c/2 - t_d)^2 , \tag{2.7}$$

where K_r is the FM rate of the radar transmit pulse, t is the fast time variable, and T_c is the pulse length.

From the above discussion we can write the ideal received SAR signal from a point reflector as a two dimensional signal:

$$s(\eta, t) = A(\eta - \eta_o) P(t - t_d) exp\left(\frac{-j4\pi R(\eta)}{\lambda} + j\pi K_r (t - T_c/2 - t_d)^2 \right) , \tag{2.8}$$

where A is the azimuth antenna pattern and P is the pulse envelope in the range dimension.

Section 2.3 SAR Processing

As discussed in section 2.2, the SAR raw data matrix in both range and azimuth can be modelled as the convolution of a linear FM chirp and the ground reflectivity. Using the form of the ideal received signal in equation (2.8) a matched filter can be derived for each dimension and pulse compression can be performed on the rows and columns of the raw data.

Pulse compression rearranges the energy received from each ground reflector into a single focused pulse, where the location of maximum energy coincides with the location of the target in slant range, and the strength of the signal represents the reflectivity of the target. This is accomplished using a matched filter. In effect, the matched filter deconvolves the received signal and extracts the ground reflectivity map from noise with minimum mean-squared error.

2.3.1 The Matched Filter

The matched filter is derived as the conjugate of the time reversed ideal received signal. For a transmitted signal, *s(t)*, the echo, *r(t)*, is received after a delay t_d (see Equation 2.6):

$$r(t) = \alpha s(t - t_d) + n(t) \,, \tag{2.9}$$

where *n(t)* is white noise, and α is the attenuation. The matched filter is derived as a signal which when convolved with *r(t)* extracts the input with the highest possible power above noise. This is found to be the time-reversed conjugate of the transmitted signal, that is, $s^*(-t)$. The compressed output, *y(t)*, is the convolution of the matched filter and the received signal:

$$y(t) = \int_{-\infty}^{\infty} r(t - t_d)s^*(-t_d)d\tau \tag{2.10}$$

For details of the derivation refer to Curlander [19] and Levanon [21]. Because the slow and fast times are orders of magnitude different, two matched filters are derived using the range and azimuth parameters of the radar, respectively, and the received signal can be processed in two independent stages.

Range Resolution The result of applying the range matched filter to the point target of equation (2.8) is a compressed pulse of envelope *p(t)*:

$$p(t) = K_r T_c \frac{sin(\pi K_r T_c t)}{\pi K_r T_c t} \,, \tag{2.11}$$

where K_r is the range FM rate, and T_c is the time duration of the transmitted pulse. The resolution, δ_r, is measured as the 3 *dB* width of this signal:

$$\delta_r \simeq \frac{1}{K_r T_c} \,, \tag{2.12}$$

where $K_r T_c$ is the bandwidth of the transmitted pulse. This indicates that a pulse of time span T_c seconds is compressed by the time-bandwidth product, $K_r {T_c}^2$. Increasing the average

power will boost the signal to noise ratio, while increasing the bandwidth will produce finer resolution imagery. The main sidelobes of the compressed pulse are approximately 13 *dB* below the mainlobe; various windowing methods are used to reduce the sidelobes, at the expense of broadening the mainlobe width and decreased resolution. For a study of various window functions and their properties refer to Nuttal [22].

Azimuth Resolution The azimuth resolution in real aperture radar is only equal to the along track length of ground illuminated by the beam. As the antenna distance to ground is increased, the beam widens, and therefore the azimuth resolution becomes coarser. In SAR, however it can be shown that the azimuth resolution of a fully focused synthetic aperture is independent of sensor distance to target and wavelength.

By using the matched filtering technique on the azimuth signal the resulting resolution will be of the order of the inverse of the bandwidth. The ratio of bandwidth to time duration of a linear FM pulse is the FM rate of the signal, $K_a = BW/T$. The time duration of the azimuth signal is the time during which the target is illuminated by the radar beam and is calculated as $T = \lambda R_o/V_s D$. Using the FM rate of the azimuth signal from equation (2.5), the bandwidth can be calculated:

$$BW = \frac{2V_s}{D} \quad Hz \tag{2.13}$$

Therefore the resolution, δ_a, is:

$$\delta_a \simeq \frac{D}{2} \quad m \tag{2.14}$$

Fast-Convolution The fast-convolution method is the frequency domain implementation of the matched filter convolution process and is explained by Bennett, et al. [23] and Wu, et al. [24]. This method is used as a benchmark to evaluate other compression methods in terms of resolution and amount of computation required.

Equation 2.10 is implemented in the frequency domain as:

$$Y(\omega) = R(\omega)S^*(\omega) \tag{2.15}$$

and the time-domain output is the inverse Fourier transform of $Y(\omega)$.

Figure 2.4 shows the simplified block diagram of the fast convolution process.

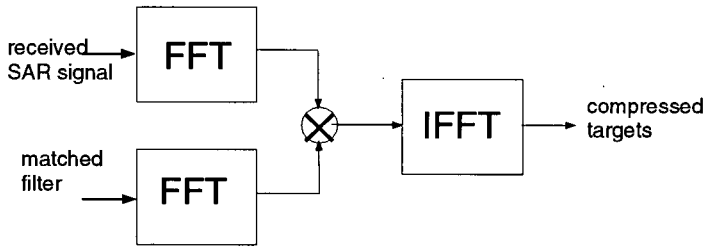

Figure 2.4 Fast-convolution

Spectral Analysis This method, also known as the *deramp-FFT* method, takes advantage of the quadratic phase of the chirp by mixing the received target and the matched filter in time, and applying short length FFTs to the constant frequency (*deramped*) signal. This method has been briefly explained by Munson, et al. [17], Elachi, et al. [10], and Chunsheng [25]. To be computationally efficient, this method can only achieve up to two-thirds the resolution of the fast-convolution method. The next chapter will explain this algorithm in detail.

Figure 2.5 shows the block diagram of the Spectral Analysis process on one line of raw data.

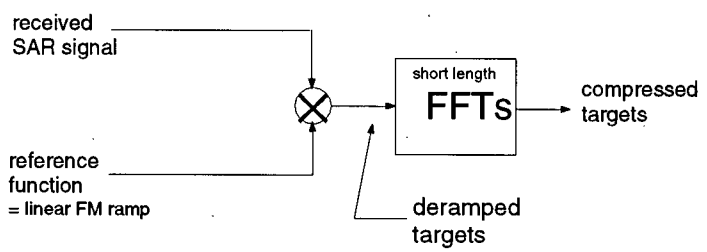

Figure 2.5 Deramp-FFT

It must be mentioned that although satellite and airborne processing principles are identical, processing of satellite SAR data is generally more complicated. This is because the very high altitude of the satellite causes a larger area to be under illumination for a longer period of time, therefore the movement of the target as a result of earth rotation must be taken into account. Also, the effect of *range migration* must be corrected in satellite imagery. For more details on range migration effects the reader is refered to Tomiyasu [8].

2.3.2 Radar Performance and Post-Processing

The radar performance is measured by examination of its impulse response. The impulse response is the output of the system when the input is the signal from a single reflector. This can be done by examining the point targets in the SAR image. The point targets are either natural (eg. ships in the ocean) or man-made objects with known reflection coefficients. The following parameters are measured on the image point targets and compared with the theoretical values [19, p. 256], [26].

1. Mainlobe broadening (the actual 3 *dB* width, compared with the value calculated assuming no system errors).
2. The Integrated Sidelobe Ratio (ratio of sum of point target sidelobes to the 3 *dB* area of the mainlobe).
3. Peak Sidelobe ratio (ratio of the largest sidelobe outside the mainlobe to the mainlobe peak).

Post-processing of the image usually consists of *radiometric* and *geometric* corrections. Geometric correction involves relating the spatial coordinates on the image to the corresponding coordinates on the ground. This is done by using the location of known targets on ground and resampling the image to new coordinates.

Radiometric correction is required to establish a relationship between the detector output and the input radiation intensity. The radiometric correction function as described by Curlander [19,

p. 477] is a scalar array which varies with range image pixels. This function depends on factors such as the antenna pattern, slant range, resolution cell size and system gain/losses. In this thesis, however, we are only concerned with correction of *scalloping*, which is the radiometric degradation specific to SPECAN images.

Chapter 3 The Spectral Analysis Method of SAR and Quicklook Processing

This chapter explains the motivation for developing SPECAN followed by the details of the algorithm as explained in the 1979 MDA report [1]. A comparison is made between the resolution of targets in the fast convolution versus the SPECAN method, and the limitations of SPECAN are reviewed.

Section 3.1 Motivation

In conventional SAR processing methods the signal is range compressed using the fast convolution method. As will be explained in detail later in the chapter, the SPECAN method will reduce the computation time required for each range line processing by approximately a factor of eight. This makes the algorithm suitable for use in on-board real-time processors and quicklook ground processors. The trade-off is that the resulting SPECAN image will have up to two-thirds the resolution of a fast convolution image of the same scene. This trade-off makes the algorithm suitable for applications where lower resolution is acceptable, such as real-time monitoring of ocean oil slicks, ship positions, and ice formations.

A real-time SAR processor breadboard has been developed (see Schotter [27], and the MDA report [28]) which uses the SPECAN algorithm for azimuth compression. Also, a SAR processor (the Brazil Quicklook processor) has been developed by MDA which uses the SPECAN algorithm for both range and azimuth compression (MDA report [29]). The rather limited use of the algorithm has been due to the image quality problems which will be dealt with in the next chapter.

Section 3.2 Explanation of the Method

This section explains the SPECAN algorithm in detail. The algorithm can be used for both range and azimuth compression. Most of the problems regarding azimuth-SPECAN image quality have been solved by an accurate estimation of the Doppler centroid, see Wong, et al. [30]. Range-SPECAN has similar problems which are still unsolved and which render the algorithm unsuitable for use. Since this thesis was aimed at solving the range-SPECAN problems, the following sections emphasize range processing.

SPECAN performs target compression in two stages. The first operation is called *deramping*. In this stage the received signal will be transformed from a linear FM signal to a constant frequency signal, that is, the phase of the received signal is transformed from quadratic to linear. The constant instantaneous frequency of the deramped signal will be proportional to the time position of the signal. In the second stage, *DFT operations*, short length DFT's across the constant frequency signal compress most of the energy of each target into a single frequency bin. The output of the SPECAN processor is the output of the DFT operations, and therefore must be resampled to represent the input range correctly. Each of these operations will be explained in greater detail below.

3.2.1 Deramping

The concept of deramping in the time domain is derived from the stretch technique [31]. The stretch technique allows linear manipulation of the time and bandwidth coordinates of a linear FM signal by means of mixing with another signal of different frequency-time slope in order to slow down, speed up, or time reverse the signal.

A linear FM signal has the following form:

$$s(t) = e^{j\pi K(t-\tau_c)^2} \qquad -\frac{T_c}{2} \leq t < \frac{T_c}{2} \tag{3.1}$$

where K is the FM rate of the signal, T_c is the time extent of the pulse, and τ_c is the time position of the zero frequency of the signal. The zero frequency of the target is the static phase point, the time at which the phase rate goes from positive to negative (or vice versa). If the phase switch-over occurs in the middle of the signal time duration, the zero frequency will coincide with the centre frequency.

The instantaneous frequency of a linear FM chirp is equal to the derivative of its phase, θ. The phase, $\theta_s(t)$, and instantaneous frequency, $\omega_{inst}(t)$, of the signal in 3.1 will be:

$$\begin{aligned} \theta_s(t) &= \pi K(t-\tau_c)^2 \\ \omega_{inst}(t) &= \frac{d\theta_s(t)}{dt} = 2\pi K(t-\tau_c) \end{aligned} \tag{3.2}$$

The instantaneous frequency is a linear function of time.

If the signal in Equation (3.1) is multiplied with another linear FM signal $s_1(t)$ which has a different FM rate K_1, and is shifted in time with respect to $s(t)$, the product will be a linear FM signal with FM rate $(K+K_1)$.

$$\begin{aligned} s_1(t) &= e^{j\pi K_1(t-\tau_r)^2} \qquad -\frac{T_c}{2} \le t < \frac{T_c}{2} \\ s(t)s_1(t) &= e^{j\pi(K+K_1)t^2} e^{-j2\pi(K\tau_c+K_1\tau_r)t} e^{j\pi\left(K\tau_c^2+K_1\tau_r^2\right)} \end{aligned} \tag{3.3}$$

The first term on the right hand side of Equation 3.3 represents a linear FM signal with FM rate equal to $(K+K_1)$. The second term is a constant frequency signal, and the third term is a constant complex number.

In SPECAN the same technique is applied. However, to transform the targets from linear FM chirps into constant frequency signals K_1 is chosen to be $-K$. The resulting deramped signal, $d(t)$, will be

$$d(t) = e^{2j\pi K(\tau_r-\tau_c)t} e^{j\pi K\left(\tau_c^2-\tau_r^2\right)} \tag{3.4}$$

The phase, $\theta_d(t)$, and instantaneous frequency, $\omega'_{inst}(t)$ of the deramped signal will be:

$$\theta_d(t) = \pi K\left[2(\tau_r - \tau_c)t + (\tau_c^2 - \tau_r^2)\right]$$
$$\omega'_{inst}(t) = 2\pi K(\tau_r - \tau_c)\,, \tag{3.5}$$

where we can see that $\omega'_{inst}(t)$ does not vary with time.

In SPECAN the FM rate of the transmitted pulse is used to generate the conjugate of the ideal received signal which then deramps the received data by a complex multiplication in the time domain. The generated function is the SPECAN matched filter and is called the *reference function.*

3.2.2 DFT Operations

After deramping, each target will have a constant frequency value proportional to the time position of its zero Doppler frequency with respect to that of the reference function as seen from Equation (3.5). A DFT performed on this signal will confine most of the energy of each target to a single frequency bin. The relative positions of these detected energies in the frequency domain will be proportional to the relative positions of the targets' time locations, therefore the targets will be detected at the correct positions relative to each other. Short length DFT blocks will be placed along the deramped signal such that each target's trajectory is included in at least one DFT input vector. The DFT block placement will be explained in more detail later in the chapter.

3.2.3 Analytical Representation

As we saw in Chapter 2 compression of radar signals is accomplished by cross correlating the received signal with the conjugate of the ideal received signal. In this section we will show that the cross correlation operation is equivalent to deramping followed by a DFT operation.

The ideal received signal is a linear FM signal of the form

$$s_{ideal}(n) = e^{-j\pi K_r(n\tau)^2} \qquad \frac{-N}{2} \leq n < \frac{N}{2}\,, \tag{3.6}$$

where

Kr = FM rate of ideal received signal [Hz/s]

N = number of samples in ideal received signal

τ = sample spacing [s]

The compressed output, *y(n)* is derived by cross correlating the received signal, *s(n)* (linear FM plus noise), and the conjugate of the ideal received signal, $r(n)=s_{ideal}^{*}(n)$.

$$\begin{aligned} y(n) &= \sum_{i=-\frac{N}{2}}^{\frac{N}{2}-1} s(i)r(i+n) \\ &= \sum_{i=-\frac{N}{2}}^{\frac{N}{2}-1} s(i)e^{j\pi K_r(n+i)^2\tau^2} \\ &= \sum_{i=-\frac{N}{2}}^{\frac{N}{2}-1} s(i)e^{j\pi K_r\left(n^2+i^2+2ni\right)\tau^2} \end{aligned} \tag{3.7}$$

Multiplying the right-hand side of Equation (3.7) by $e^{j\pi K_r\tau^2 nN}e^{-j\pi K_r\tau^2 nN}$ will result in:

$$\begin{aligned} y(n) &= e^{j\pi K_r n^2\tau^2}e^{-j\pi K_r\tau^2 nN}\sum_{i=-\frac{N}{2}}^{\frac{N}{2}-1} s(i)e^{j\pi K_r\tau^2 i^2}e^{2j\pi K_r\left(ni\tau^2+\tau^2 nN/2\right)} \\ &= e^{j\pi K_r\tau^2\left(n^2-nN\right)}\sum_{i=-\frac{N}{2}}^{\frac{N}{2}-1} s(i)e^{j\pi K_r\tau^2 i^2}e^{2j\pi K_r n\tau^2(i+N/2)} \end{aligned} \tag{3.8}$$

The first term in the right-hand side of Equation (3.8) is a phase rotation term and can be ignored if the next operation is the detection operation which removes the phase information.

The second term on the right of the summation is the conjugate of the ideal received signal, *r(n)*. Therefore Equation (3.8) can be rewritten as

$$y(n) = \sum_{i=-\frac{N}{2}}^{\frac{N}{2}-1} s(i)r(i)e^{2j\pi K_r \tau^2 (i+\frac{N}{2})} \tag{3.9}$$

If the product of the signal and its complex conjugate is denoted by $p(n) = s(n)r(n)$, by a change in limits the output can be written as:

$$y(n) = \sum_{i=0}^{N-1} p\left(i - \frac{N}{2}\right) e^{2j\pi K_r n \tau^2 i} \tag{3.10}$$

The number of samples in the reference function is $N = F^2/K_r$. Substituting for K_r in Equation (3.10) we can further simplify the compressed output.

$$\begin{aligned} y(n) &= \sum_{i=0}^{N-1} p\left(i - \frac{N}{2}\right) e^{2j\pi in/N} \\ &= e^{j\pi n} \sum_{i=0}^{N-1} p(i) e^{2j\pi in/N} \end{aligned} \tag{3.11}$$

The $e^{j\pi n}$ term before the summation is a phase rotation term which again can be ignored if the next operation is detection. Equation 3.11 shows that the result of cross-correlating the input signal with the conjugate of the ideal received signal is equivalent to performing a DFT on the product of the received signal and the reference function. The above derivation can only be carried out if the signals have a linear FM form. Therefore the SPECAN algorithm is only valid for linear FM signals.

3.2.4 Graphical Representation

Greater understanding of the SPECAN method is possible by graphically examining the deramping and DFT operations. This section will use the geometry of point reflectors as they undergo SPECAN compression operations to show how the algorithm determines target location.

In SAR the time-bandwidth product[1] of the transmitted signal is usually higher than 100. Thus the principle of stationary phase can be used to simplify the relationship between the time (T) and instantaneous frequency (f) of the linear FM signal as

$$f = KT \tag{3.12}$$

This one-to-one correspondence between time and frequency allows the linear FM signal to be well represented in the frequency-time plane which will be used extensively in the following sections.

Deramping This section shows the deramping operation with the aid of Figure 3.1. The receiver sampling rate is greater than the Nyquist rate of the received signal. The reference function is generated using the same FM rate as the transmitted pulse, but with bandwidth equal to the sampling frequency. Therefore, according to Equation (3.12), the reference function will have a longer time duration than the received point reflector as demonstrated in Figure 3.1a.

If the target and reference function had equal time locations for their zero Doppler frequencies the frequency of the product would be zero Hz. This would be the case in Equation (3.4) for $\tau_c = \tau_r$. In this case the equation of the deramped target would simplify to $d(t) = 1$. In the general case, however, the zero Doppler frequency of the target is displaced in time from that of the reference function, and the resulting product has a non-zero constant frequency (as seen in Figure 3.1d) proportional to the displacement as seen in Equation (3.4).

---

[1] The time-bandwidth product is the product of the duration of the dispersed pulse and its bandwidth.

Because the target is shifted in time with respect to the reference function, the reference function is repeated in time to encompass the entire length of the target. This causes a frequency shift of y $\pm F$ in the deramped target, where F is the sampling frequency. Aliasing by $\pm F$ will restore the signal to f_d.

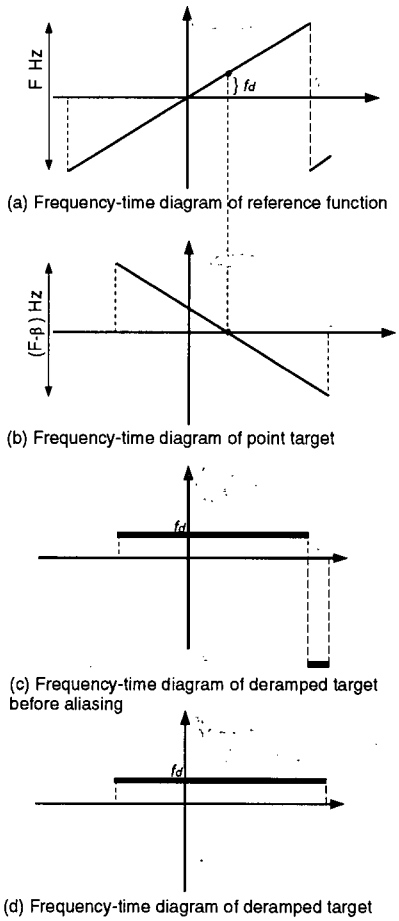

Figure 3.1 Deramping a single linear FM signal by time multiplication

The operations in Figures 3.1a, b, c, d must be extended to an entire line of received data. The received signal, which is modelled as the convolution of the transmitted pulse and the ground reflectivity [17], can be represented as a sum of point reflectors. This is shown in 3.2a. The reference function is repeated in time to encompass the entire length of the received data. The sawtooth frequency-time diagram of the reference function is shown in Figure 3.2b. The result of deramping a number of equally spaced point reflectors is shown in 3.2c.

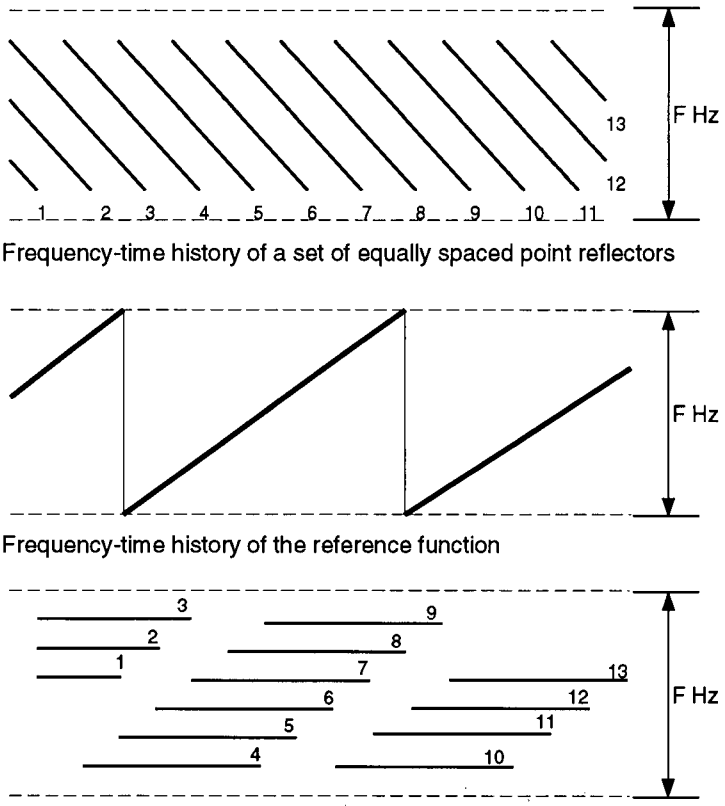

(a) Frequency-time history of a set of equally spaced point reflectors

(b) Frequency-time history of the reference function

(c) Frequency-time history of the product functions when the signals in (a) are multiplied by the reference function in (b)

Figure 3.2 Extending the deramping operation to multiple point targets

The Parallelogram Processing Region After deramping, the targets whose zero Doppler frequency is located within one reference function cycle will have frequencies ranging from –F/2 to F/2 Hz. These targets will constitute one processing region. The formation of parallelogram shaped regions from the deramped targets can be seen in Figure 3.2(c).

Consecutive processing regions are separated by lines of slope K (the FM rate of the reference function). Each processing region constitutes a parallelogram shaped area, and is referred to as the *parallelogram.* Each parallelogram is bound by the position of the reference function cycles. The top and bottom boundaries of the parallelogram are not as critical to the processing operation as the side boundaries, since digital aliasing will make the targets with frequencies above F/2 or below –F/2 equivalent to modulo F. These targets will fall within the next or previous processing

region. Figure 3.3 shows one processing region in more detail. The parameters defined on the figure are calculated as follows (where F is the sampling frequency and K is the FM rate of the signal).

The number of samples in one cycle of the reference function: $M = F^2 / K$;

The number of samples in each target: $M_c = (1 - \beta)M$

The β parameter denoting the guardband width as ratio of the parallelogram width: $\beta = 1 - BW / F$, where BW is the bandwidth of the transmitted pulse.

The guardband width of one parallelogram processing region (in samples) = βM

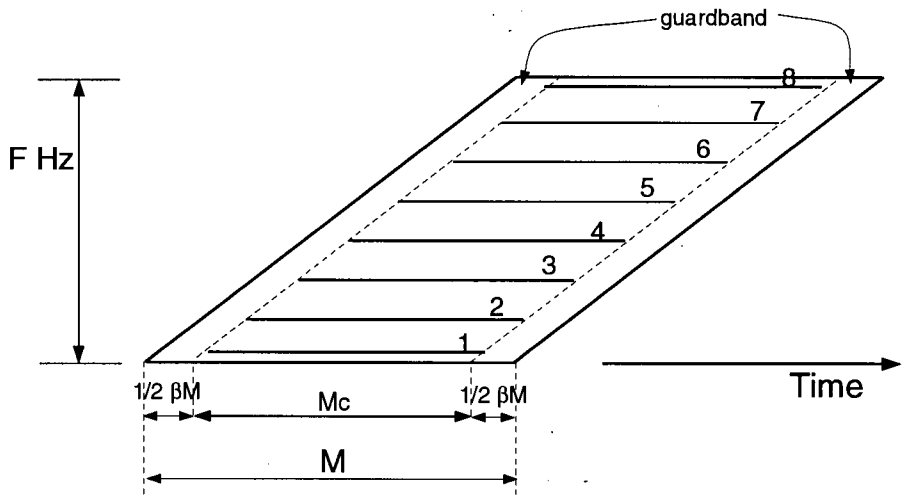

Figure 3.3 8 deramped targets constituting one parallelogram processing region

Each deramped target in the parallelogram has a unique frequency ranging from –F/2 to +F/2. It is this unique frequency which defines the position of each target with respect to other targets in the same parallelogram region.

The Guard Band The guard band is the region between successive parallelograms, shown in Figure 3.2, which does not contain valid target samples. It can also be seen as the dotted region on each side of the parallelogram in Figure 3.3.

The reason for the formation of the guardband in range processing is the longer time duration of the reference function, explained in section 3.2.4. This longer time duration ensures that the entire bandwidth of each target is limited to within one processing region and the deramped targets do not overflow into adjacent parallelograms. The guard band region, therefore, corresponds to regions outside the time interval of the radar pulse. The number of samples in the guardband can be calculated using the target bandwidth as shown from Figure 3.3.

DFT Block Placements The next step in the imaging process is to separate the targets into different energy cells with regard to their position in the time domain. As mentioned earlier the deramped targets in each processing region have unique frequencies ranging from $-F/2$ to $+F/2$. Short length DFT operations performed across the deramped data will separate the energy of each target into a unique DFT bin.

The number of points in the DFT is usually chosen as a power of 2 to facilitate the Fast Fourier Transform algorithm for the DFT (see Oppenheim [32, p. 587–605]). The placement of the DFT blocks is shown in Figure 3.4. The placement of the first DFT block is arbitrary. The next DFT block must be placed such that it covers the trajectory of the first target which is not completely covered by the previous DFT block. To do this a horizontal line (shown as *ab* in Figure 3.4) is extended from the point where the first DFT rectangle first coincides with the guardband to the guardband on the opposite side of the same parallelogram. The next DFT block is placed such that it contains the time domain samples $(b - N + 1)$ to b, where N is the DFT length.

To fully utilize the geometry of the parallelogram area, and to cover all the targets with the least number of DFT operations, the first DFT block in Figure 3.4 is positioned so that its right hand corner touches the right hand corner of the parallelogram region before the guard band. Because the frequency-time slope of the deramped target is zero Hz/s, the location of the compressed energy for a particular target does not vary with the location of the DFT block on the target trajectory.

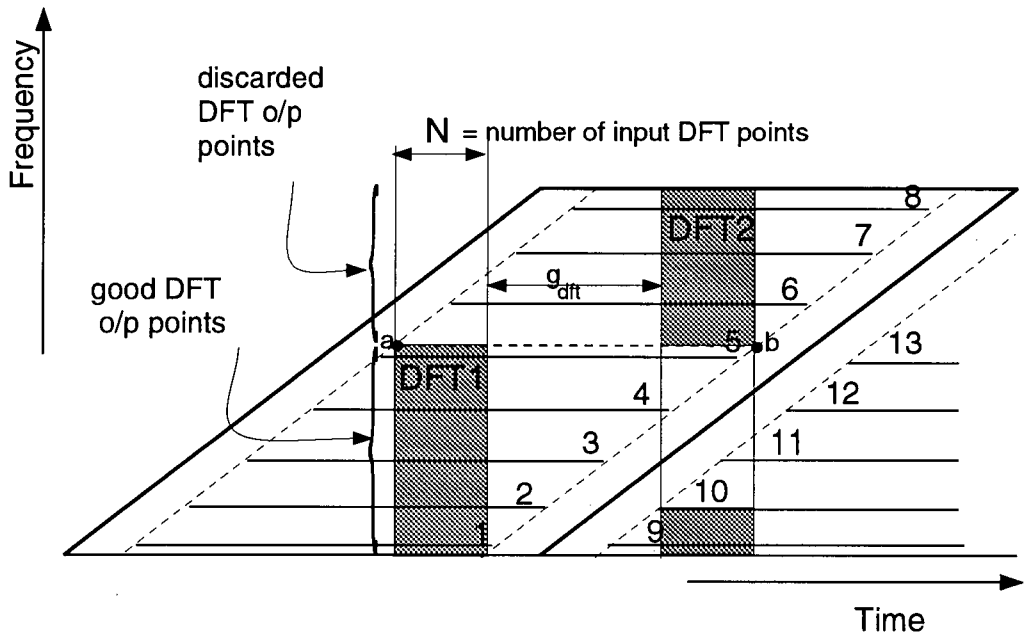

Figure 3.4 Parallelogram regions showing the placement of the DFT blocks in the single look case.

The gap between each DFT, g_{dft}, can be calculated from the geometry of the processing region as follows:

$$g_{dft} = \frac{G}{\alpha} - N \ , \tag{3.13}$$

where G is the number of good DFT output points; N is the number of input samples per DFT operation; M is the number of samples per reference function cycle, and α=N/M. Therefore,

$$\begin{aligned} g_{dft} &= N(1-\alpha-\beta)\frac{M}{N} - N \\ &= M(1-2\alpha-\beta) \ \ [samples] \ . \end{aligned} \tag{3.14}$$

As seen in Figure 3.4, the first DFT block contains N points of each of the trajectories of targets 1 to 5. The second DFT block is placed such that it covers the targets immediately after target 5 up to target 8 of the current parallelogram and targets 9 and 10 from the next parallelogram region.

Calculating the Good DFT Output Points Not all the DFT output points constitute valid image data. Part of the output points of each DFT correspond to guard band samples and incomplete sections of target trajectories. To see the division between valid and invalid DFT output points see the DFT1 block of Figure 3.4. The DFT rectangle can be divided into two regions by a horizontal line where the left-hand side of the rectangle touches the guard band. The upper section of the rectangle contains invalid output samples which must be discarded, output points corresponding to the lower section of the rectangle are kept in a buffer as the *good DFT output points*. Figure 3.5a and b shows an example of detected targets from two DFT blocks before extracting the good output points. The number of good output points are calculated (as shown later), stored in a buffer and concatenated together. The final output of the two DFT blocks is shown in 3.5c. The rest of the output points of each DFT block are discarded.

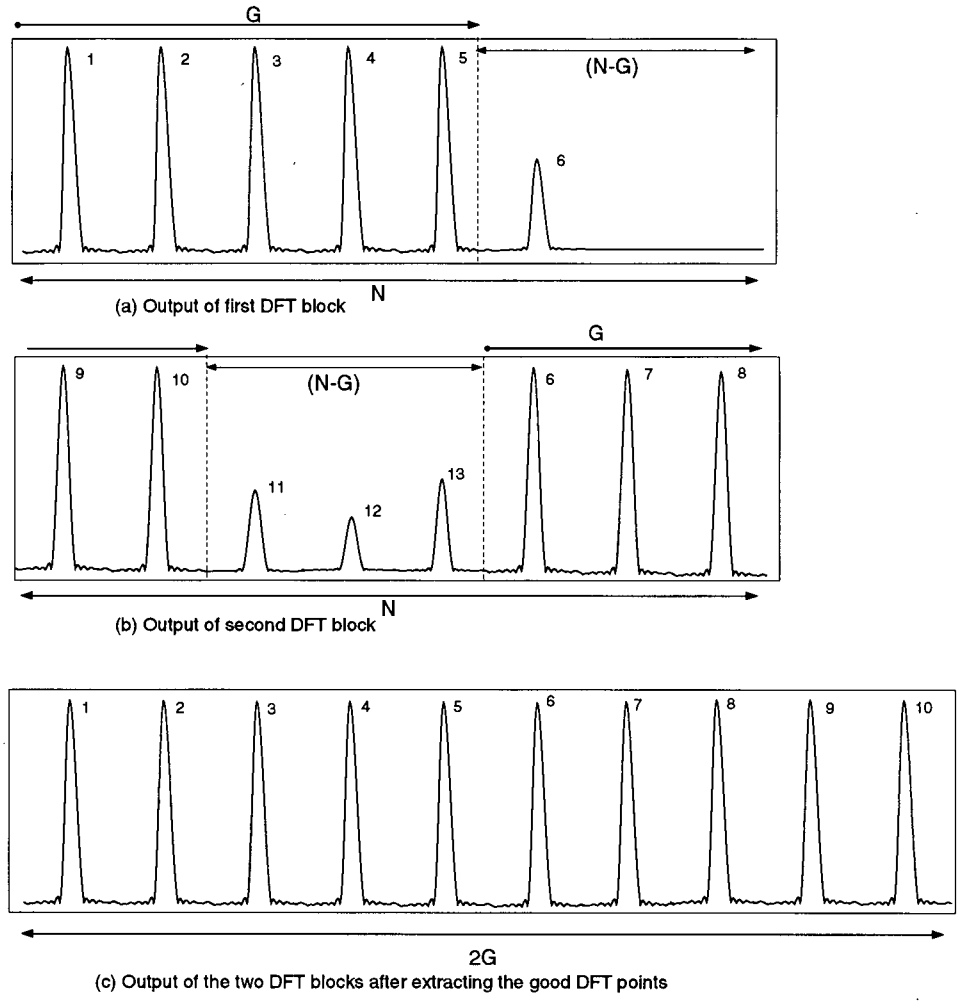

Figure 3.5 Output of each DFT block shown separately

The good DFT output points are calculated using the geometry of the parallelogram and similar triangles. See Figure 3.6.

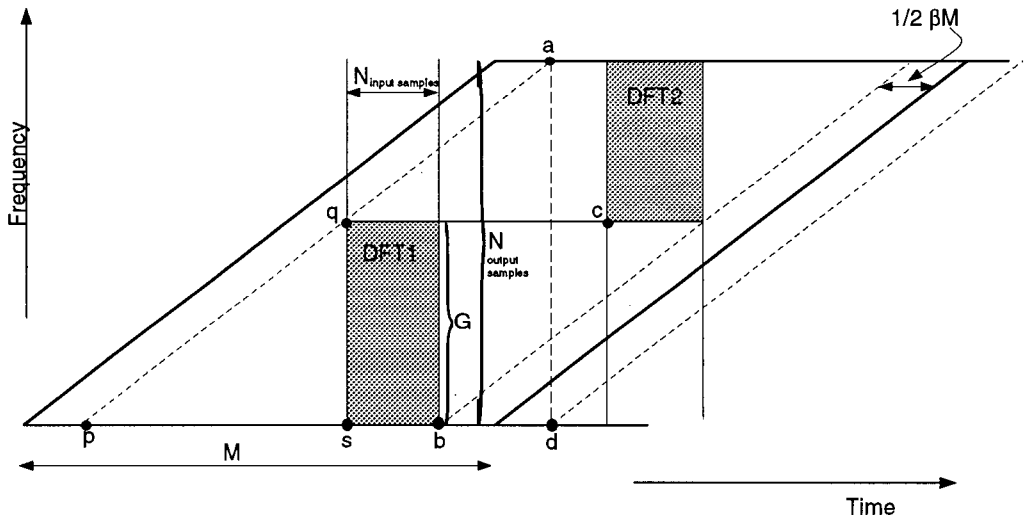

Figure 3.6 Calculation of good DFT output points

From the following relationship between similar triangles we can calculate the number of good output points.

$$\frac{ad}{dp} = \frac{qs}{sp} \tag{3.15}$$

From this the good output points (G) can be calculated as follows (note that α denotes the *N/M* ratio):

$$\frac{N}{M} = \frac{G}{(M - \beta M - N)} \tag{3.16}$$

and rearranging the equation gives:

$$G = N(1 - \alpha - \beta) \quad [samples] \tag{3.17}$$

Similarly we can calculate the distance between the starting point of successive DFT blocks (γ) in the single look case (where γ is the distance qc in Figure 3.6):

$$\begin{aligned} \frac{G}{\gamma} &= \frac{N}{M} \\ \gamma &= \frac{G}{\alpha} \end{aligned} \tag{3.18}$$

Resolution and Choice of DFT Length The choice of DFT length will affect the image resolution. The ability of a DFT operation to detect closely spaced signals depends on the number of input samples to the DFT. However, increasing the DFT block length in SPECAN will decrease the efficiency of the algorithm in two ways: the number of DFT operations required to detect all the targets will be increased, and the number of operations per DFT will increase.

The number of operations required for a Fast Fourier Transform is $5Nlog_2N$ [32, p. 590], therefore longer length DFTs will require more computation. The increase in the number of DFT operations is because widening the DFT rectangle will shorten the good output section of the DFT block and therefore more DFT blocks will be needed to cover the trajectory of all the targets. A shorter DFT input length will provide a larger ratio of good output points per DFT operation, which in turn will decrease the number of DFT operations required, but reduce the image resolution.

As shown in Chapter 2, range resolution is inversely related to the bandwidth of the transmitted pulse. In fast convolution imaging the entire bandwidth of each target can be used for compression; the resulting resolution of the image after fast convolution will be referred to as the full resolution. In SPECAN only part of the bandwidth of each target is used, that is, the bandwidth corresponding to the number of input samples to each DFT. The resolution of the SPECAN image will be N/M of the full resolution, where N is the number of input DFT samples, and M is the number of samples per target. The efficiency of SPECAN will be measured as the number of operations requrired compared to the number of operations required per fast convolution processing of the same range line length.

To show how the efficiency of SPECAN varies with resolution compared to the fast convolution method, all possible input DFT lengths possible for the ERS-1 satellite parameters were tested and the results are shown in Table 3.1. A 4096 sample long range line is used as a benchmark, and the ERS-1 parameters are used to calculate the number of DFT blocks requried

for the SPECAN compresssion. The first column of Table 3.1 shows the input lengths; the second column is the number of operations required for the SPECAN as a percentage of what is required for the fast convolution. The third column is the value of *N/M*, that is the resolution of SPECAN as a factor of the resolution of fast convolution.

FFT Length	Operations (% of fast convolution)	Resolution (% of fast convolution)
32	0.78	4.55
64	1.81	9.09
128	4.82	18.18
256	13.91	36.36
512	61.69	72.73

Table 3.1 Variation of efficiency and resolution with the SPECAN DFT length

From the table it is apparent that as the FFT length (and therefore resolution) is doubled the efficiency is quartered. This is illustrated in Figure 3.7 which is the plot of the polynomial fit to the values in Table 3.1.

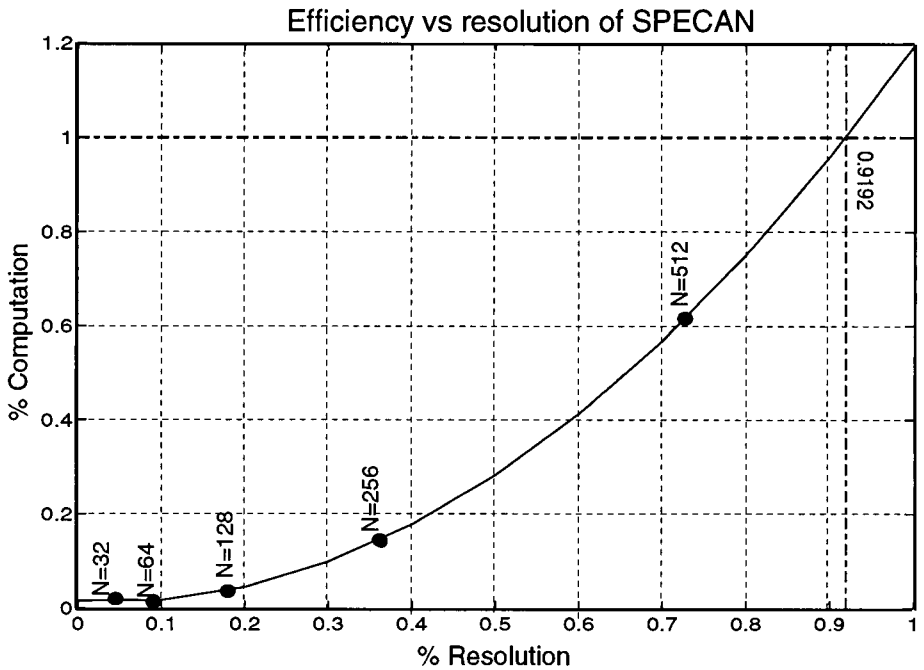

Figure 3.7 Comparison between SPECAN and fast convolution in terms of resolution and computation requirements.

Figure 3.7 shows that at high resolutions SPECAN does not provide much efficiency over fast convolution considering the loss of resolution. For ERS-1 parameters, a sample size of 256 is advantageous for quicklook processing. At this input length 36% of the full resolution is obtained by expending only 14% of the computation required.

Chapter 4 Radiometric Degradation in Range-SPECAN

This chapter explains the image quality problem (scalloping) associated with the use of SPECAN for range processing. The main image degradation is explained using the transmitted signal characteristics, and the effect of a correction scheme to eliminate the scalloping is proposed and simulated on point targets.

Section 4.1 Scalloping

Images which have been range processed using SPECAN show degradation in the form of regular light and dark bands in the range dimension; this effect is called "banding", or "scalloping". The period of the scalloping corresponds to the number of good DFT output points, which is calculated in Equation (3.17).

Figure 4.1 is an ERS-1 satellite scene from the ocean off the coast of Halifax. The image has been formed by range compression using SPECAN, and azimuth compression using the fast convolution method. Scalloping is visible at boundaries between the four DFT range blocks across the image. Summing the SPECAN range processed lines over the entire image will show the average amount of scalloping over the area. Figure 4.2 shows the average amount of scalloping over 2048 range lines by averaging the digital image file from Figure 4.1.

For comparison the same scene has been processed using fast convolution in both range and azimuth. The resulting image is shown in Figure 4.3. No scalloping is visible in the image and this is further verified by averaging the digital image file as shown in Figure 4.4[1].

---

[1] The grainy apearance of these images is due to speckle noise which is an inherent part of radar imagery. See Freeman [33] for a description of speckle. To better see the images hold them at 80 *cm* from your eyes.

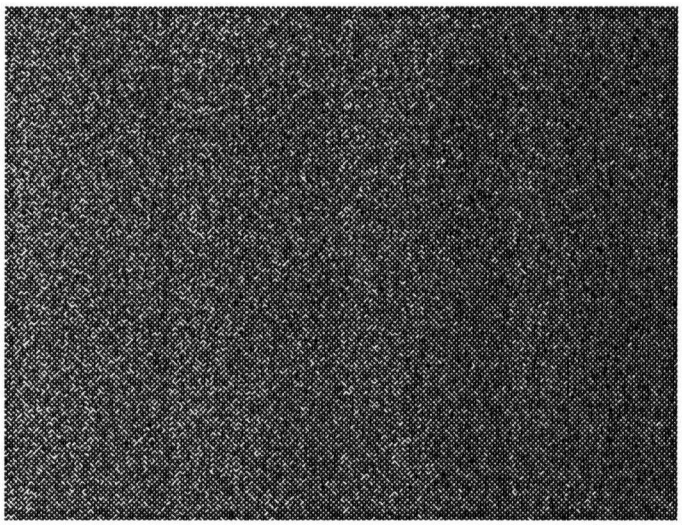

Figure 4.1 Ocean scene processed using SPECAN in range, scalloping is present

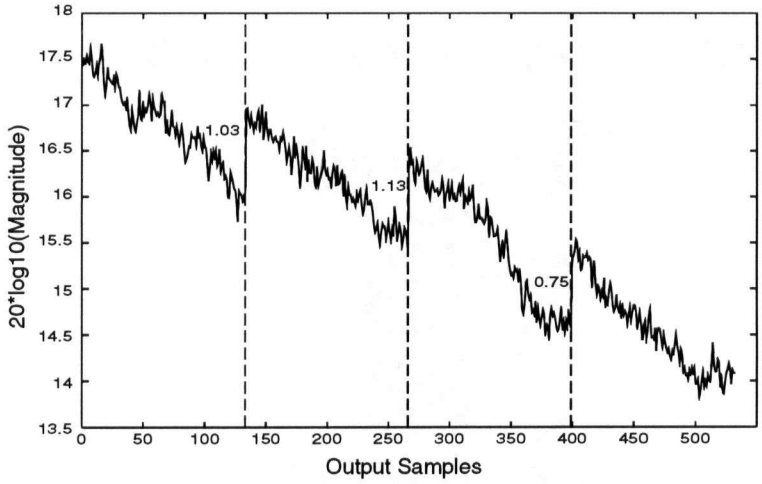

Figure 4.2 SPECAN output: sum of 2048 lines of the digital image

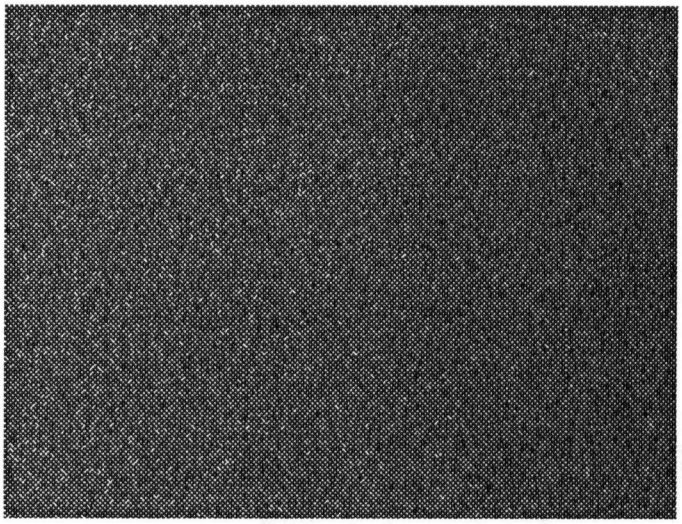

Figure 4.3 Ocean scene processed by fast convolution method, no scalloping is observed

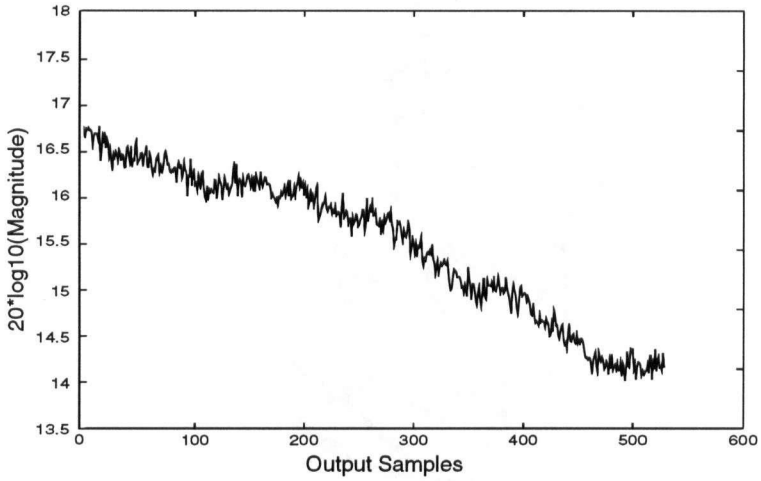

Figure 4.4 Fast convolution output: sum of 2048 range lines of the digital image

Scalloping is most noticeable in smooth, featureless areas, such as scenes of ice and water. In scenes containing a wide range of features scalloping is less apparent because the amount of scalloping is insignificant compared to the natural radiometric variations of the scene. Also, because the human visual system tends to overshoot or undershoot around areas of different intensities, over a large smooth area the perceived scalloping will be further emphasized, especially at the boundaries (Gonzalez [34, p. 28]).

Section 4.2 Cause of Scalloping

Ideally the pulse transmitted by the satellite has a flat, rectangular envelope. However, the chirp replica[2] included in the ERS-1 satellite auxiliary data shows a time-varying envelope. The remainder of this section will show that the time-varying energy of the transmitted pulse is responsible for SPECAN range scalloping.

The scalloping occurs at the DFT boundaries (as verified by Figure 4.2). To investigate the cause of the problem we will consider the changes that occur in the deramped data at the DFT boundaries. We will also investigate how a varying chirp amplitude will affect the radiometry of the image as the outputs of successive DFT's are strung together to form the image.

Initially, to estimate how much scalloping should be expected, a chirp replica from the ERS-1 scene is extracted and examined. Figure 4.5 is a model of the typical envelope of the transmitted pulse derived from the ERS-1 chirp replica. (For a sample of the actual chirp replica refer to Figure 5.2).

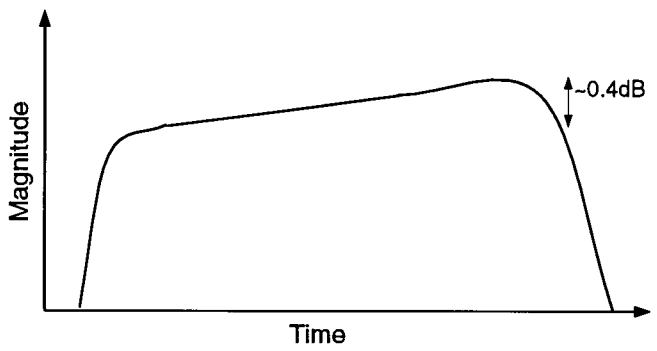

Figure 4.5 Typical envelope of ERS-1 chirp replica

The next step is to examine how the chirp envelope affects the boundary between successive DFTs. Figures 4.6 and 4.7 illustrate the effect of the chirp amplitude on detected point targets by showing two consecutive DFT placements on the deramped signals.

---

[2] The chirp replica refers to a copy of the ERS-1 pulse which has been sent through the transmitter and receiver, though not through the antenna system. This signal is the best available estimate of the amplitude of the transmitted pulse.

Figure 4.6a represents the situation where the chirp amplitude is constant. Correspondingly the detected targets in 4.6b have equal amplitudes. Figure 4.7a shows the case where the amplitude of the transmitted pulse, and consequently each deramped target, increases with time (this is represented by a thickening of the lines representing the frequency-time profile of the deramped targets). The magnitude of each output point target is the summation of energy through the gray shaded part of its exposure (DFT input samples). Figure 4.7b shows that the amplitude of each detected target depends on the average energy of the section of the transmitted pulse from which the deramped target samples are chosen. Because of the varying chirp envelope, the average energy of the deramped targets varies, causing the scalloping effect. The amount of scalloping corresponds to the energy difference between the beginning and end of the chirp spectrum.

Note that the detected targets in Figures 4.6b and 4.7b only illustrate detection of the position of maximum energy for each target, and do not show the actual compressed pulse shape or sidelobes which are a result of the finite pulse length.

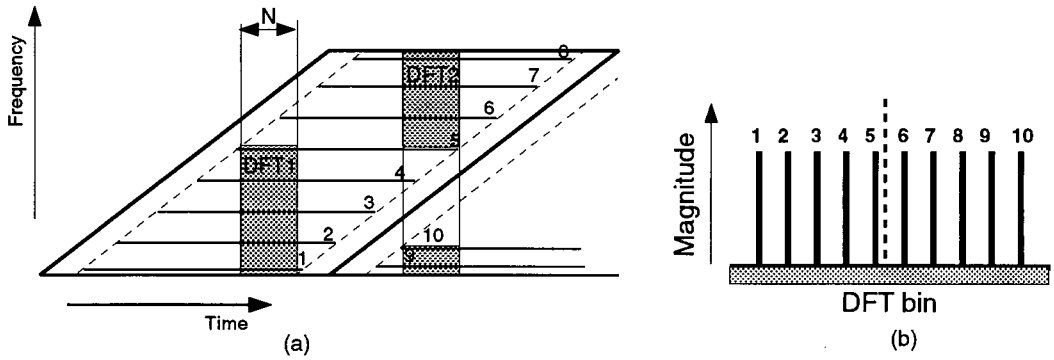

Figure 4.6 Illustrating effect of ideal deramped targets (a) on detected targets (b).

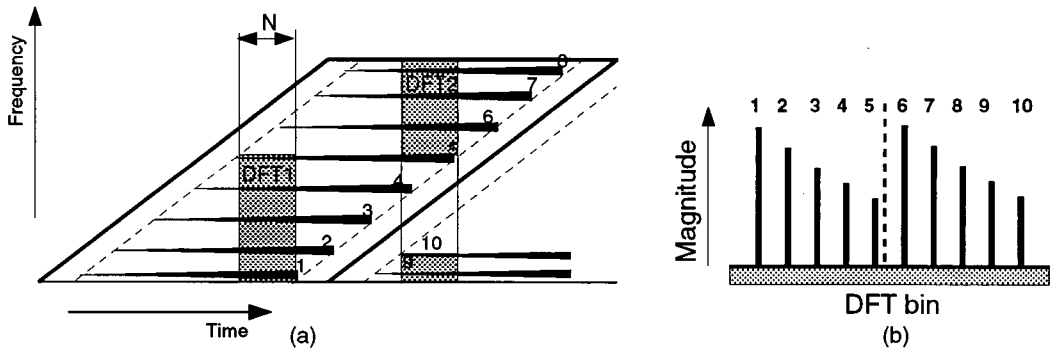

Figure 4.7 Illustrating effect of deramped targets of varying envelope amplitude (a) on detected targets (b).

Scalloping is a phenomena unique to SPECAN and is a result of the way the matched filter is applied to the deramped signal. The matched filter changes its center frequency as a function of time, as it is moved along the raw data compressing blocks of the received signal; in fast convolution methods the matched filter is stationary in frequency space. The output of SPECAN, therefore, is dependent on the position of the matched filter with respect to the deramped signal. The following section will explain the correction implemented to compensate for the varying energy of the transmitted chirp.

Section 4.3 Proposed Solution of Scalloping Problem

In this section a scheme to correct for the effect of the varying chirp envelope will be proposed by studying the point target compression equations.

The obvious solution is to correct for the envelope of each target before the DFT operation by using an accurate estimate of the envelope of the transmitted chirp. However, each block of deramped data chosen for the DFT operation (as seen in Figures 4.6 and 4.7, for example) contains the sum of deramped targets at different frequencies, and from different parts of the chirp envelope. Therefore it is not possible to correct for the envelope of each individual target in the time domain. After the DFT operation most of the energy of each target is confined to a single frequency bin. It is then possible to implement a correction scheme to remove the dependency of the amplitude of each detected target on its position in the chirp envelope.

If the exact variation of the chirp envelope with respect to time is known, its effect can be cancelled by dividing the detected output by the average value of the envelope for that segment. This correction will be justified in the following paragraphs using the assumption that the signal frequencies correspond to center bin values. For other frequencies the result in Equation 4.8 has been verified by simulation to be true to within 0.06%.

From Chapter 3 we know that the ideal deramped target, *d(t)*, of magnitude *A*, is a constant frequency signal of the form:

$$d(t) = A\, e^{j\theta t}\,, \qquad 0 \leq t \leq T\,, \tag{4.1}$$

where *T* is the time duration of the pulse. The constant phase terms have been omitted to keep the equation simple. This can also be written in terms of *M* samples spaced at *1/Fr* seconds, where *Fr* is the sampling frequency, and *M = T * Fr*:

$$d[m] = A\, e^{j\theta m} \qquad 0 \leq m < M \tag{4.2}$$

If the transmitted signal had a time varying envelope, *env[m]*, the deramped target would be

$$d[m] = A\, env[m] e^{j\theta m} \tag{4.3}$$

Using the point target arrangement from Figure 4.6, target 1 corresponds to the beginning, and target 5 to the end of the chirp spectrum. The two segments are shown on the same envelope in Figure 4.8 for comparison.

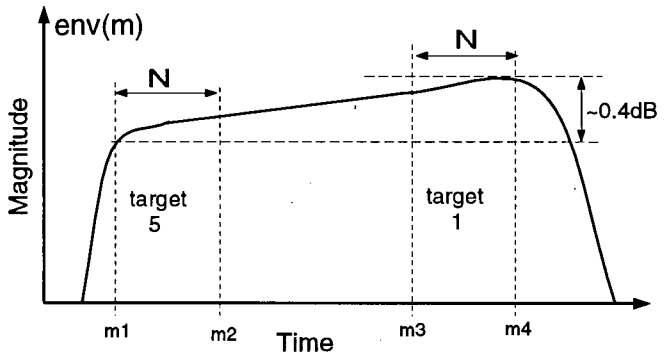

Figure 4.8 Magnitude displacement of first and last detected targets.

Let Y_i be the compressed output of the i*th* target. Using $Y_1(k)$ and $Y_5(k)$ from the two extremes of the chirp envelope of Figure 4.8 we can write:

$$\begin{aligned} Y_1(k) &= A\cdot\mathrm{DFT}\left[env(m)e^{j\theta m}\right]_{m_1}^{m_2} \\ Y_5(k) &= B\cdot\mathrm{DFT}\left[env(m)e^{j\theta m}\right]_{m_3}^{m4} \end{aligned} \tag{4.4}$$

Where A and B are scalars denoting the strength of the reflection from points 1 and 5 on the ground, respectively.

Using the relationship between convolution and multiplication, the equation can be rewritten as follows, where "*" is the convolution operator.

$$\begin{aligned} Y_1(k) &= A\cdot\mathrm{DFT}[env(m)]_{m_1}^{m_2} * \mathrm{DFT}\left[e^{j\theta m}\right]_{m_1}^{m_2} \\ Y_5(k) &= B\cdot\mathrm{DFT}[env(m)]_{m_3}^{m_4} * \mathrm{DFT}\left[e^{j\theta m}\right]_{m_3}^{m_4} \end{aligned} \tag{4.5}$$

For ideal, identical point targets differing only in magnitude, $|Y_1(k)| = |Y_5(k)|A/B$. For both $Y_1(k)$ and $Y_5(k)$ the second term on the right hand side of Equation (4.5) is an impulse of magnitude N. Therefore the only source of difference in the two detected targets is the DFT of

the envelope segments. Denoting the peak value of $|Y_1(k)|$ and $|Y_5(k)|$ as Y_1 and Y_5 respectively, we can write

$$\frac{Y_1}{Y_5} = \frac{A}{B}\frac{peak\left(\mathrm{DFT}[env(m)]_{m_1}^{m_2}\right)}{peak\left(\mathrm{DFT}[env(m)]_{m_1}^{m_4}\right)} \tag{4.6}$$

For the case where the envelope is slowly varying and can be approximated by a straight line of constant slope the two sections are related by a constant b; for $m_1 \le m \le m_2$, $env(m) \equiv a_1(m)$, and for $m_3 \le m \le m_4$, $env(m) \equiv a_2(m) = a_1(m) + b$. Because DFT(a + b) = DFT(a) + DFT(b), the ratio of the two sequences will be:

$$\frac{\mathrm{DFT}[a_1(m)]}{\mathrm{DFT}[a_2(m)]} = \left[\frac{\sum_{m=0}^{N-1} a_1(m)}{\sum_{m=0}^{N-1} a_2(m)},\ 1,\ 1,\ 1,\ \ldots\right] \tag{4.7}$$

and the only difference between $a_1(m)$ and $a_2(m)$ will occur in the first (peak) term. The ratio of the peak value of the two point targets reduces to

$$\frac{Y_1}{Y_5} = \frac{A\sum_{m=0}^{N-1} a_1(m)}{B\sum_{m=0}^{N-1} a_2(m)} \ . \tag{4.8}$$

This verifies that to correct the amplitude difference resulting from the varying chirp envelope it suffices to normalize each detected target by the mean value of the segment of the envelope corresponding to the position of the target. The correction vector, $C(l)$, will correct one DFT output block, and therefore will be G samples long, where G is the number of good DFT output points. The equation for $C(l)$ will be

$$C(l) = 1/\left[\frac{1}{N_r}\sum_{i=ld}^{ld+N_r-1} env(-i)\right] \qquad 0 \le l < G \tag{4.9}$$

where d determines the distance between each N_r long section of the amplitude envelope (in samples). For M being the number of samples in the chirp replica, d is calculated as: $d = (M - N_r) / G$. The reason for time-reversing the envelope vector is that the arrangement of output

samples (as seen in Figure 4.6, for example) is such that the first output sample of each DFT block corresponds to the last segment of the deramped target envelope.

This solution has the advantage that its implementation adds very little computation to the algorithm. Each detected range line must be multiplied by the correction vector, which needs to be calculated only once. This is important since the main advantage of using SPECAN is its efficiency compared to other imaging algorithms, therefore a computationally intensive correction would nullify the main advantage of the algorithm.

In the next section the effect of varying chirp amplitude and correction for it will be tested on simulated point targets.

Section 4.4 Point Target Simulation

Point target analysis is usually performed to measure the quality of an imaging algorithm, and the effects of changing parameters on the image quality. We are able to extrapolate our findings to real data because SAR processing is a linear operation to which superposition applies.

In this section a number of point targets are simulated and the effect of the chirp envelope shape on the output is observed. It is shown that the correction method explained in the previous section will eliminate the scalloping. This thesis is concerned with SPECAN range compression, therefore point targets will be simulated in the range dimension only. The ERS-1 parameters relevant to the point target simulation and range processing which are used in out simulation are shown in Table 4.2.

Bandwidth (BW)	15.55 MHz
Pulse Length (T)	37.1 μs
Analog to digital complex sampling rate (F_r)	18.96 MHz
FM Rate (K_r)	0.4191 MHz / μs

Table 4.2 ERS-1 SAR parameters for the transmitted signal

Figure 4.9a shows the real part of a complex linear FM chirp which was simulated using the ERS-1 parameters. Note that in both 4.9a and 4.11a the amplitude variations toward the beginning and end of the signal are only a result of sampling. We will use the spectrum of the signal as an indicator of how its energy varies with time[3]. Figure 4.9b shows the magnitude of the spectrum of the signal in Figure 4.9a.

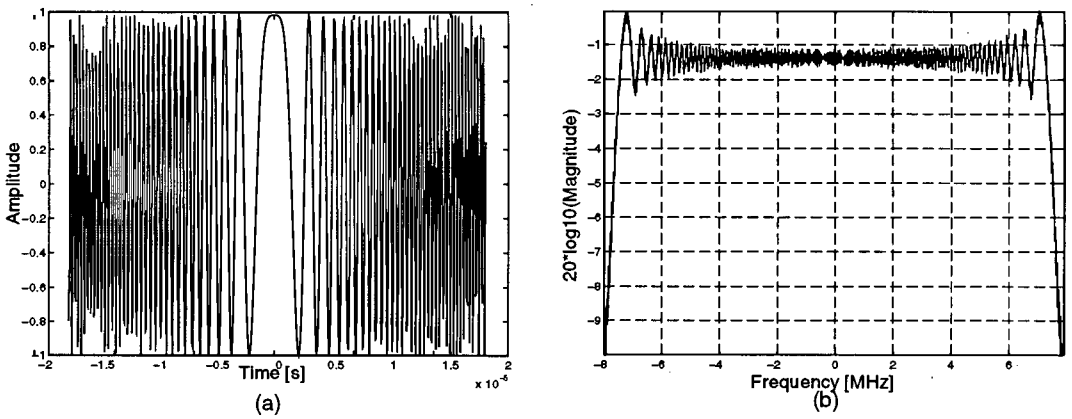

Figure 4.9 Single point target in time and frequency domain. The target has a rectangular envelope.

The simulated received signal is the sum of 20 identical point targets with rectangular envelopes. This signal is processed using the SPECAN algorithm as explained in Chapter 3; the resulting compressed point targets are shown in Figure 4.10. The processor has detected all the targets at equal amplitudes. Note that the output is in frequency samples and must be multiplied by the factor F_r/K_rN_r to represent time. The dotted line represents the boundary between two DFT output cycles.

[3] The energy in the frequency domain varies as in the time domain for the ERS-1 transmitted signal because it is an upchirp (has positive FM rate).

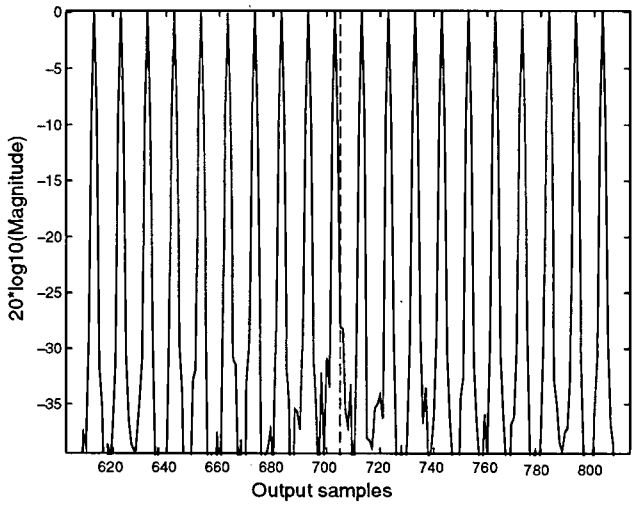

Figure 4.10 Point targets compressed using SPECAN

Next, the case is shown where the envelope of the transmitted signal is a straight line with a constant slope. Figure 4.11a shows the real part of the linear FM chirp, and Figure 4.11b is the spectrum of the signal. The 2 *dB* gain across the envelope of the signal translates directly to a 2 *dB* gain across the spectrum of the signal.

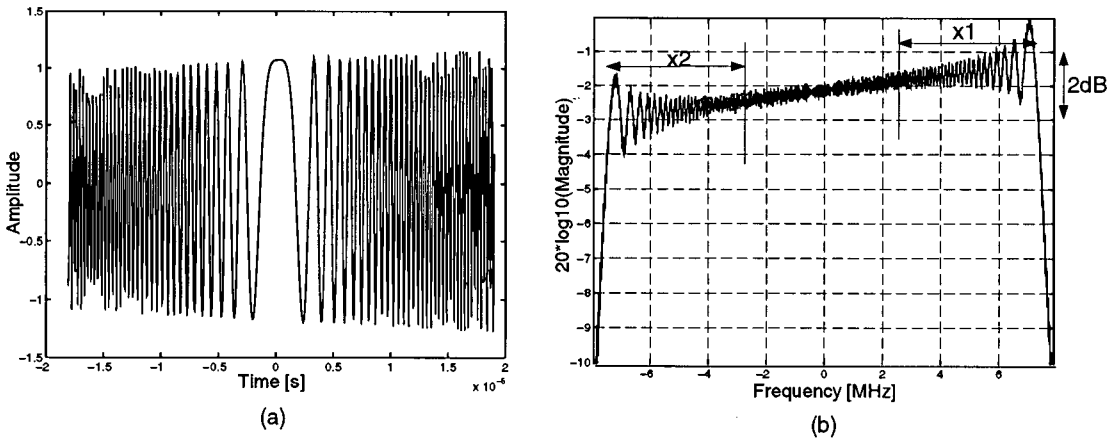

Figure 4.11 Real part (a), and spectrum (b) of chirp with a linear envelope superimposed

The predicted scalloping is the amount $\Delta x = (\Sigma x_2 - \Sigma x_1)/N_r$, which for this example equals 1.38 *dB*. *Nr* is the DFT input sample size.

Figure 4.12 is the range compressed output when the input contains 20 equally spaced identical targets of the form in Figure 4.11. We see the time varying chirp envelope causes

scalloping at the DFT boundaries of SPECAN range processed images. The DFT boundaries are shown by the dotted lines.

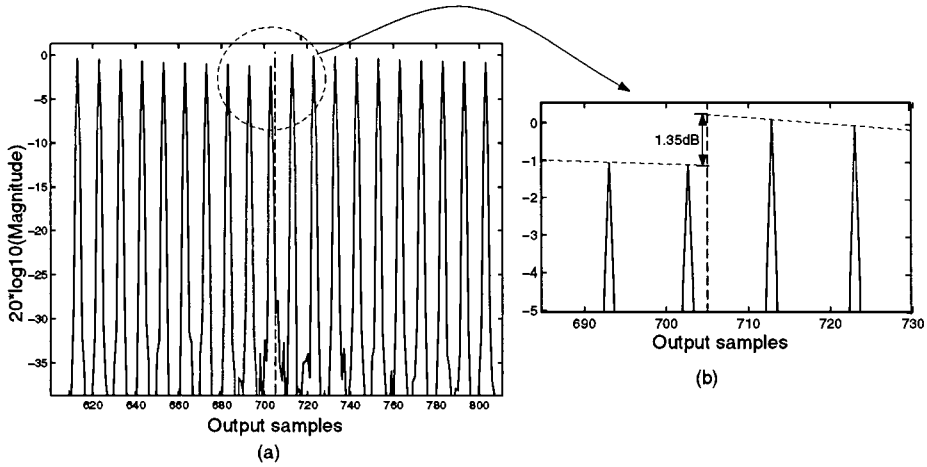

Figure 4.12 Output showing scalloping at the DFT boundary

The scalloping is measured from Figure 4.12 to be 1.35 *dB*. This value is close to the Δx value derived from the pulse envelope. Figure 4.13 shows the same output after it is corrected.

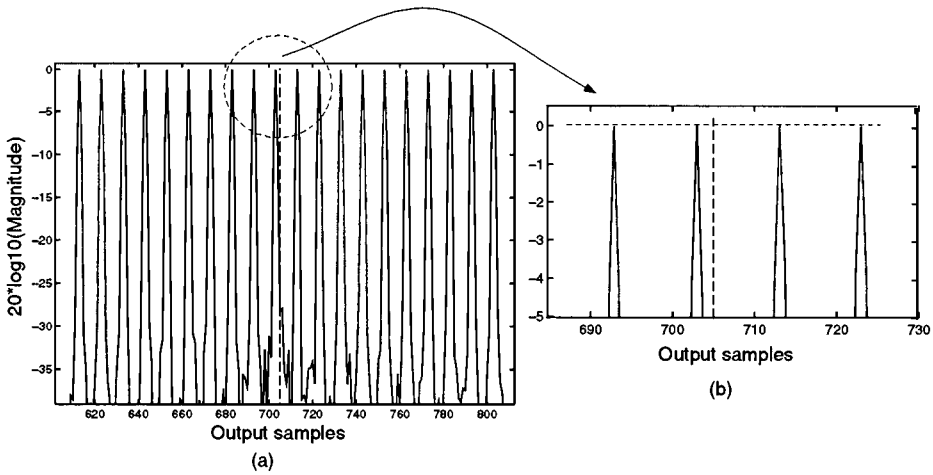

Figure 4.13 Output corrected for scalloping

The reason the measured scalloping on Figure 4.12 is not exactly equal to the 1.38 *dB* value measured from the chirp envelope is leakage from the incomplete targets in the parallelogram. The DFT input samples chosen from the parallelogram contain some incomplete trajectories

of targets from the next and previous DFT blocks. These incomplete targets contain a non-integer number of cycles. Although the output points corresponding to these incomplete targets is discarded, part of their energy is introduced in the good DFT output points as leakage and cannot be removed. However the amount of energy leakage introduced in this way is in the hundredths of *dB*s and not significant.

Comparing Figures 4.10 and 4.13 shows that the correction factor eliminates the scalloping resulting from the varying chirp envelope to at least 0.03 *dB* in the point target simulation.

Chapter 5 Range-SPECAN on ERS-1 Data

This chapter presents the results of SPECAN range compression on ERS-1 data. The functions of the ERS-1 synthetic aperture radar are outlined; the properties of the raw satellite data and their impact on SPECAN range processing is described.

Section 5.1 The ERS-1 Satellite

To verify the results of the point target simulation of the previous chapter, SPECAN range processing and scalloping correction are carried out on ERS-1 satellite data. This satellite was launched on July 17, 1991 by the European Space Agency (ESA). Its main objective is to increase the understanding of the interaction between the earth's atmosphere and oceans on a global scale. Other major benefits it provides are ice-coverage measurements, monitoring of pollution, and land use changes.

Figure 5.1 shows the geometry of the ERS-1 satellite in strip-mapping mode. In this mode the satellite obtains high resolution imagery of a strip of ground by sending a microwave beam towards the ground at regular intervals and receiving the echo while moving at a constant velocity. The ERS-1 is placed in a polar orbit with a mean altitude of 780 *km*, and images 100 *km* wide strips of terrain.

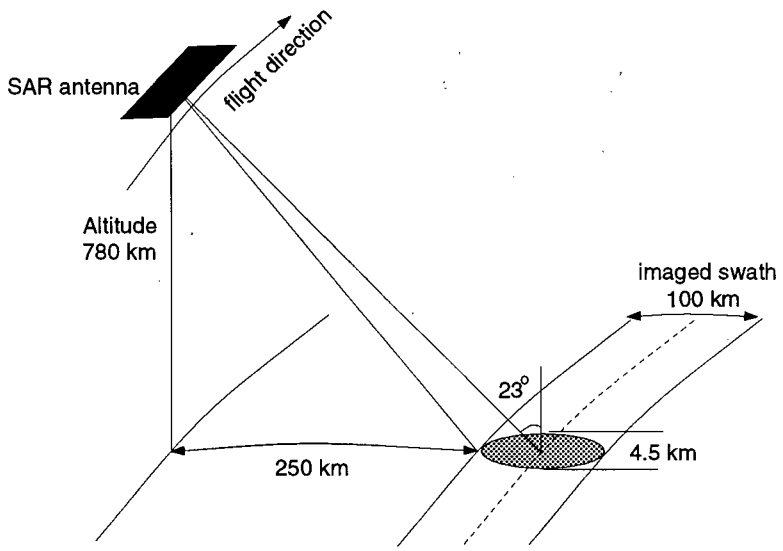

Figure 5.1 ERS-1 SAR strip-mapping geometry

Some of the ERS-1 SAR engineering parameters are given in Table 5.3.

SAR antenna size	10 *m* long, 1 *m* wide
Frequency	5.3 *GHz* (C band)
Bandwidth	15.55 *MHz*
Pulse Length	37.1 μs
FM rate	0.4191 *MHz* / μs
Polarization	linear vertical
A/D complex sampling rate	18.96 *Msamples/sec*
I and Q quantisation	5 bits
Sampling window duration	299 μs
Swath width	100 *km*
Incidence angle	23° at midswath
Data rate	105 *Mbps*

Table 5.3 ERS-1 SAR parameters

The operations of the ERS-1 Active Microwave Instrument (AMI) which also includes the SAR module have been explained fully by Carter [35], Blisset [36], and Francis [7]. The SAR module of the ERS-1 satellite transmits pulses, amplifies and filters the received signal. The module has two modes of operation: image mode, and wave mode. Image mode obtains the

high resolution imagery with which we are concerned in this thesis, so all ERS-1 operations mentioned from now on are image mode operations. The transmit module of the SAR outputs a linearly chirped pulse of 15.55 *MHz* bandwidth and 37.1 μs length at the intermediate frequency of 123 *MHz*. The up-converter converts the output to 5.3 *GHz*, amplifies to 250 *mW* and sends to the high power amplifier (HPA). The signal is then amplified to about 4.5 *kW* and sent to the circulator assembly and the SAR antenna. The circulator allows the antenna to be time-shared between transmitter and receiver. The receiver filters the echo and down-converts it to baseband (zero center frequency). The demodulator creates sine and cosine channels in quadrature. The receiver also amplifies the received signal to adapt its level to that of the analog-to-digital convertor. After analog to digital conversion, where the data is quantized to 5 bits for each of the in-phase (I) and quadrature (Q) channels, and adding auxiliary data, the signal is either sent to a receiving ground station if one is within transmission distance, or recorded for future transmission.

Section 5.2 The Chirp Replica

As we have seen in the previous chapter, removal of scalloping requires accurate knowledge of the profile of the transmitted chirp. The calibration unit of the ERS-1 satellite SAR intercepts the transmitted chirp after it passes through the HPA and before it reaches the antenna (see Figure 2.2). A copy of this signal is fed back to the receiver and recorded in the echo line as auxiliary data to be used for on-ground range compression. Thus, this replica of the transmitted signal contains all the system distortions except those induced by the antenna which are negligible.

For our purpose, the replica pulse is extracted from the raw data header and used as the most accurate available representative of the transmitted chirp envelope. Figure 5.2a, the absolute value of one pulse replica, shows that the transmitted signal is noisy and has a non-rectangular envelope. The SAR receiver thermal noise contributes to the replica noise. As Figure 2.2 shows,

the chirp replica is intercepted after passing through the high power amplifier, this is another cause for the distortion seen in the chirp replica. The total distortion, as shown by Blisset [36], can be divided into linear, quadratic, ripple and noise components. The ripple and noise components will not have a particular effect at the DFT boundaries and therefore will not affect scalloping. The linear and quadratic components will be accounted for by the correction vector.

A number of replicas from different scenes have been examined and altogether there is very little variation in the transmitted signal from scene to scene. A study by Laur [37] has shown that the ERS-1 replica pulse total power is quite stable (to within ± 0.1 *dB*), that is, the transmitted signal power does not vary significantly from pulse to pulse. Therefore the degree of scalloping resulting from the chirp profile should be constant throughout each scene. By averaging 256 point sections of the chirp replica to derive the correction we are cancelling the effects of the noise, since 256 points is large enough to mask the short term perturbations of the replica. Figure 5.2b is the least squares fit straight line derived to show the noiseless envelope, and the approximately 0.5 *dB* increase from the beginning to the end of the chirp profile.

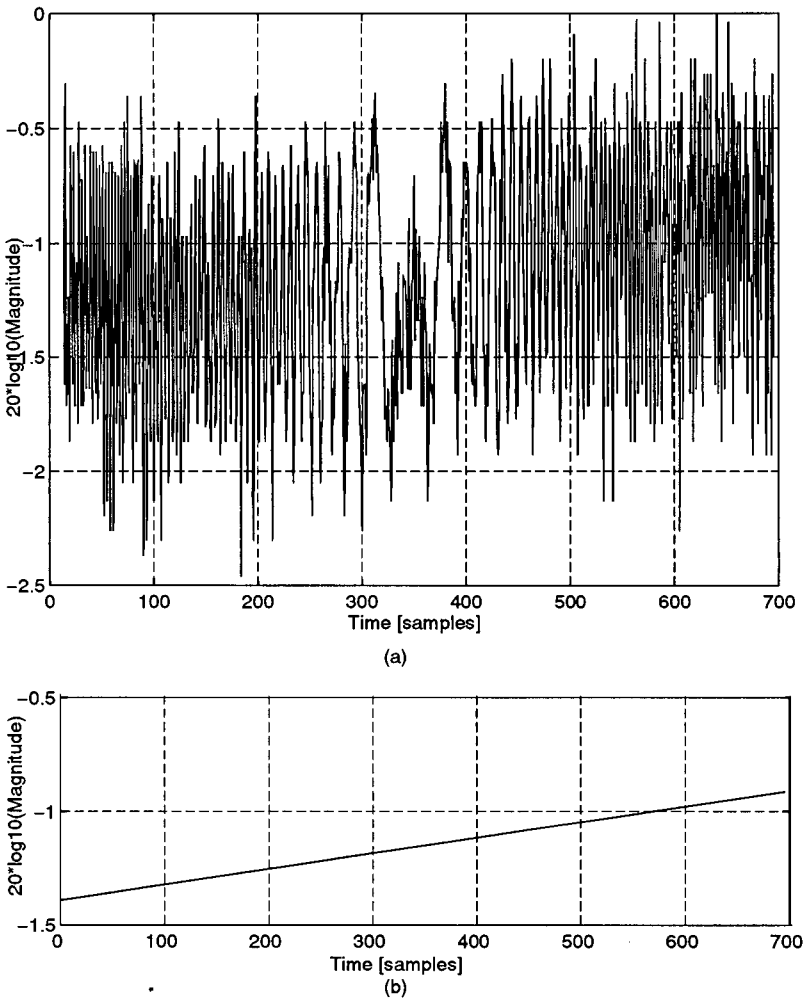

Figure 5.2 Envelope of the chirp replica (a), and approximation of the envelope to a straight line (b)

The chirp amplitude envelope of Figure 5.2a will be used to derive the correction vector according to Equation (4.9) repeated here:

$$C(l) = 1/\left[\frac{1}{N_r}\sum_{i=ld}^{ld+N_r-1} env(-i)\right] \qquad 0 \le l < G \tag{5.1}$$

The good DFT output points are derived from the ERS-1 satellite parameters in Table 5.3 and Equation (3.17) to be 133. The 133 point correction vector derived from the envelope of Figure 5.2a is shown in Figure 5.3 below.

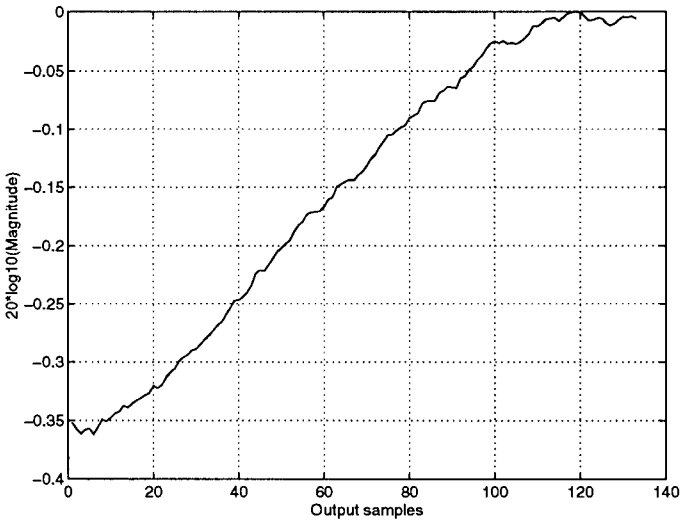

Figure 5.3 Correction vector derived from the chirp replica envelope

The effect of scalloping and the correction implemented was tested on a number of ERS-1 scenes. A significant difference in the amount of scalloping was observed between scenes of land and those of water and ice. The results of testing different combinations of water and land have been included. The reasons and significance of the differences between the output of different scene contents is mainly due to saturation of the raw data, and will be explained in the next chapter.

Section 5.3 Properties of the ERS-1 Raw Data

Prior to processing, it is necessary to verify that the data has not been corrupted during on-board processes such as in-phase (I) and quadrature (Q) channel separation and analog to digital conversion, and also that the methods of reading the raw data from the tape are correct. ERS-1 SAR raw data is received from the ADC output as a string of 5 bit in–phase (I) and 5 bit quadrature (Q) values unpacked to 8 bit integers. The statistical properties of SAR raw

data are the initial indicators of the quality of the data. Other ways to test the raw data include examining the spectrum of the raw data, and forming an image.

5.3.1 Statistical Properties

The "central-limit theorem" states that the sum of N independent random variables approaches Gaussian distribution as N becomes large. The received SAR echo has a Gaussian probability density function because the antenna footprint is large and the received SAR echo is the reflection from a diverse area [19]. Each resolution cell is a few square meters of ground area; the complex number representing the reflection from this cell is the coherent sum of the many reflections from each point in this area. The I and Q channels each have Gaussian distribution with 0 mean. Any dc bias or channel gain imbalance is removed prior to processing[1]. The validity of using a Gaussian distribution for ERS-1 raw data has also been verified by Laur [37] by comparing and showing the agreement of the percent saturation versus the standard deviation plots of simulated Gaussian data and ERS-1 raw data.

The ERS-1 ADC linearly quantizes the I and Q channel inputs to 5 bit values. The saturation level of a linear quantizer is set to $k\sigma$, and for 5 bit quantization of Gaussian signals the optimum value of k which would minimize the quantization and saturation errors is approximately 2.9. A larger value of k will decrease saturation noise, and a lower value will decrease the quantization noise as described by Gray [38] and Richards [39].

Saturation is calculated as the percentage of samples occupying the highest and lowest quantization levels *in excess* of the expected percentage of samples at those bins. In general, the amount of saturation decreases from near range to far range because the strength of the received backscatter is higher at near range. The amount of saturation in the raw data also depends on the scene content. Areas with high backscattering level, such as water during storms, will have

---

[1] Channel gain imbalance refers to the ratio of the total power of the I and Q channels which is ideally one.

the most amount of raw data saturation. Checking the histogram of the received SAR data and comparing it with the theoretical Gaussian distribution is one way to evaluate the integrity of the data. The results of this comparison for the scenes used in the thesis are shown in Figure 5.5.

5.3.2 Spectrum of Raw Data

Ideally, the spectrum of the raw data in the range direction should be that of the transmitted chirp. The received signal as a function of time, *s(t)*, is the convolution of the transmitted signal, *r(t)*, and the ground reflectivity, *g(t)*.

$$s(t) = r(t) * g(t) \tag{5.2}$$

Using the properties of convolution, the spectrum of the above, $S(\omega)$, can be rewritten in terms of the spectrum of the ground reflectivity, $G(\omega)$ and transmitted signal, $R(\omega)$.

$$S(\omega) = R(\omega)\, G(\omega) \tag{5.3}$$

Summing over a number of range lines will cancel out the effects of $G(\omega)$ which is a random Gaussian variable, revealing the spectrum of the transmitted signal. The shape of $S(\omega)$ is rectangular in range and proportional to the squared Sinc function in azimuth (see Curlander [19, p. 86]) representing the antenna pattern. Therefore this test will also verify that the raw data matrix is oriented with rows corresponding to range lines and columns to azimuth lines. ERS-1 data from the scenes chosen for this study were validated by the above two methods prior to processing.

Figure 5.4a shows the range spectrum, and Figure 5.4b the azimuth spectrum of the raw data from a 512 line by 512 pixel sample of ERS-1 raw data. As expected, the azimuth spectrum reveals the antenna pattern and the range spectrum corresponds to the spectrum of a linear FM signal. If the ground reflectivity were constant, the tilt of the range spectrum

would be a direct function of the transmitted chirp profile. The ERS-1 does not have automatic gain control, however, and the ground reflectivity slope is reflected in the slope of the range spectrum. Therefore the exact envelope of the transmitted signal cannot be recovered from the range spectrum.

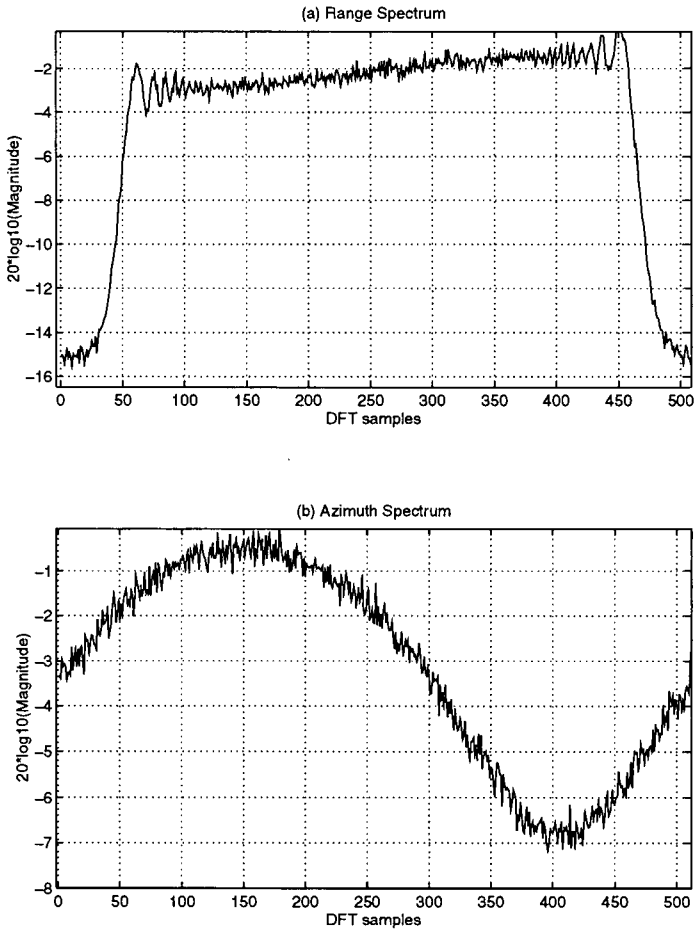

Figure 5.4 Raw data spectrum

Section 5.4 Scenes Chosen for Study

The processing results of four scenes used for the analysis of the SPECAN correction are presented in this thesis. These scenes are chosen to contain combinations of different types of features to demonstrate the performance of the correction scheme on different imaged areas.

The scenes will be named and referred to according to their locations or content as the Nova Scotia ocean scene(A) and (B), the Rhine river scene, and the mountain scene. Each raw

data set is 5616 pixels wide by approximately 30000 lines long (approximately 360 *Mbytes*) corresponding to a 100 *km* by 100 *km* strip of ground.

The mountain scene is of a mountainous, high contrast area; the Nova Scotia(A) scene is of a homogeneous section of the ocean with high raw data saturation at near range; the Nova Scotia(B) scene shows some features of ice and turbulent water; the Rhine river scene shows a sharp radiometric contrast between dark, calm water and bright, turbulent water.

Figure 5.5 shows the histogram of a 500 x 100 sample section of raw data, superimposed is the dotted line representing the expected normal distribution for that particular standard deviation. The histogram shows the frequency percentage of raw data at each of the quantization levels.

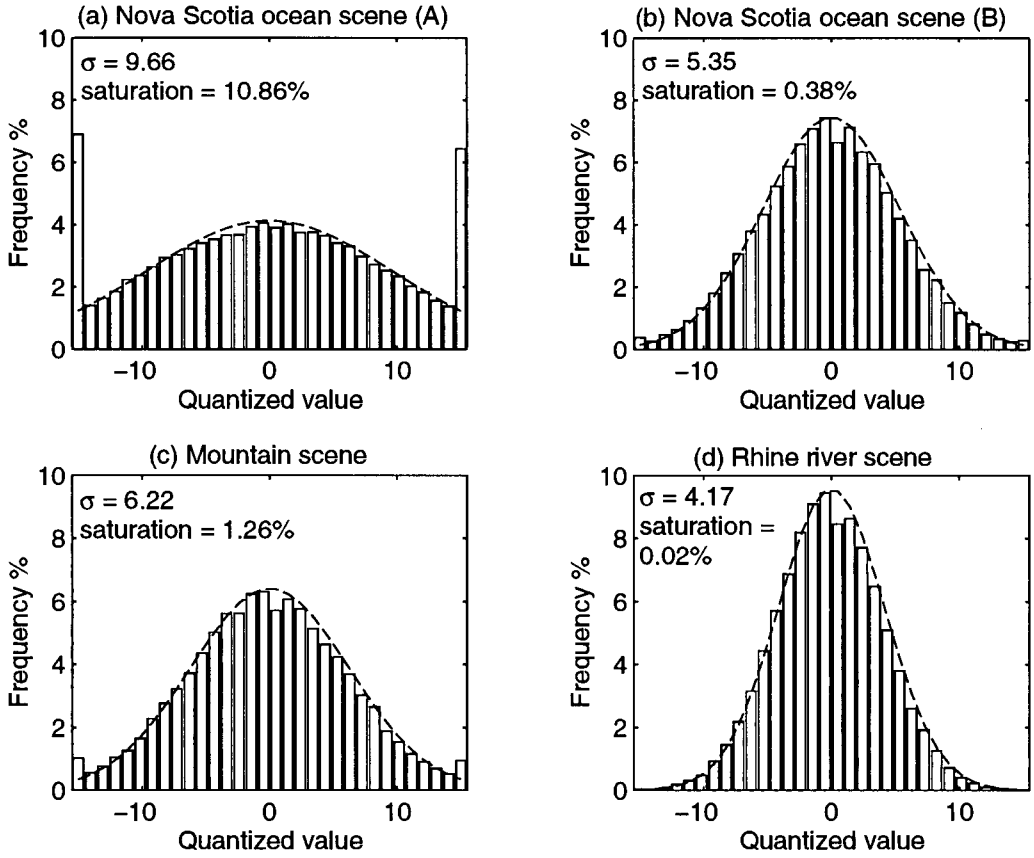

Figure 5.5 Histograms showing distribution of raw SAR data

From the plots we can see that the raw data follows the normal distribution closely in the case of the Rhine scene; the Nova Scotia ocean(B) and mountain scenes show a small degree of

saturation, and the Nova Scotia ocean(A) scene shows a high degree of saturation. The effect of this saturation on the output of SPECAN is described in the next chapter.

Section 5.5 Analysis of SPECAN Output

The degree of scalloping and the effect of the correction scheme will be measured for different scene contents. To show the scene content two quicklook images will be shown of the near and far range sections of the range swath. These images are obtained by compressing 2048 pixel by 2048 line segments of raw data from near and far range. SPECAN and fast convolution are used for range and azimuth compression, respectively. The resulting image is averaged by four in azimuth to make the ground range/azimuth aspect ratio close to one, and to reduce the speckle noise.

Also, for each scene the histogram of three sample sections of the raw data chosen at equal distances from near, mid, and far range will be shown to display the trend in raw data saturation along the range dimension.

To see the scalloping effects, 5000 lines of each scene will be range compressed using SPECAN. The magnitude of the range compressed data is averaged over the 5000 range lines and displayed along with its corrected version. Summing the range lines will cancel out the noise and the random fluctuations due to the scene features resulting in a relatively smooth line disjointed at regular intervals due to scalloping. The sum of the magnitude of the 5000 lines of raw data is also displayed to show the general radiometry of the scene; the shaded sections indicate the segments of raw data which have been used as input to the SPECAN matched filter. For scenes of water where the radiometry is smooth a smaller number of lines are needed to show the scalloping clearly. For scenes of land where the range compressed data has a wider dynamic range and more frequent fluctuations the scalloping effect can be seen better by summing a larger number of range lines.

The amount of scalloping between sucessive blocks is indicated on the figure showing the SPECAN output. The scalloping is measured as the amplitude difference between the first output sample of one block and the last output sample of the preceding block. This measurement does not take into account the fluctuations in the output which are a result of the natural variations in the radiometry. To account for these variations the amplitude difference between adjacent samples is plotted, and the amount of scalloping is alternatively measured as the amount by which the natural radiometry is exceeded at the DFT block boundary.

5.5.1 Nova Scotia Ocean Scene

The Nova Scotia ocean scene was acquired on February 7, 1994 from the ocean off the coast of Halifax. The different image contents cause the top and bottom parts of this scene to have different statistical properties which affect their output after SPECAN compression. Therefore we have divided this scene into two sections and processed each separately. The section towards the top of the scene, referred to as Nova Scotia ocean(A), is 5000 lines of featureless water showing a large amount of saturation in the raw data. Nova Scotia ocean(B) is a 5000 line section towards the bottom of the scene and contains features of new and old ice; the raw data in this section has very little saturation.

Nova Scotia Ocean(A) Figures 5.6 and 5.7 are the quicklook images of Nova Scotia ocean(A).

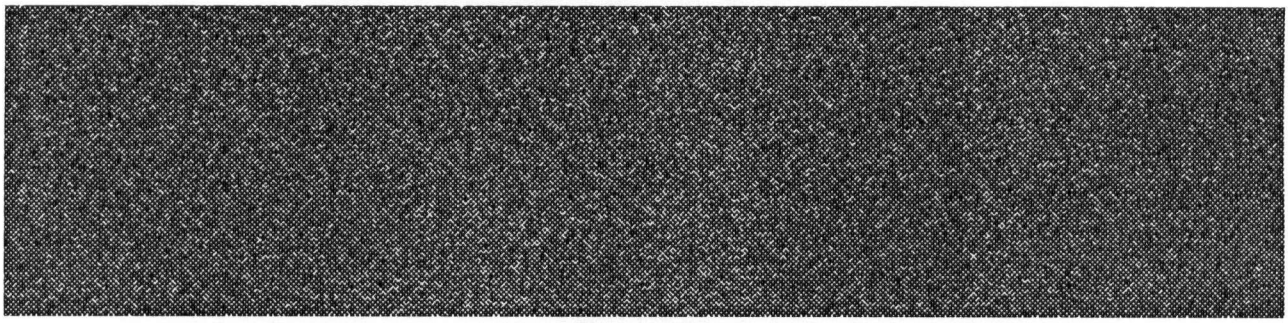

Figure 5.6 Near range image of Nova Scotia ocean(A) scene. Pixels 0 to 2047.

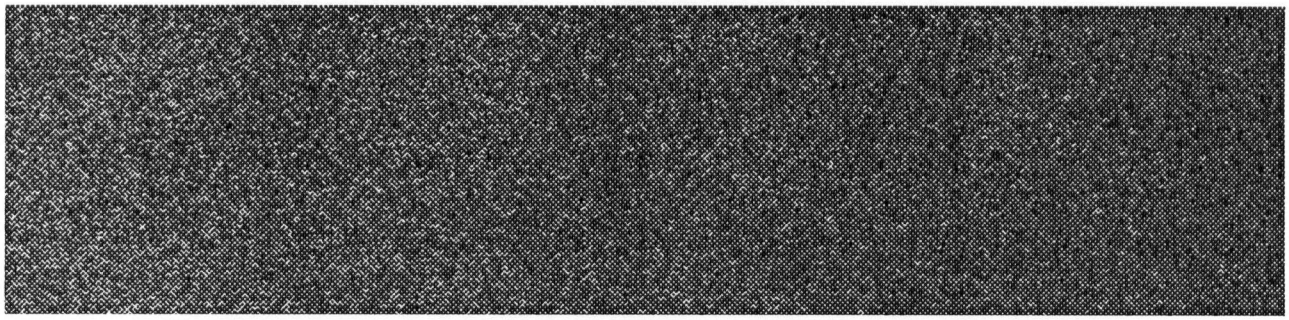

Figure 5.7 Far range image of Nova Scotia ocean(A) scene. Pixels 3500 to 5547.

Figure 5.8 shows the histograms of three sample sections of the raw data chosen at equal distances from near to far range from the Nova Scotia ocean(A) scene. The histogram shows a high degree of saturation at near range. The saturation decreases along the range direction because the power of the received signal decreases along range.

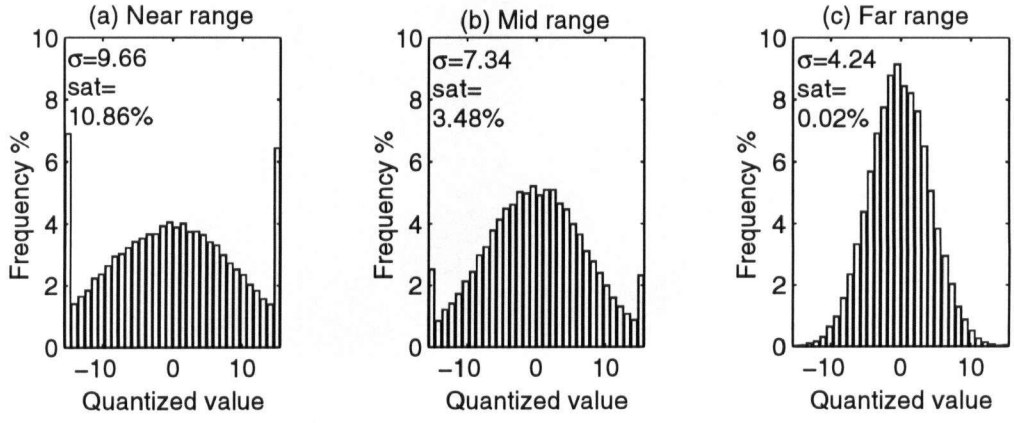

Figure 5.8 Histograms of Nova Scotia ocean(A) raw data

Figure 5.9 shows the result of SPECAN range compression, the chirp replica correction, and raw data range line summation in Nova Scotia ocean(A). The shaded areas in 5.9c, numbered from 1 to 12, indicate the samples of raw data which have been used in the SPECAN processing. The corresponding outputs of each of the input blocks in 5.9a and 5.9b have also been numbered. The scalloping is quite high in the uncorrected output and there is significant residual scalloping in the corrected output.

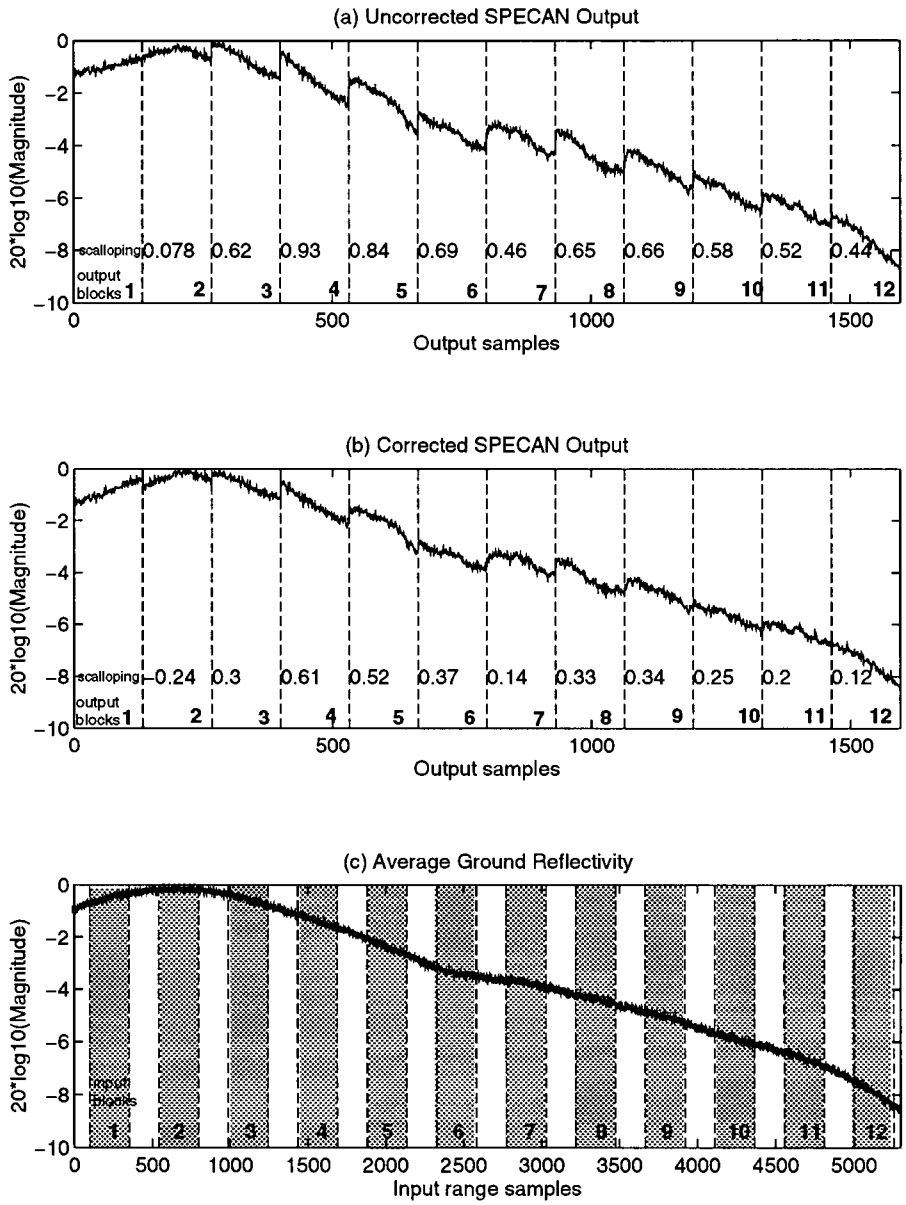

Figure 5.9 Averaged 5000 range processed lines of Nova Scotia ocean(A) (a), (b), average ground reflectivity (c).

Figure 5.10 shows the amplitude difference between adjacent samples of the outputs in Figure 5.9; in the uncorrected output we can easily see how the amplitude difference exceeds that of the neighboring samples at the DFT boundaries. This scalloping is not completely eliminated as seen from 5.10b; especially at boundaries 3, 4, 5, 7, 8, and 9 the residual scalloping is significant.

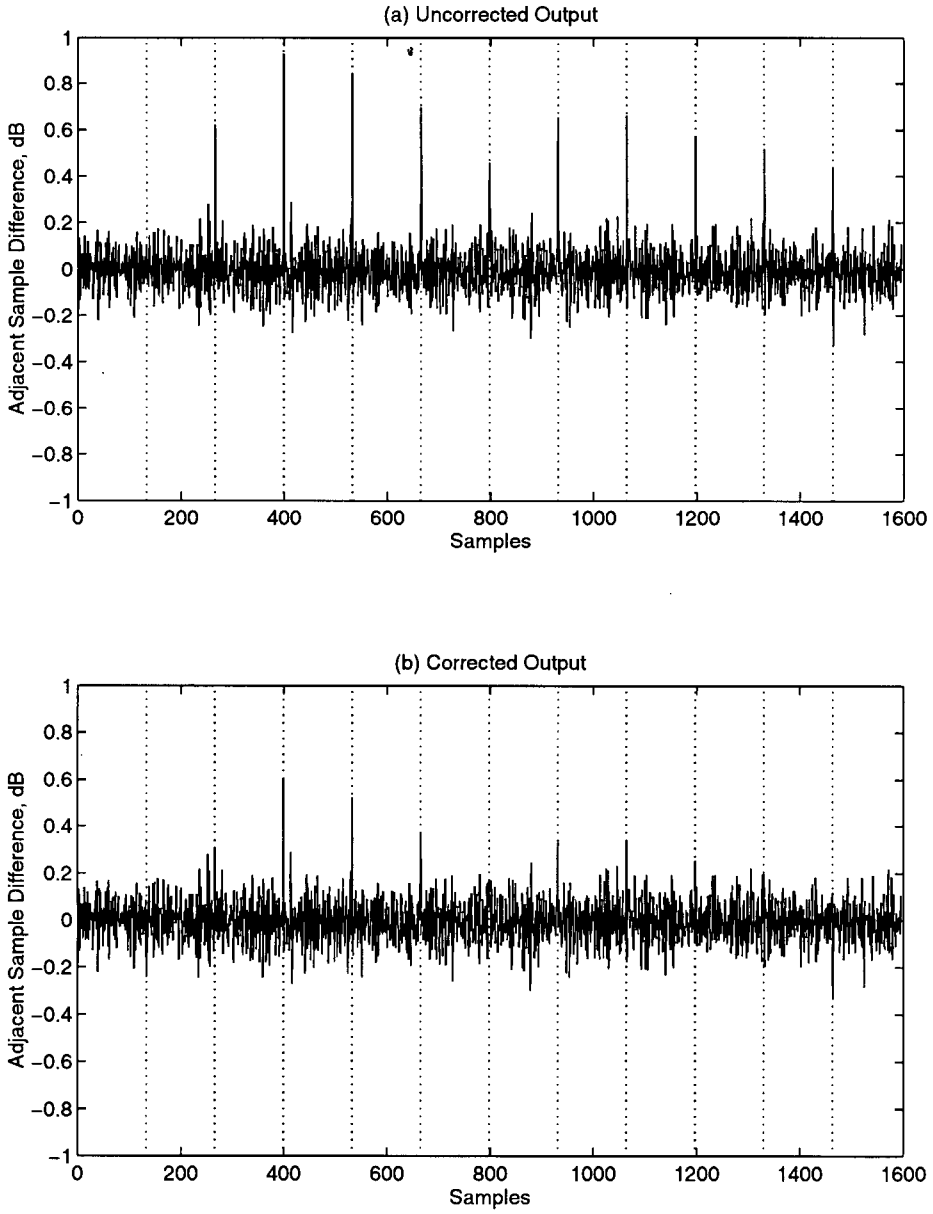

Figure 5.10 Effect of correction scheme on output of Nova Scotia ocean(A) scene

Nova Scotia Ocean(B) Figures 5.11 and 5.12 are the quicklook images of Nova Scotia ocean(B).

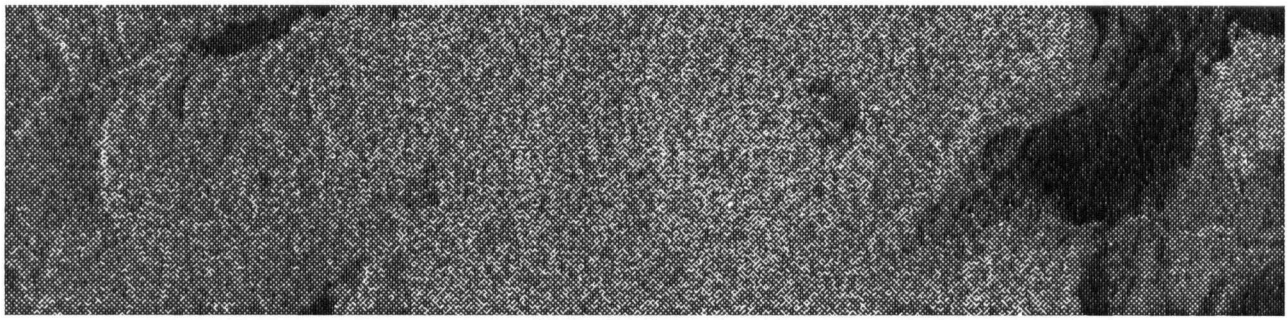

Figure 5.11 Near range image of Nova Scotia ocean(B) scene. Pixels 0 to 2047.

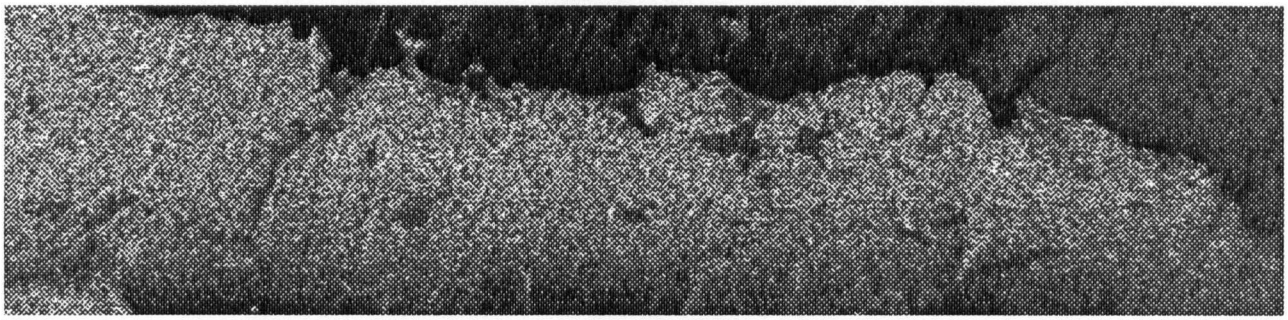

Figure 5.12 Far range image of Nova Scotia ocean(B) scene. Pixels 3500 to 5547.

Figure 5.13 shows the histograms of three sample sections of the raw data chosen at equal distances from near to far range from the Nova Scotia ocean(B) scene. The degree of saturation in this scene is far less than the Nova Scotia ocean(A) scene. Note that the missing bin in 5.13c could be due to an error in the ADC in that portion of the data. Figure 5.14 shows the range–SPECAN output of Nova Scotia ocean(B).

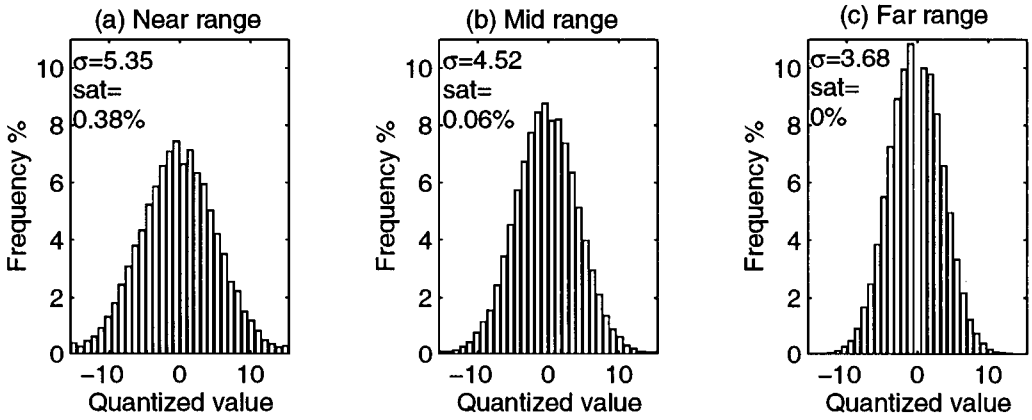

Figure 5.13 Histograms of Nova Scotia ocean(B) raw data

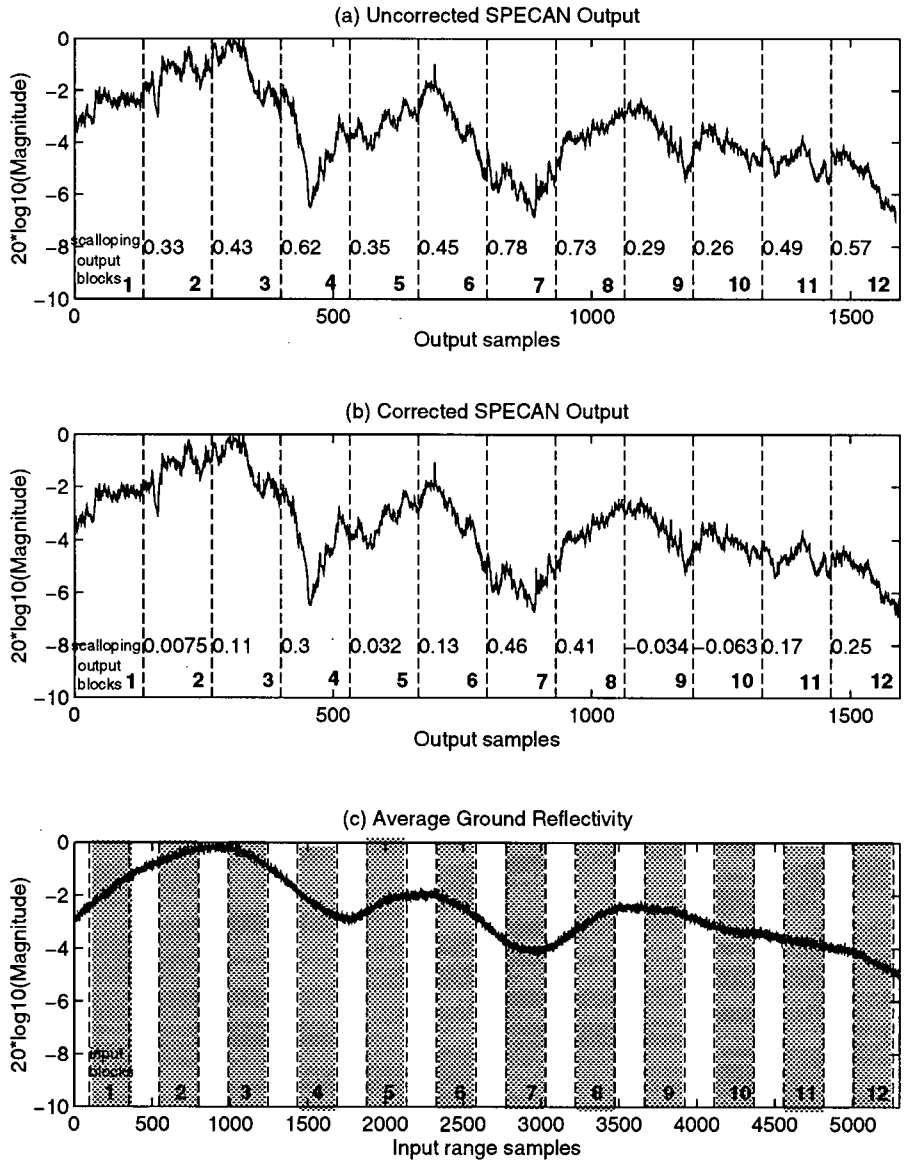

Figure 5.14 Averaged 5000 range processed lines of Nova Scotia ocean(B) (a), (b), average ground reflectivity (c).

The amount of scalloping at the DFT boundaries is illustrated in Figure 5.15. This figure illustrates that after correction the amplitude difference at the DFT boundaries is reduced to values within the natural variations expected in this particular scene, and that scalloping is not noticeable in scenes with contrasting features.

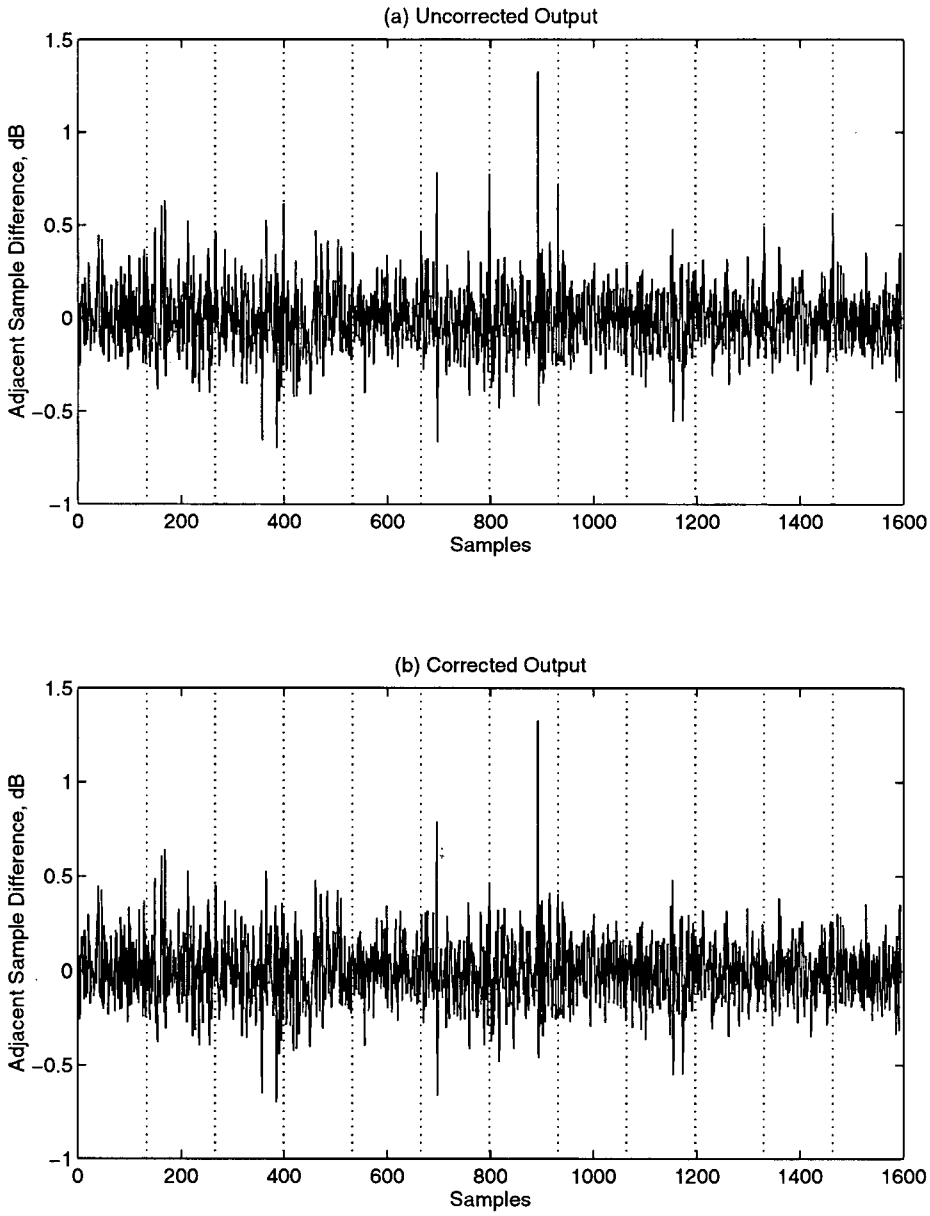

Figure 5.15 Effect of correction scheme on output of Nova Scotia ocean(B) scene

The Nova Scotia ocean(A) shows unexpectedly high amounts of scalloping at near range (Figure 5.9a) tapering to approximately the predictable[2] amount at far range; correspondingly, Figure 5.8 shows a high amount of raw data saturation at near range, decreasing to no saturation at far range for Nova Scotia ocean(A). The scalloping at far range is almost completely eliminated by the correction scheme.

Figure 5.13 shows the amount of saturation is low all across range for Nova Scotia ocean(B). Correspondingly, Figure 5.14a shows the amount of scalloping does not have a particular trend with range. The corrected output in 5.14b shows no visible scalloping which is verified by 5.15b.

5.5.2 Rhine River Scene

The Rhine river scene was acquired on April 8, 1993 from the North Sea, adjacent to the mouth of the Rhine river, along the coast of Holland.

The Rhine river scene is divided into sections of bright water, dark water, and land. Figure 5.16 is the quicklook image from near range of this scene. The bright area to the left shows the choppy waters of the North Sea; the darker areas in the middle and to the right show calmer waters. The bright spots in the middle of the scene are reflections from ships in the water. Figure 5.17 is the quicklook image from far range of this scene. The slanted line across the middle is the land water boundary. The water on the left is more turbulent and therefore brighter, the water adjacent to the land is calm and therefore darker.

---

[2] The predictable amount is that estimated from the chirp replica envelope, i.e. approximately 0.36 *dB*.

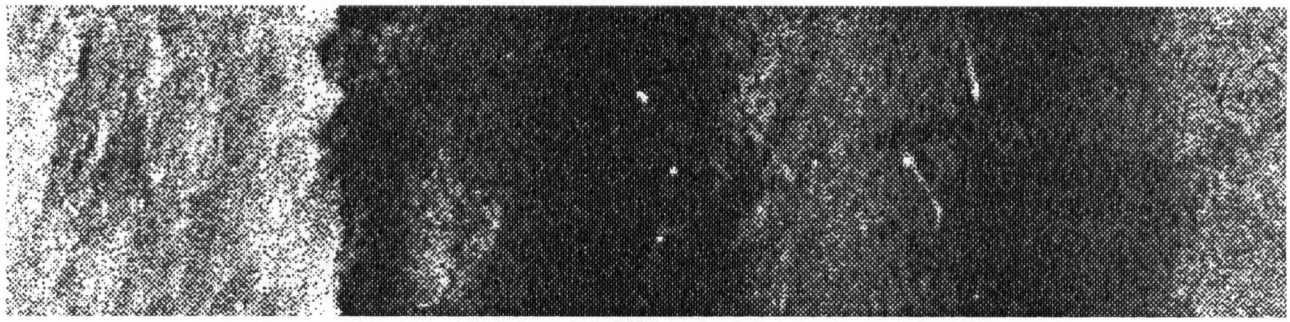

Figure 5.16 Near range image of Rhine river scene. Pixels 0 to 2047.

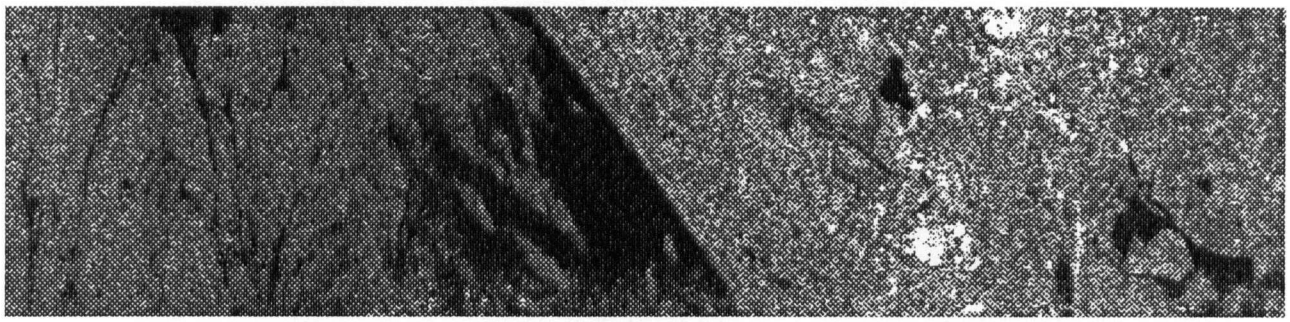

Figure 5.17 Far range image of Rhine river scene. Pixels 3500 to 5547.

As with the Nova Scotia ocean scenes, the histograms of the raw data are included in Figure 5.18 to show the amount of raw data saturation across range. The histograms show that there is very little raw data saturation in this scene at near and mid range. The higher saturation at far range corresponds to the bright reflection from the land seen at far range in Figure 5.17.

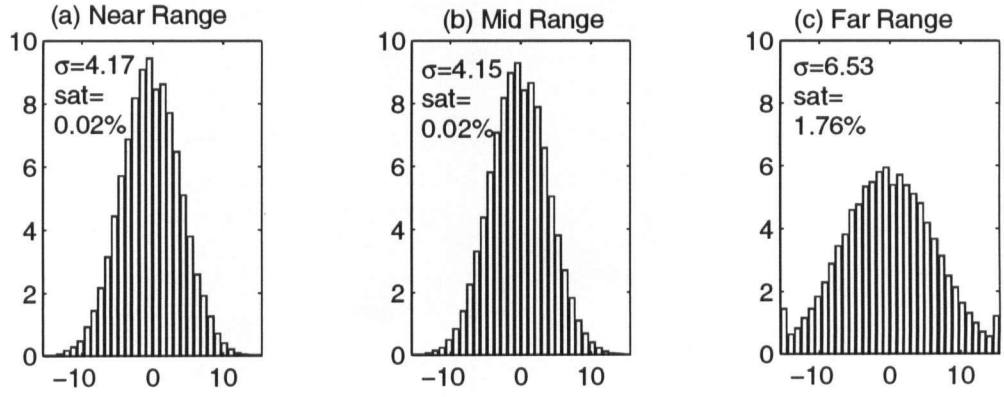

Figure 5.18 Histograms of the Rhine river scene raw data

Figure 5.19a shows the average of 5000 SPECAN range processed lines from the Rhine river scene, the corrected output and the raw data over the 5000 range lines. Note that the high contrast area in blocks 9 to 12 of Figure 5.19 corresponds to the land section in the right-hand half of the image in Figure 5.17.

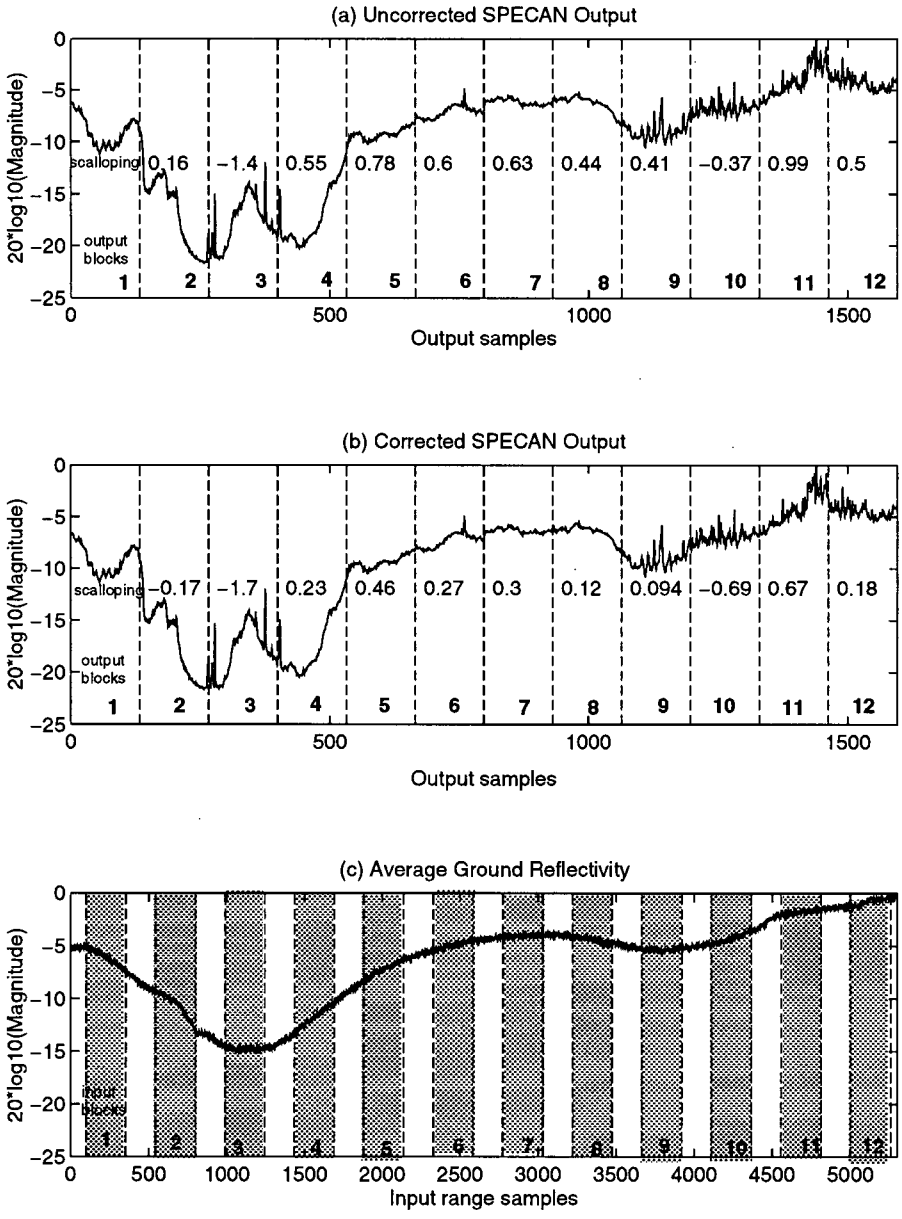

Figure 5.19 Average of 5000 lines of the Rhine river scene

Figure 5.20 shows the adjacent sample amplitude difference before and after applying the correction vector. In Figure 5.20a regular scalloping at the DFT boundaries is observed particularly well from samples 400 to 1100. After correction this scalloping is not observed (Figure 5.20b).

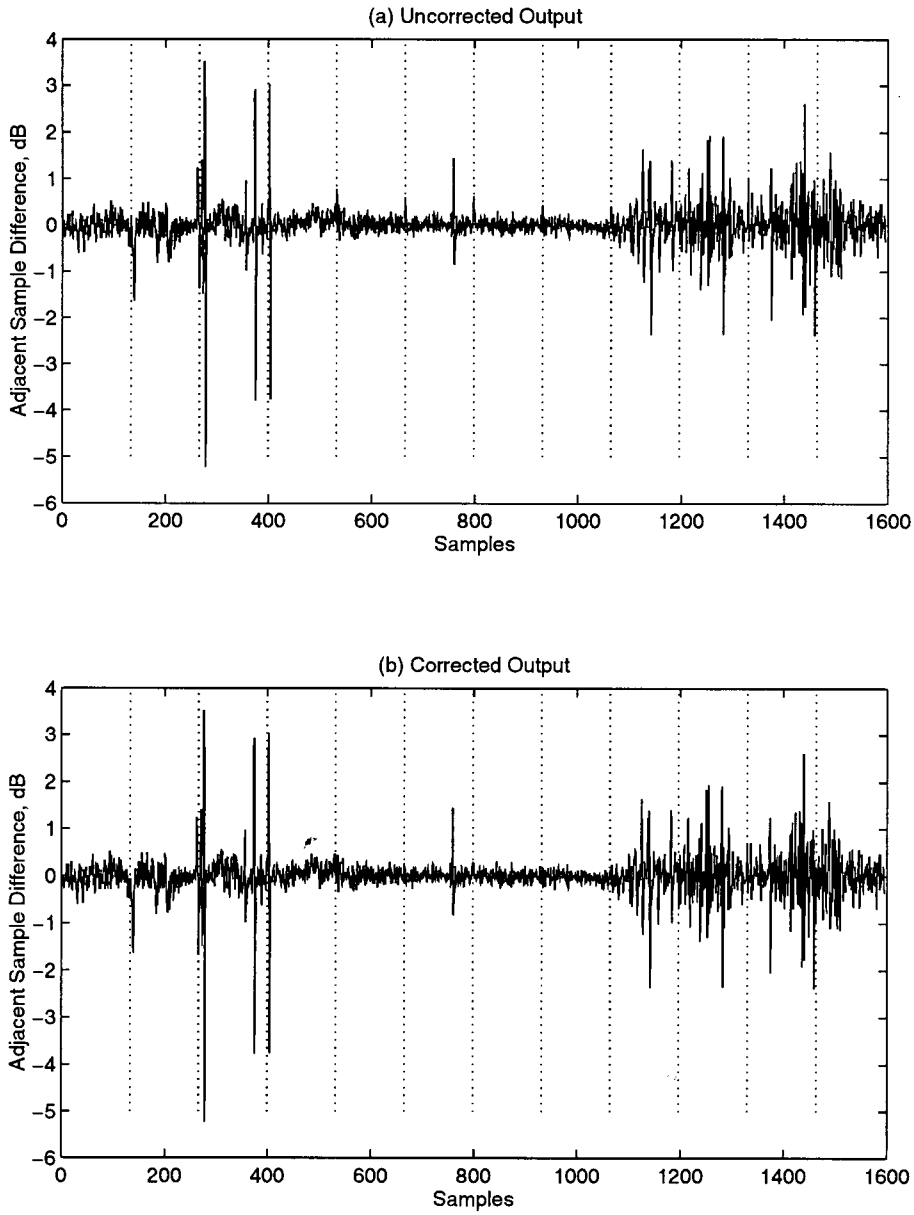

Figure 5.20 Effect of correction scheme on output of Rhine river scene

5.5.3 Mountain Scene

The mountain scene was acquired on May 14, 1993 from Vancouver, B. C. and the surrounding area from Boundary Bay in the south to Whistler Mountain in the north. The section of the scene processed for this analysis is the mountainous area around Whistler, and has the highest contrast of all scenes used for this study. Figures 5.21 and 5.22 show the quicklook images at near and far range.

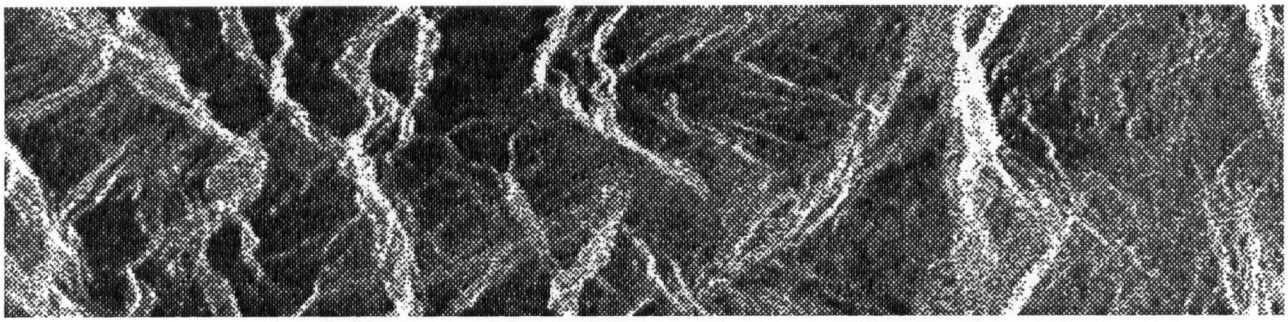

Figure 5.21 Near range image of the mountain scene. Pixels 0 to 2047.

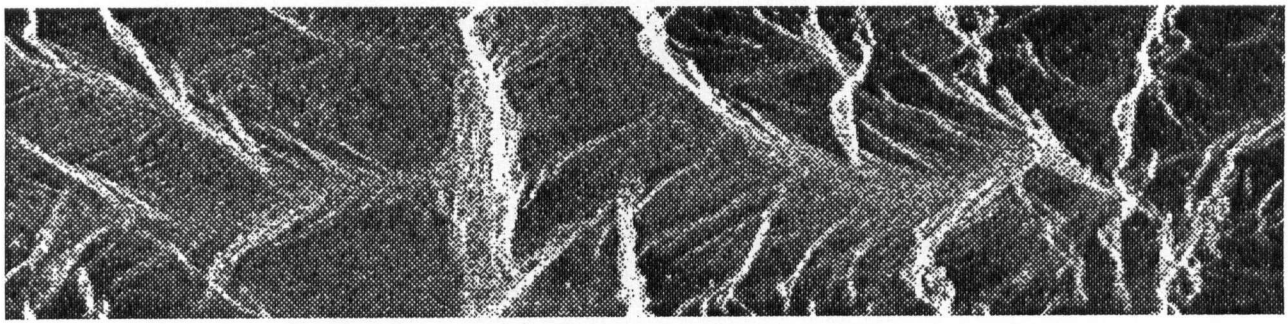

Figure 5.22 Far range image of the mountain scene. Pixels 3500 to 5547.

Figure 5.23 shows the histograms of three sections of the raw data equally spaced along range. There is some saturation in the near and mid range sections of the scene.

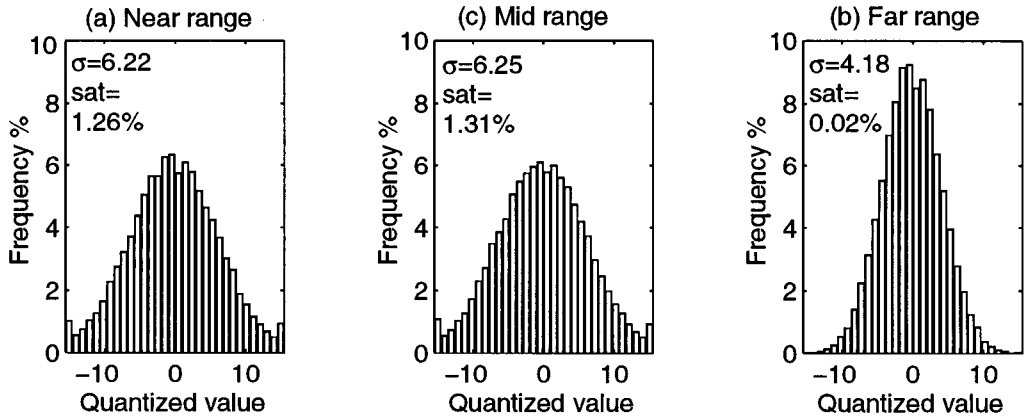

Figure 5.23 Histograms of mountain scene raw data

Figure 5.24a shows the average of 5000 lines of the mountain scene range compressed using SPECAN; 5.24b shows the output of the same scene corrected using the chirp replica, and 5.24c shows the sum of the raw data range lines to show the general radiometry of the scene. Figure 5.25 shows the amplitude difference between adjacent samples before and after correction. The high amount of contrast in this mountainous scene masks the SPECAN discontinuities such that even before correction no scalloping is visible.

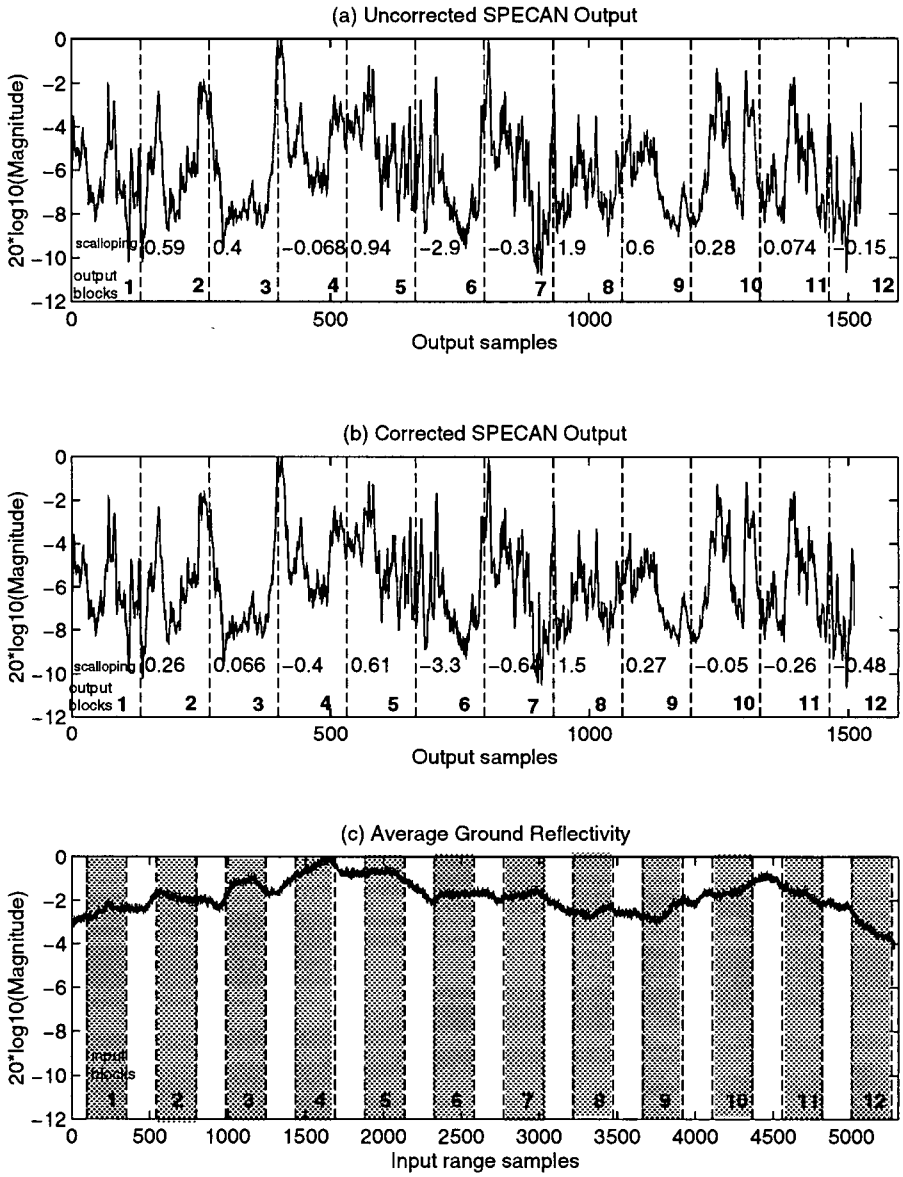

Figure 5.24 Average of 5000 lines of the mountain scene

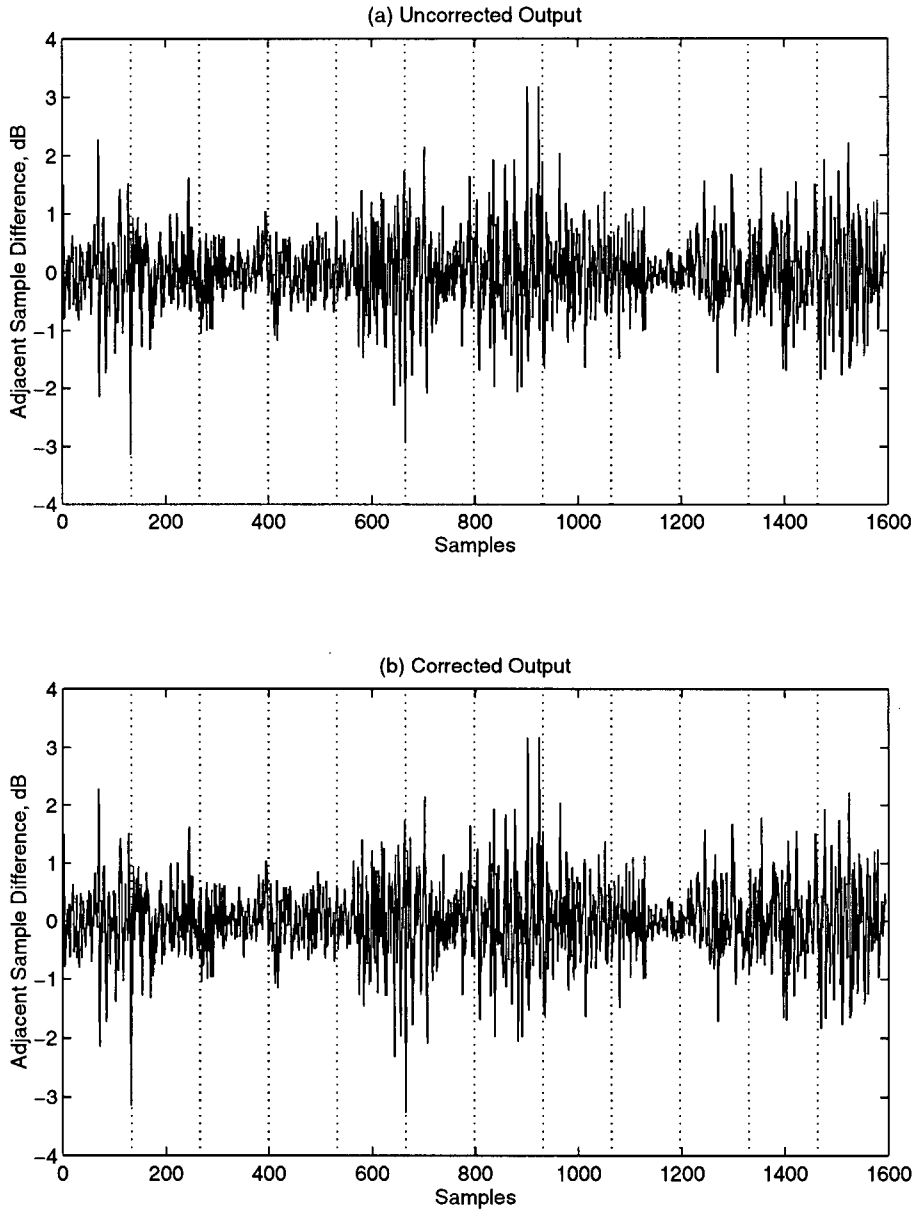

Figure 5.25 Effect of correction scheme on output of mountain scene

This chapter has shown that the degree of scalloping varies from scene to scene, and from near to far range in each scene. Significant scalloping is observed in scenes with low contrast features, and particularly in the sections of these scenes which have high degree of raw data saturation. The next chapter will discuss the effects of raw data saturation on SPECAN scalloping.

Chapter 6 Effects of Raw Data Saturation on SPECAN Scalloping

In this chapter the effects of saturation in the ERS-1 analog to digital converter on scalloping are analyzed.

Scalloping is caused because of the amplitude difference between the beginning and end of the transmitted chirp. Because the transmitted chirps are almost identical the amount of scalloping should be the same in all scenes. However, as graphs in the previous section indicate, the amount of scalloping varies from scene to scene and with the range axis in each scene. Examining the raw data shows that a direct correlation exists between the degree of saturation in the raw data and the amount of scalloping. This section of the thesis will examine this correlation and verify that saturation in the raw data is the main reason for the very high scalloping observed in some scenes.

Section 6.1 Scene Content and Saturation

In some scenes the amount of scalloping is constant across range and corresponds to the slope of the transmitted pulse as predicted in Chapter 4. In these scenes the amount of scalloping is approximately 0.4 *dB*. This small degree of scalloping is still large enough to be seen in uniform, low contrast scenes, and is therefore worth correcting. The scalloping in these scenes is removed by the correction scheme of Chapter 4.

For other scenes, however, the amount of scalloping varies across range: high at near range and decreasing gradually to the predicted value at far range. This variation may be explained by the degree of saturation in the raw data. Because there is no automatic gain control incorporated in the ERS-1 receiver, saturation will occur unpredictably. It has been observed in this study

that scenes of turbulent water contain the highest degree of saturation and show scalloping much higher than the expected value.

The above findings are verified by contour plots of the raw data standard deviation of areas around the English Channel made by Laur [37, p. 269]. These plots show that the standard deviation of the raw data decreases from near to far range, and that the standard deviation is particularly high (around 9.5) over the sea.

The saturation affects the output of SPECAN at the DFT boundaries increasing the amount of scalloping in proportion to the degree of saturation. The following sections will attempt to verify this finding and propose a solution to overcome the excessive scalloping caused by raw data saturation.

Section 6.2 Further Saturation of Raw Data Prior to Range Processing

To verify that the extra scalloping seen at near range is due to saturation, data from the Nova Scotia ocean scene was subjected to further saturation prior to SPECAN range processing, and the amount of scalloping was measured for each degree of saturation. This will verify whether the trend of increased scalloping will continue with further saturation. The raw data is received in quantized form, therefore the only way to see the effect of further saturation is to reduce the number of quantization levels. The degree of saturation is measured as the number of samples in the first and last bins of the histogram *in excess* of the expected number of samples in those bins as expected by the standard deviation.

The scalloping increased in proportion to the amount of saturation. Figure 6.1 shows the range line averaged output of four DFT blocks from the Nova Scotia ocean scene far range region before and after saturation. σ is the standard deviation of the raw data of the input block, and s is the percentage saturation.

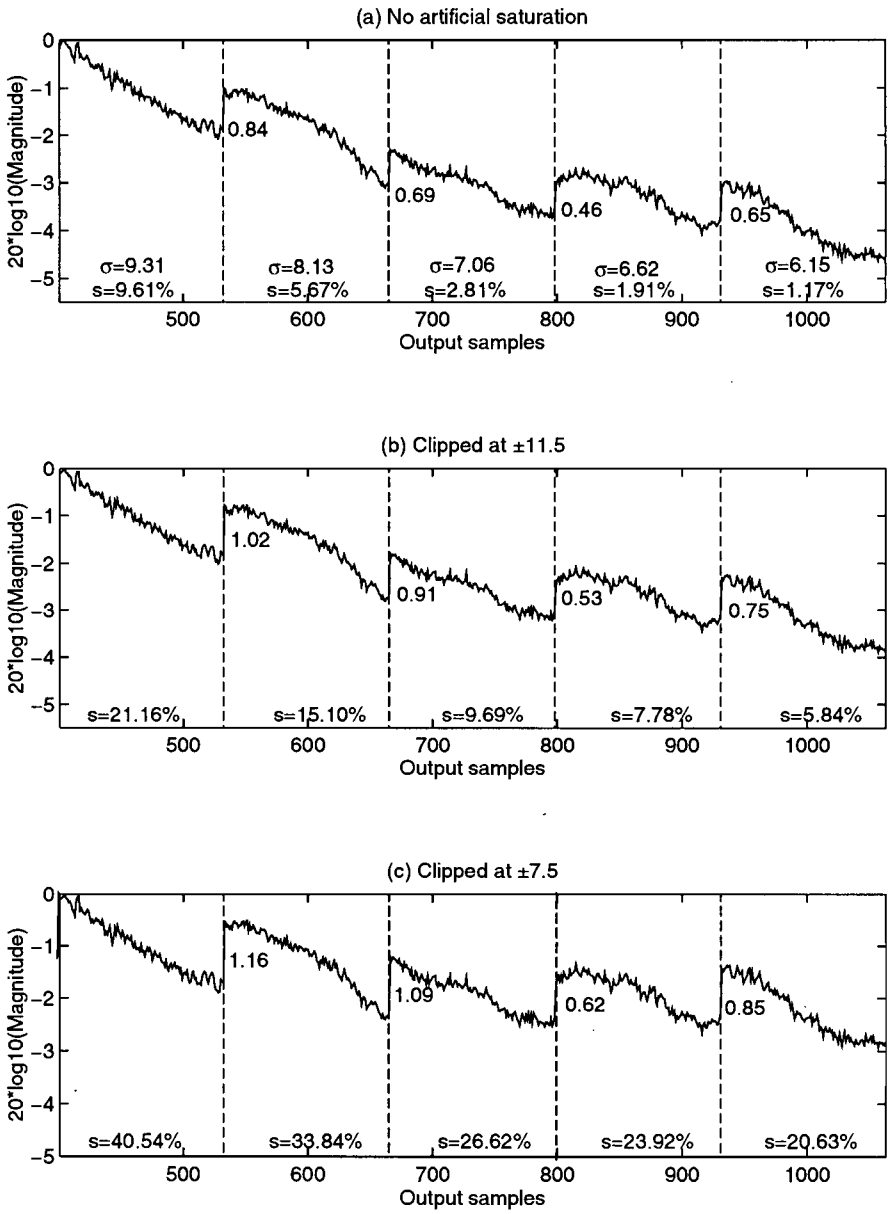

Figure 6.1 Effect of introducing excess clipping in raw data prior to SPECAN range processing.

To better see the trend of scalloping versus raw data saturation, raw data from the Nova Scotia ocean scene was clipped at 9 levels: ±15.5, ±14.5, ±13.5, ±12.5, ±11.5, ±10.5, ±9.5, ±8.5, ±7.5; the scalloping is plotted against the standard deviation of the raw data in that block for each clipping level. Figure 6.2 shows four of the resultant scalloping versus saturation plots, where the points (circles on the plot) are fit to a first or second order polynomial (solid line). The block number refers to the position of the block in range where there are 12 blocks as seen

in Figure 5.9. The standard deviation, $\sigma = \sqrt{\frac{\sum_{i=0}^{N-1}(x_i - m_x)^2}{N-1}}$, is a measure of the total power of the quantized signal.

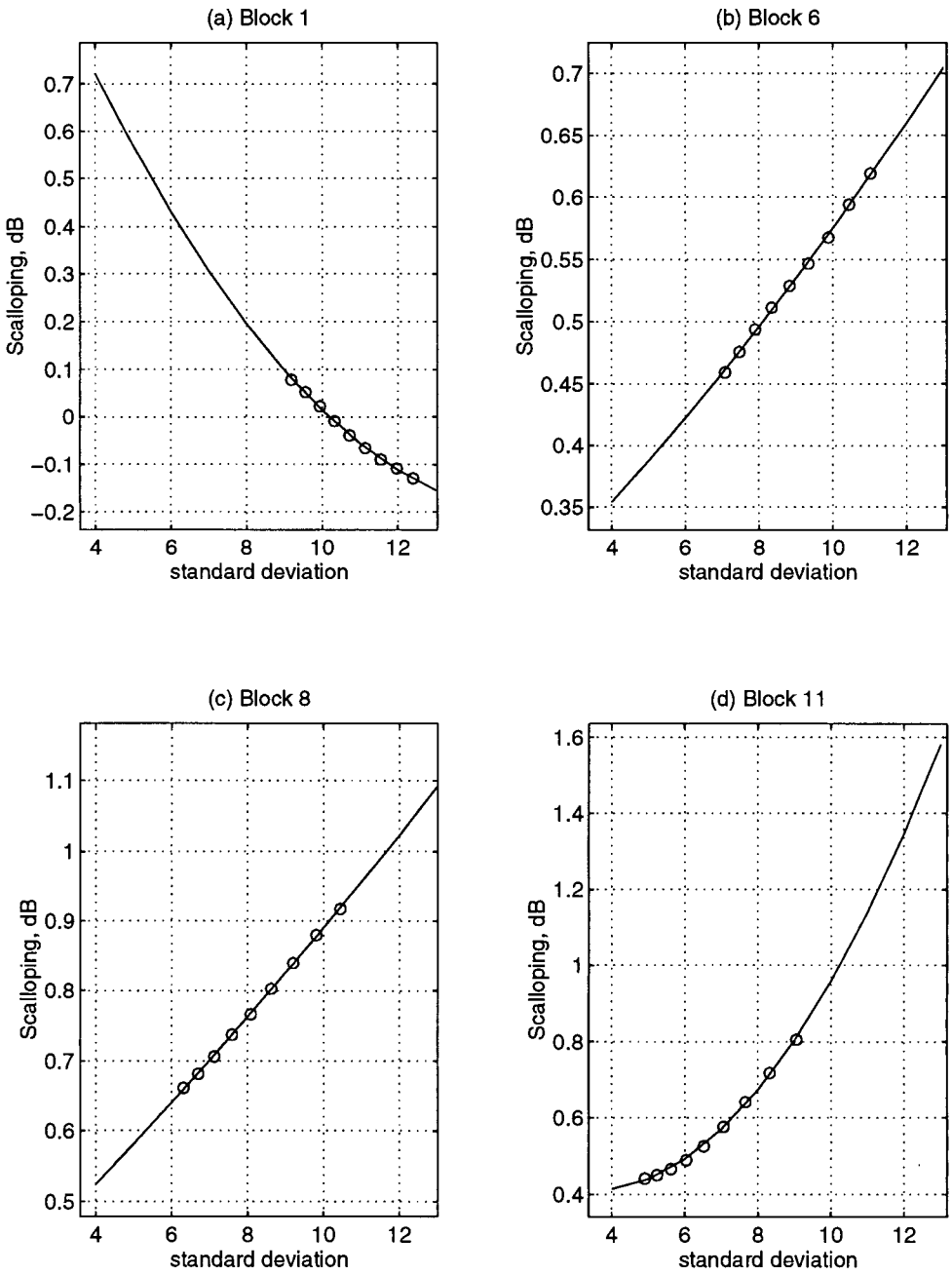

Figure 6.2 Relationship between scalloping and saturation

With the exception of block 1, all the blocks show an increase in scalloping versus saturation such that at zero saturation the scalloping can be predicted to be approximately 0.4 *dB* which is the amount expected from the chirp replica amplitude. As we investigate the mechanism by which saturation affects scalloping the reason for the anomalous result in block 1 will become evident.

Section 6.3 Effect of Saturation on Range Scalloping

Comparing Figures 6.1a, b and c, we are able to ascertain the effect of saturation on the SPECAN output. The following paragraphs explain this effect, which is verified by a raw data simulation in the next section.

Saturation in the ERS-1 raw data occurs as a result of underestimation of the dynamic range of the input signal to the ADC. In this case, the signal is overamplified, and its dynamic range exceeds that of the quantizer. This results in overall loss of power in the ADC output.

To demonstrate this, data sets with Gaussian distribution and varying standard deviations are simulated. Figure 6.3 shows three examples of data with standard deviations of 5, 9, and 13. To simulate the effect of the ERS-1 ADC operation, each data set is clipped at the dynamic range of the ADC, i.e. at ±15.5. The power loss at each value of standard deviation is the corresponding shaded area.

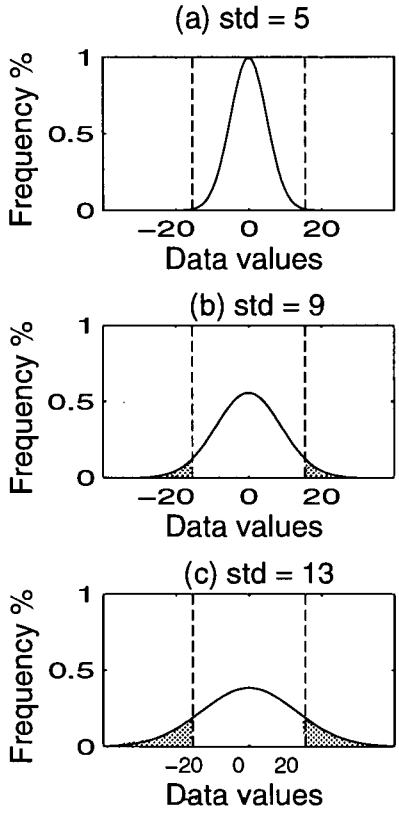

Figure 6.3 Demonstrating power loss with increasing standard deviation for fixed ADC range.

The power loss was calculated in the manner described above for Gaussian data sets with standard deviations ranging from 5 (corresponding to no saturation for the 5 bit quantized data) to 20. The result is plotted in Figure 6.4.

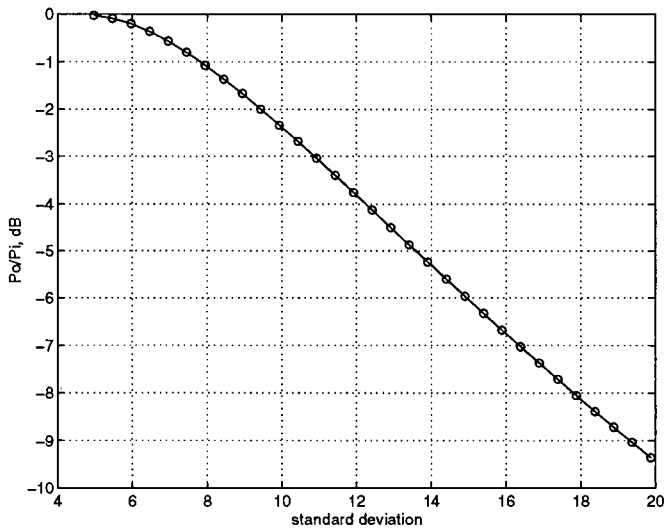

Figure 6.4 Output power loss as function of increasing input power of signal to ADC.

The general trend of scalloping, particularly clear from Figure 5.10 is that of an initial increase, and then a gradual decrease in the degree of saturation across range. This corresponds to the power of the received signal. Because of the gap in the raw data between the blocks chosen for compression, the degree of saturation in each input block is different from its surrounding blocks; this results in a different average power from the original output for each block. (The original output refers to the output had the dynamic range of the input signal been estimated correctly). As the blocks are concatenated, the different displacements cause a sudden power difference at the DFT boundaries, which is seen as scalloping.

Figure 6.5 shows an example of nine SPECAN output blocks (A), the cumulative effect of saturation (B), and the chirp profile (C). For the case where the raw data is not saturated the output blocks fit together smoothly (plot A). Where the raw data has been saturated prior to processing each output block suffers a loss of power compared to output A represented by one of the values of a1 to a9. This causes a sudden jump in output power between two blocks (plot B). Because of the shape of the ground reflectivity function the scalloping resulting from saturation is negative when the ground reflectivity has an positive slope (blocks 1 and 2), and is positive when the ground reflectivity slope is negative (blocks 3, 4, 5, 6, 7, 8, and 9).

The shape of the chirp amplitude envelope causes a droop towards the end of each output block (from Figure 4.7 in Chapter 4). The direction and amount of this droop is not related to the slope of the ground reflectivity. This droop adds to the results of saturation, increasing the scalloping when the ground reflectivity has negative slope, and decreasing the scalloping when the ground reflectivity has positive slope (plot C).

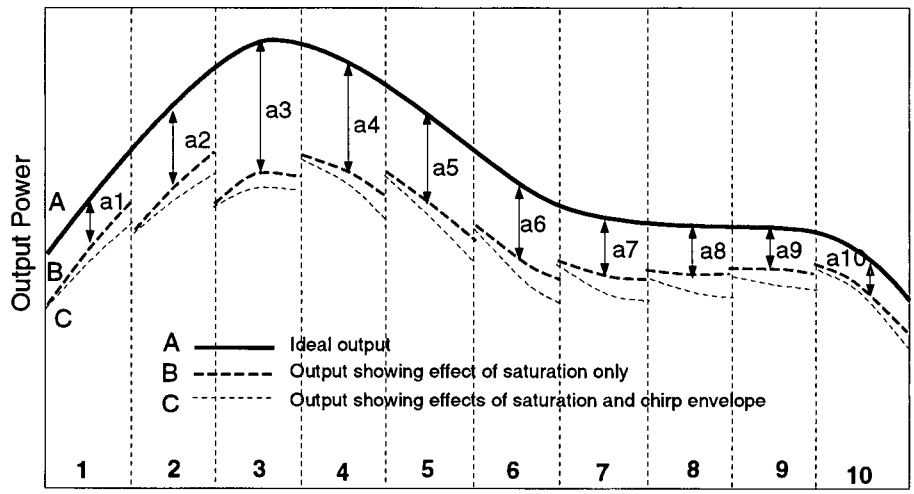

Figure 6.5 Plot A shows the ideal output, plot B shows the result of saturation on the output, and plot C shows the result of the combination of chirp amplitude and saturation.

For output block 1 in Figure 6.5 the ground slope is in the same direction as the chirp amplitude slope; as a result, the effect of the chirp amplitude counters the effect of the saturation and the total scalloping decreases. This effect is the reason for the unexpectedly low scalloping seen in the first output block of Figure 5.9a, and the overcorrection in 5.9b. This also explains why the slope of the scalloping versus saturation curve is negative in Figure 6.2a.

Section 6.4 Raw Data Simulation

To fully understand the mechanism by which saturation affects the amount of scalloping it is necessary to compare the output before and after saturation. Real SAR data can be further saturated by reducing the quantization levels as shown in Figure 6.1, however to *isolate* the effects of saturation, especially from the effects of the chirp envelope, it is necessary to simulate the case where the transmitted signal is ideal, and the only factor affecting the output is saturation.

The point target model is the first choice in simulating the effects of changing parameters in SAR processing. SAR processing is a linear operation (up to the final stage which is detection) and by the principle of superposition the results from the point target simulation may be applied to real data. However, repeating the point target simulation of the previous chapter and saturating

the data before compression will not increase our understanding of the way saturation affects SPECAN processing. The harmonics created in the spectrum of the signal due to saturation add up in a deterministic pattern which depends on the spacing between the point targets. This pattern is repeated with each DFT block, showing an effect which is similar to scalloping but is only a result of the addition of harmonics in a certain pattern. The most significant effect of saturation on real data is a loss of power; not distinct harmonics. Another reason for the unsuitability of point target simulation in this case is that the results cannot be extended to real data because saturation is a non-linear operation.

6.4.1 Model

To properly simulate the effects of saturation it is necessary to have as realistic a model of the received signal as possible. For this, received raw data was simulated using the statistical properties of SAR signals. Various raw signal simulators of three-dimensional scenes have been presented such as the one by Franceschetti, et al. [40], but for the purpose of this experiment only a simple model is considered as follows.

The backscatter received from each sampling cell in slant range will be the sum of the reflection of the many point scatterers in that cell. These reflections will add up coherently resulting in *speckle*, which is the grainy appearance of SAR images as described by Elachi [10]. The signal received from each cell in slant range, therefore, will be a delayed version of the transmitted signal, with a random amplitude and phase.

The simulation is implemented by convolving the transmitted signal with the complex Gaussian random vector representing the ground reflectivity. The transmitted signal is an ideal linear FM ramp simulated using the ERS-1 parameters as outlined in Table 5.1. As a result of introducing the random complex ground reflectivity, and a reflection from every resolution cell, there will be no distinct harmonics as in the point target simulation.

The simulated raw data was quantized to 5 bit values before input to the SPECAN processor. Using knowledge of the dynamic range of the data, the quantizer levels were chosen to minimize saturation. To simulate saturation, the raw data was multiplied by a scalar to simulate a stronger reflection while keeping the minimum and maximum levels of the quantizer unchanged.

6.4.2 Simulated Cases

The received power along the imaged swath is dependent upon the SAR viewing geometry, the antenna gain pattern, and the terrain type as explained by Hawkins [41]. In many SAR systems this dependence is estimated, and a *sensitivity time control* (STC) function with the inverse shape is implemented to flatten the response and minimize saturation (see Teany [42]). This is not done in the ERS-1 satellite, however, and range attenuation of the raw data must also be simulated.

The raw data was simulated using the following four situations.

a. Ground reflectivity is constant across range representing ideal ground reflection, the chirp amplitude is constant, representing the ideal transmitted signal.
b. Ground reflectivity varies across range representing the actual range attenuation, the chirp amplitude is constant.
c. Ground reflectivity is constant across range, the chirp amplitude has a positive slope representing the actual transmitted signal.
d. Ground reflectivity varies across range, the chirp amplitude has a positive slope. This represents the actual received data.

The simulated chirp was multiplied by the function in Figure 6.6a to simulate the transmitted pulse envelope in cases c and d. The simulated ground reflectivity is multiplied by the function in Figure 6.6b to simulate the range attenuation in cases b and d. The pulse envelope function has been exaggerated with respect to the actual function to emphasize the output results.

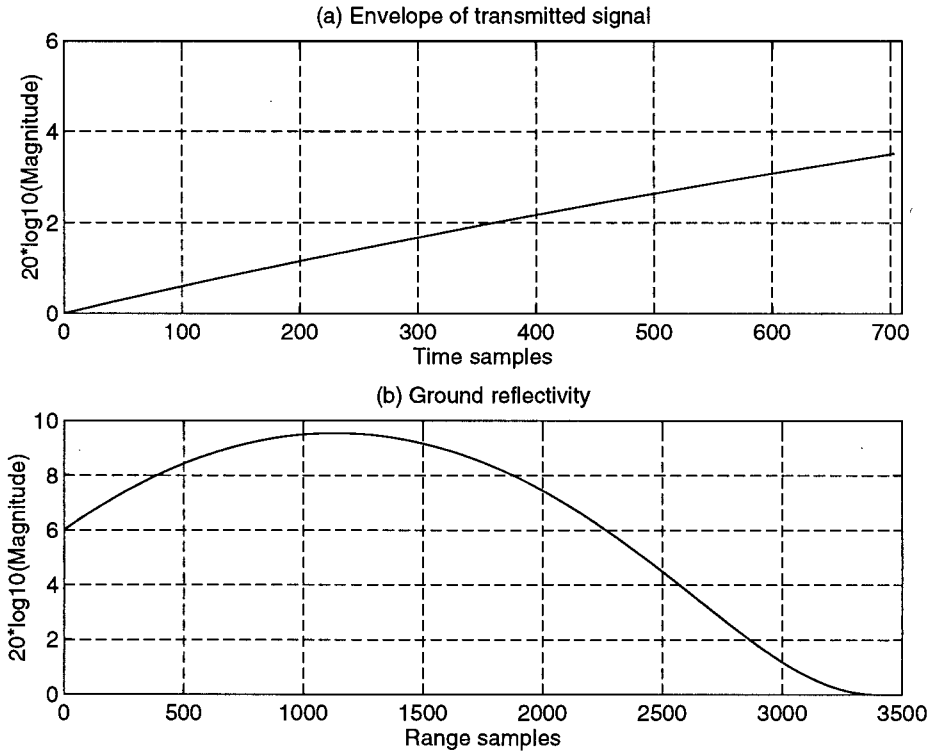

Figure 6.6 Simulated ground reflectivity and transmitted chirp envelope

6.4.3 Output

For each of the cases a to d, SPECAN range processing was performed on 2000 lines of simulated data, and 2000 lines of the same data after it was saturated and the averaged results for each case are shown in Figures 6.7 to 6.10. For cases b and d, the saturation will vary across range as a result of the varying ground reflectivity strength. For cases c and d the output is corrected using the correction scheme derived from the chirp envelope in Figure 6.6a. The scalloping shown on the blocks is measured as the amplitude difference between the last and first samples of adjacent blocks.

For each of the four cases the averaged results for the saturated and unsaturated cases are compared. Figure 6.7 shows the case where the ground reflectivity values constitute a Gaussian distribution, and the transmitted chirp has a completely flat envelope. In this case no scalloping is observed as a result of raw data saturation.

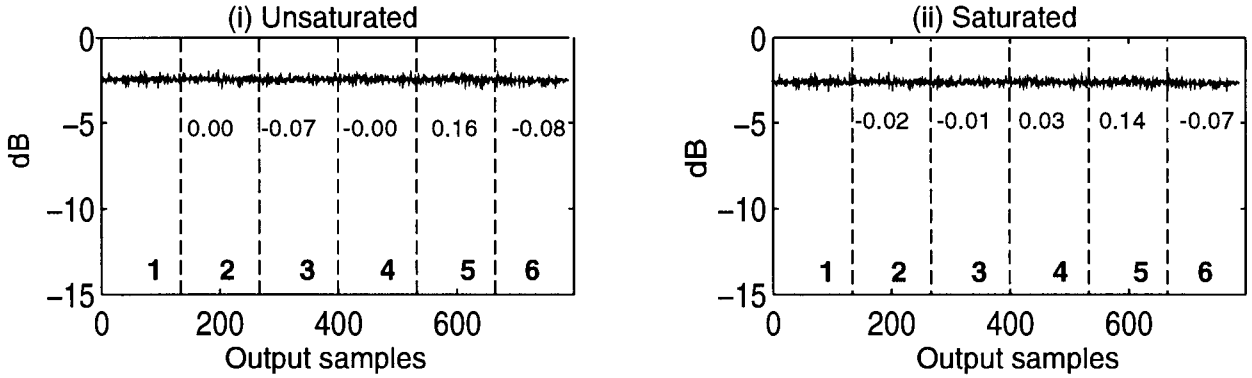

Figure 6.7 SPECAN output, constant chirp amplitude and constant ground reflectivity.

The most interesting result is derived from Figure 6.8 where the ground reflectivity varies along range according to the function in Figure 6.6b, and the transmitted chirp has constant amplitude. The results in this case could not be derived using real data, since all data is affected by the non-ideal chirp envelope. The discontinuity seen at the DFT boundaries in Figure 6.8 verifies the theory that the varying chirp amplitude is not the only cause of scalloping, and the combination of raw data clipping and varying ground reflectivity also creates a time varying scalloping effect. The sign of this discontinuity is opposite to the ground reflectivity slope.

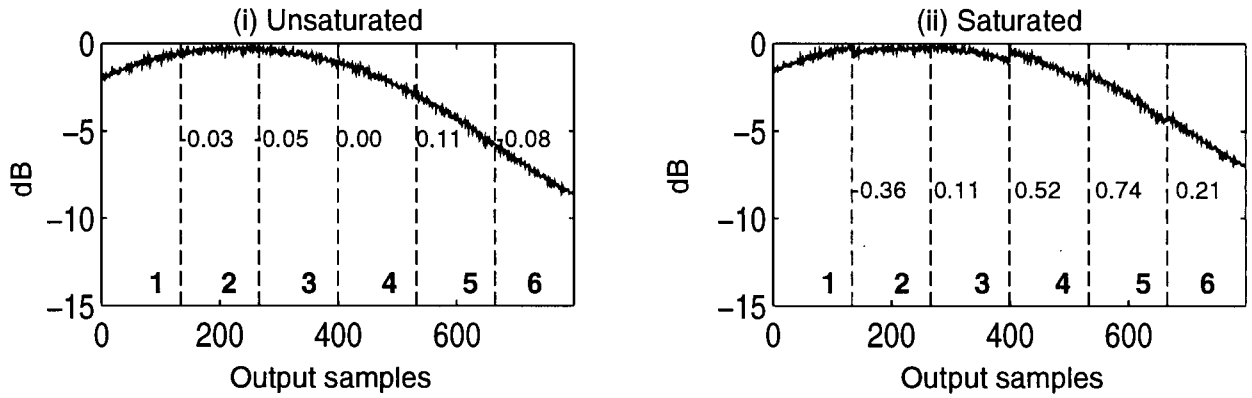

Figure 6.8 SPECAN output. Varying ground reflectivity, constant chirp amplitude.

Figure 6.9 shows that when the ground reflectivity is constant across range, the effect of saturation will be a constant power loss over each DFT block which decreases the degree of scalloping. The correction method will largely reduce the scalloping in the unsaturated case and result in overcorrection in the saturated case. This overcorrection which results from saturation and a completely flat ground reflectivity has not been observed with real data. However, in systems other than the ERS-1 SAR, which may contain automatic gain control, it may be necessary to correct for this effect.

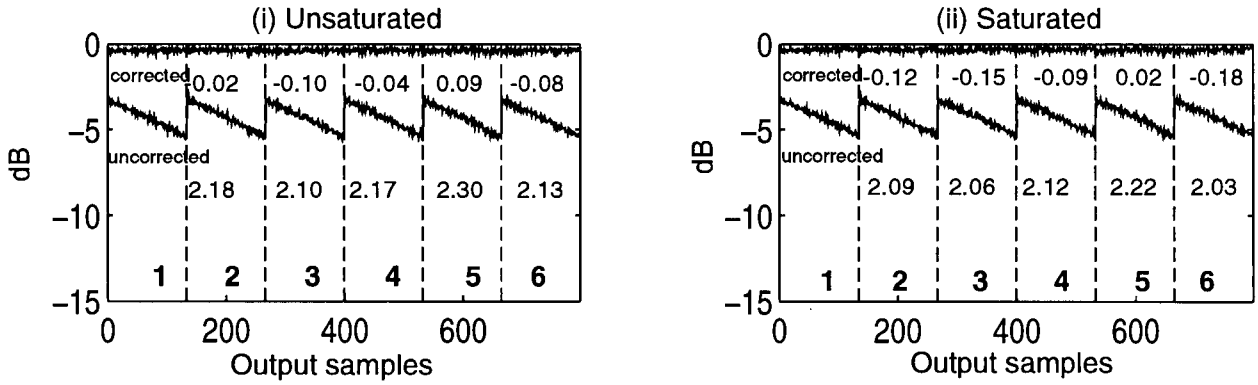

Figure 6.9 SPECAN output. Constant ground reflectivity, positive slope on chirp envelope.

Figure 6.10 shows the output where the ground reflectivity varies with respect to range and the envelope of the transmitted chirp has an positive slope. The results in this case model real data. The correction scheme effectively eliminates the scalloping in the absence of saturation as seen in Figure 6.10i. Clipping the data prior to processing, however, significantly affects the scalloping. For ground reflectivity having positive slope the scalloping decreases after saturation, resulting in overcorrection after applying the correction function. For ground reflectivity having negative slope, the scalloping increases and the correction function does not fully remove the scalloping, as seen in Figure 6.10ii.

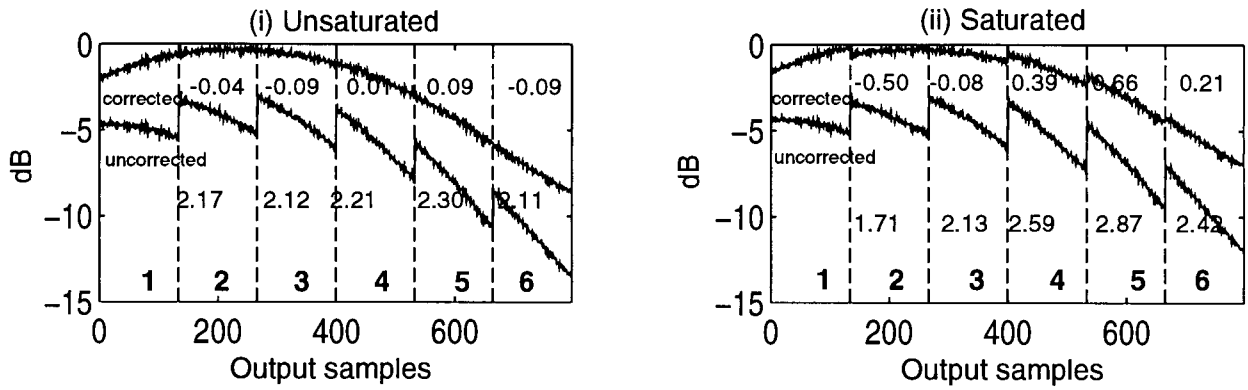

Figure 6.10 SPECAN output. Varying ground reflectivity, positive slope on chirp envelope.

To avoid cluttering the plots, the standard deviation values for each block are summarized in Table 6.4. For the case of Figures 6.8 and 6.10, the varying ground reflectivity causes the degree of saturation to vary across range which in turn creates a varying scalloping effect. In the case of Figures 6.7ii and 6.9ii, although the raw data is highly clipped prior to processing, because the degree of clipping is constant across range, so are the effects of saturation.

	block 1	block 2	block 3	block 4	block 5	block 6
(6.7i) σ	5.69	5.70	5.69	5.70	5.69	5.69
(6.7ii) σ	17.23	17.23	17.05	17.20	17.32	17.17
(6.8i) σ	5.77	6.01	5.89	5.69	5.72	5.84
(6.8ii) σ	10.69	11.71	11.31	9.77	7.55	5.81
(6.9i) σ	5.69	5.71	5.68	5.71	5.70	5.70
(6.9ii) σ	11.11	11.11	11.07	11.11	11.13	11.10
(6.10i) σ	5.75	6.02	5.94	5.70	5.70	5.84
(6.10ii) σ	10.59	11.75	11.50	10.05	7.84	5.91

Table 6.4 Standard deviation of raw data for each output block of Figures 6.7 to 6.10.

Section 6.5 Correction of Residual Scalloping Caused by Saturation

Using the relationship between power loss and standard deviation shown in Figure 6.4, and the conclusions of the raw data simulation from the previous section, correction of the residue scalloping should be possible by adjusting the mean power of each output block. This method is tested on the Nova Scotia(A) scene (Figure 5.9). This scene has the highest raw data saturation and lowest contrast in features, and therefore shows a significant degree of residual scalloping (up to 0.4 *dB*) even after the basic correction.

Two operations per range line are required to correct the scalloping resulting from raw data saturation. The first operation is the calculation of the standard deviation for each range block. To get an accurate representation of the standard deviation it must be calculated over a number of range lines. The optimum number of range lines over which the standard deviation is calculated depends on how fast the scene content is changing.The second operation is to either calculate, or find the power loss associated with the standard deviation from a lookup table, and correct the output block by multiplication with the inverse of the power loss value.

A practical method to calculate the standard deviation of each raw data block during processing must be devised. For the purpose of testing this correction method, however, the

mean raw data standard deviation of each block is calculated over the entire 5000 range lines. Using the value of standard deviation for each block, the power loss value is found from Figure 6.4. Each output block is then multiplied by the inverse power loss value.

Figure 6.11 shows the averaged range-compressed output before correction, after the chirp replica correction, and after the residue scalloping correction.

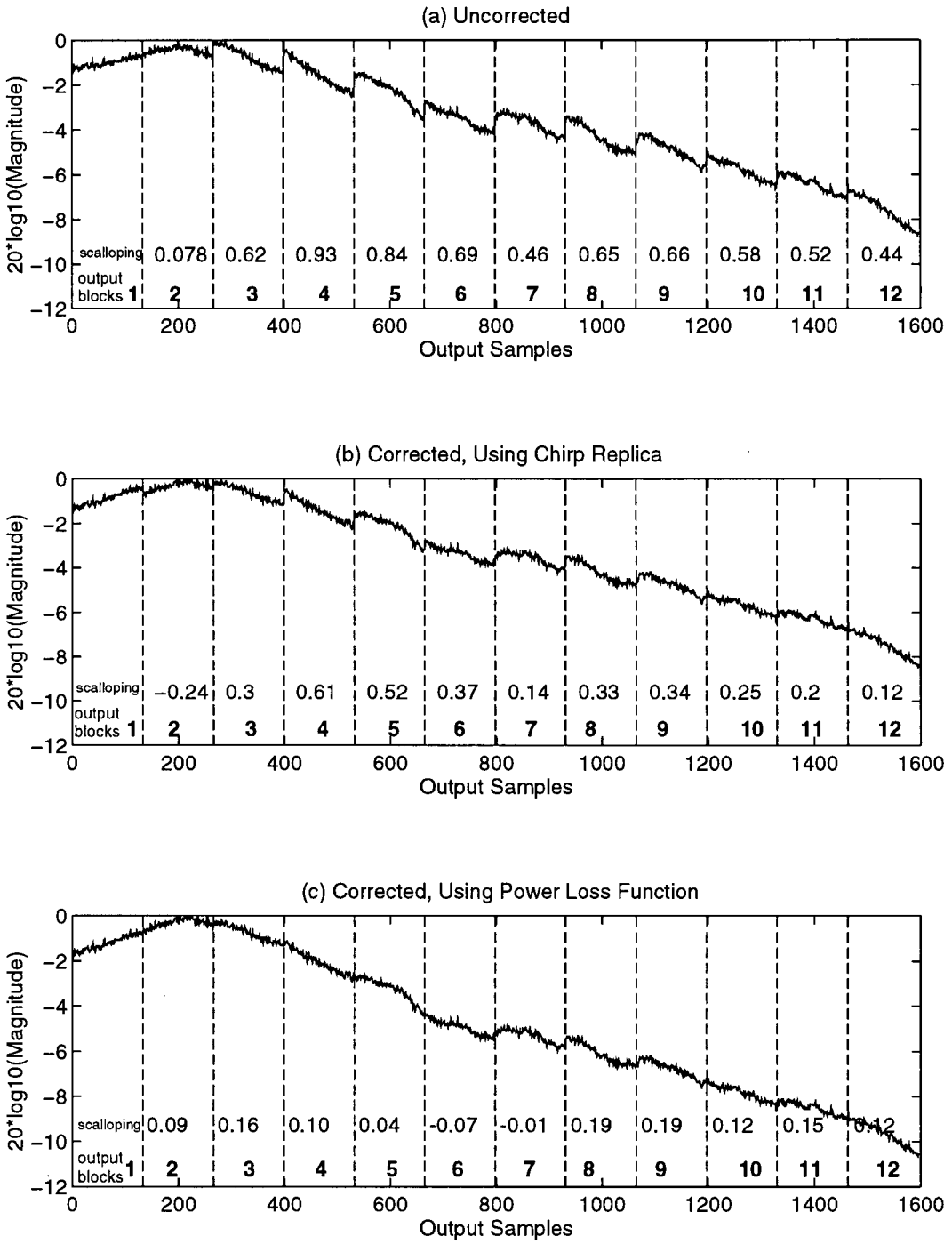

Figure 6.11 Averaged 5000 range processed lines of Nova Scotia ocean(A).

The result in 6.11c shows a maximum improvement of 0.83 *dB* in block 4 which showed the most degree of scalloping before correction. The most amount of remaining scalloping is seen in blocks 8 and 9. This could in part be due to the way the correction is implemented. The

average standard deviation of the blocks over the entire 5000 range lines is used to calculate the amount of power loss. The relationship between the power loss and the standard deviation is quadratic (see Figure 6.4); therefore if the standard deviation of the raw data has changed by a significant amount in the course of these 5000 lines the corresponding power loss (from the look-up table) will not reflect the average power loss. In this case the objective was to show that a relationship between power loss and standard deviation exists and that compensating for the power loss will significantly reduce SPECAN scalloping; this is illustrated by Figure 6.11.

Chapter 7 Discussion

Section 7.1 Summary

This thesis summarizes the work done in improving the range image quality of SAR data processed using the SPECAN algorithm. This algorithm provides a unique method of efficiently producing SAR images, by processing only chosen segments of the raw data and discarding the rest. The drawback to using the algorithm has been the scalloping problem in both the range and azimuth dimensions. The azimuth scalloping has been effectively dealt with; this thesis is concerned with reducing the range scalloping to an acceptable level.

The work that must be done to effectively eliminate range scalloping can be divided into two parts. First is correction of the basic scalloping which is due to the transmitted signal envelope. Second is correction of the residual scalloping seen in some scenes which is due to the combination of gaps in the raw data, raw data saturation, and range attenuation.

The basic scalloping is due to the fact that look frequencies vary with time, which allows the amplitude of each output block to be affected by the envelope of the transmitted chirp. The non-idealities of the transmitted chirp profile will cause distortion in the amplitude of the output block. When the output blocks are put together to form the image, the amplitude distortion is seen as a repeating pattern of light and dark bands across the image. By estimating the amplitude of the transmitted chirp the effect of the distortion on each output block can reversed. In the ERS-1 satellite, a copy of the transmitted signal is recorded to be used for range compression. This replica is used to estimate the envelope of the transmitted chirp and the SPECAN correction function. In low saturation scenes the basic correction method reduces the scalloping from (approximately) 0.5 *dB* to 0.1 *dB*.

The correction described above does not completely eliminate scalloping in all scenes. The key cause of the residual scalloping is that the data chosen for the compression process is from disjointed sections of the raw data. This, combined with raw data saturation and range attenuation, amplifies the scalloping effect in some scenes. In high reflectivity scenes, such as those of the ocean, the raw data is highly saturated in near range where the received signal is strongest. As the received signal power decreases with range, the degree of saturation also decreases. Correspondingly, images from these areas show a high degree of scalloping in near range which gradually decreases to a negligible amount in far range. In sections of the scene with significant raw data saturation the basic correction method reduces the scalloping from (approximately) 1.1 *dB* to 0.7 *dB*.

To see how the range attenuation can cause extra scalloping we must consider that the main effect of saturation is a loss of power in the saturated output compared to the ideal output. This power loss varies across range according to the degree of saturation. As each processing block is chosen from a different part of the raw data, each block has a different power loss from adjacent blocks. This power loss difference is seen as a sudden amplitude gain between adjacent output blocks increasing the scalloping effect.

To correct for the effect of raw data saturation on scalloping, a relationship is drawn between the degree of saturation and the expected power loss in random Gaussian data. Using this function and the average saturation of each SPECAN range block for one processed scene, the power loss for each output range block is predicted and compensated for. This procedure was performed for one of the scenes in this study which showed the highest degree of residual scalloping. The results showed that this method, combined with the basic scalloping correction, can reduce the scalloping to negligible amounts.

Section 7.2 Future Work

The basic scalloping has been largely eliminated by the correction method of Chapter 4. The extra scalloping seen in high reflectivity scenes is a result of raw data saturation. Raw data saturation also causes power loss in images and is identified as the major source of errors in SAR calibration (Laur [37]). To reduce these problems, future remote sensing satellites should be built with more quantization levels in the analogue-to-digital converter. In the worst case of saturation seen in the ERS-1 data the standard deviation of the raw data had increased from 5 (which corresponds to no saturation) to 11. For a standard deviation of 11, 64 distinct levels, corresponding to 6 bits, would be enough to decrease the saturation to less than 1%.

To reduce saturation with the current 32 quantization levels the receiver gain must be reduced. The receiver amplifies the signal before it reaches the ADC. The strength of the signal from high reflectivity areas has been underestimated in the ERS-1 receiver, and the gain levels have been set such that the received signals' range is far higher than the ADC dynamic range. The ERS-1 data should be used in future designs to gain a more accurate estimate of the dynamic range of the received signal.

To continue using the SPECAN algorithm on ERS-1 data, the correction tested in Section 6.5 can be expanded into an efficient algorithm which will measure the standard deviation of each range block, and using a lookup table estimate and compensate for the power loss of the block by a scaling operation. The effectiveness of this correction method should be tested on different scenes. In cases where the raw data is known to be from land or areas with low backscattering this correction should be bypassed by the operator.

In general, scalloping in high contrast scenes cannot be detected by the human eye. In scenes of homogeneous areas, however, the scalloping is quite noticeable and can be corrected using the chirp replica. The chirp replica correction is not computationally intensive, and it is worthwhile

to correct all scenes using this method. In homogeneous scenes with raw data saturation, the scalloping is very high and cannot be compensated for by the chirp replica. In these scenes the scalloping can be removed by estimating, and compensating for, the power loss. Because raw SAR data has a Gaussian distribution, the power loss can be predicted by measuring the standard deviation of the data. This procedure must be integrated in the SPECAN processor by an efficient and practical algorithm.

Bibliography

[1] I. G. Cumming, "Spectral Analysis Approach to the Compression of Linear FM Signals," Tech. Rep. TN-79–276–003, MacDonald Dettwiler and Associates, Ltd., Dec. 1979.

[2] ESA, "Method and Apparatus for Processing Data Generated by a Synthetic Aperture Radar," *European Patent #0048704, Assigned to European Space Agency, Filed September 15, 1981, Granted February 20*, 1985.

[3] S. D. Wall and K. W. Ledbetter, *Design of Mission Operations Systems for Scientific Remote Sensing*. Burgess Science Press, Basingstoke, GB, 1991.

[4] S. A. Hovanessian, *Introduction to Sensor Systems*. Artech House, Inc., Norwood, MA, 1988.

[5] W. G. Rees, *Physical Principles of Remote Sensing*. Cambridge University Press, 1990.

[6] W. T. K. Johnson and A. T. Edgerton, "Venus Radar Mapper – Multimode Radar System Design," *SPIE – The International Society for Optical Engineering*, no. 589, pp. 158–164, Nov. 1985.

[7] R. Francis, "The ERS-1 Spacecraft and its Payload," *ESA Bulletin*, vol. 65, pp. 27–48, Feb. 1991.

[8] K. Tomiyasu, "Tutorial Review of Synthetic Aperture Radar (SAR) with Applications to Imaging of the Ocean Surface," *Proceedings of the IEEE*, vol. 66, no. 5, pp. 563–583, May 1978.

[9] F. T. Ulaby, R. K. Moore, and A. K. Fung, *Microwave Remote Sensing*, vol. 2. Addison-Wesley Publishing Company, 1982.

[10] C. Elachi, T. Bicknell, R. L. Jordan, and C. Wu, "Spaceborne Synthetic-Aperture Imaging Radars: Applications, Techniques, and Technology," *Proceedings of the IEEE*, vol. 70, no. 10, pp. 1174–1196, Oct. 1982.

[11] F. T. Ulaby and C. Elachi, *Radar Polarimetry for Geoscience Applications*. Artech House, Inc., Norwood, MA, 1990.

[12] L. C. Graham, "Synthetic Interferometer Radar for Topographic Mapping," *Proceedings of the IEEE*, vol. 62, no. 6, pp. 763–8, June 1974.

[13] H. A. Zebker, R. P. Salazar, and T. H. Dixon, "Mapping the World's Topography Using Radar Interferometry: the TOPSAR Mission," *Proceedings of the IEEE*, vol. 82, no. 12, pp. 1774–86, December 1994.

[14] J. C. Kirk, "A Discussion of Digital Processing in Synthetic Aperture Radar," *IEEE Transactions on Aerospace and Electronic Systems*, vol. AES-11, no. 3, pp. 326–337, 1975.

[15] S. R. Brooks, H. Joyce, F. G. Sawyer, and D. J. Smith, "The ERS-1 Synthetic Aperture Radar and Scatterometer," *GEC Journal of Research*, vol. 3, no. 2, pp. 124–36, 1985.

[16] S. J. Austin, D. J. Q. Carter, and J. D. McCaughey, "ERS-1 Spacecraft - Active Microwave Instrumentation: A Major Achievement," *GEC Journal of Research*, vol. 9, no. 1, pp. 2–12, 1991.

[17] D. C. Munson and R. L. Visentin, "A Signal Processing View of Strip-Mapping Synthetic Aperture Radar," *IEEE Transactions on Acoustics, Speech, and Signal Processing*, vol. 37, no. 12, pp. 2131–2147, Dec. 1989.

[18] S. Marcus, B. D. Colella, and T. J. Green, "Solid-state Laser Synthetic Aperture Radar," *Applied Optics*, vol. 33, no. 6, pp. 960–4, Feb. 1994.

[19] J. C. Curlander and R. N. McDonough, *Synthetic Aperture Radar, Systems and Signal Processing*. John Wiley & Sons, Inc., Toronto, 1991.

[20] D. J. Bonfield and J. R. E. Thomas, "Synthetic Aperture Radar Real-time Processing," *IEE Proceedings*, vol. 127, no. 2, pp. 155–159, April 1980.

[21] N. Levanon, *Radar Principles*. John Wiley & Sons, Inc., New York, 1988.

[22] A. H. Nuttal, "Some Windows with Very Good Sidelobe Behaviour," *IEEE Transactions on Acoustics, Speech and Signal Processing*, vol. ASSP-29, no. 1, pp. 84–91, Feb. 1981.

[23] J. R. Bennett, I. G. Cumming, and R. A. Deane, "The Digital Processing of Seasat Synthetic Aperture Radar Data," *IEEE International Radar Conference*, pp. 168–191, April 1980.

[24] C. Wu, K. Y. Lin, and M. Jin, "Modelling and a Correlation Algorithm for Spaceborne SAR Signals," *IEEE Transactions, AES-18*, pp. 563–574, 1982.

[25] L. Chunsheng, L. Jingwen, and Z. Yinqing, "Azimuth Digital Signal Processing Algorithms for Spaceborne SAR," *International Conference on Circuits and Systems*, pp. 475–7, June 1991.

[26] J. E. Harris, S. O. Randall, D. M. Chabries, and R. Christiansen, "Quality Measures for SAR Images," pp. 1064–7.

[27] R. Schotter, R. Gunzenhauser, and H. Holzl, "Real Time SAR Processor," *International Geoscience and Remote Sensing Symposium (IGARSS)*, vol. 2, pp. 2.1–2.6, 1982.

[28] "The Construction and Testing of a Real-Time Digital Breadboard Processor for the ESA Remote Sensing Satellite Synthetic Aperture Radar," Tech. Rep. 00–0778, MacDonald Dettwiler and Associates, Ltd., Dec. 1984.

[29] "Brazil Quicklook SAR Processor High-Level Design," Tech. Rep. BZ-DS-50–2733, MacDonald Dettwiler and Associates, Ltd., Jan. 29, 1992.

[30] "A Doppler Centroid Estimation Algorithm for the Processing of ScanSAR Data: Preliminary Analysis and Results," Tech. Rep. RC-TN-MDA-SY-0002, MacDonald Dettwiler and Associates, Ltd., April 18, 1988.

[31] W. J. Caputi, "Stretch: A Time Transformation Technique," *IEEE Transactions on Aerospace and Electronic Systems*, vol. 7, no. 2, pp. 269–278, March 1971.

[32] A. V. Oppenheim and R. W. Schaffer, *Discrete-Time Signal Processing*. Prentice-Hall International, Englewood Cliffs, New Jersey, 1989.

[33] A. Freeman, "SAR Calibration: An Overview," *IEEE Transactions on Geoscience and Remote Sensing*, vol. 30, no. 6, pp. 1107–1121, Nov. 1992.

[34] R. C. Gonzalez and R. E. Woods, *Digital Image Processing*. Addison-Wesley Publishing Company, Don Mills, Ontario, 1992.

[35] D. J. Q. Carter and S. Hartley, "ERS-1 Active Microwave Instrumentation Engineering Model Performance," *International Geoscience and Remote Sensing Symposium (IGARSS)*, vol. 2, pp. 867–70, Sep 1988.

[36] R. J. Blisset and F. G. Sawyer, "ERS-1 SAR Performance Verification," *GEC Journal of Research*, vol. 4, no. 1, pp. 47–56, 1986.

[37] H. Laur, P. Meadows, J. I. Sanchez, and E. Dwyer, "ERS-1 SAR Radiometric Calibration," *SAR Calibration Workshop Proceedings*, pp. 257–81, 20–24 Sep. 1993.

[38] G. A. Gray and G. W. Zeoli, "Quantization and Saturation Noise Due to Analog-to-Digital Conversion," *IEEE Transactions on Aerospace and Electronic Systems*, pp. 222–3, Jan. 1971.

[39] B. E. Richards and D. C. Lancashire, "The Impacts of Quantization Noise on the ERS-1 Synthetic Aperture Radar Performance," *International Geoscience and Remote Sensing Symposium (IGARSS)*, vol. 2, pp. 1159–61, September 1988.

[40] G. Franceschetti, M. Migliaccio, D. Riccio, and G. Schirinzi, "SARAS: A Synthetic Aperture Radar (SAR) Raw Signal Simulator," *IEEE Transactions on Geoscience and Remote Sensing*, vol. 30, no. 1, pp. 110–123, January 1992.

[41] R. K. Hawkins, C. E. Livingstone, A. L. Gray, R. B. Olsen, J. G. Halbertsma, and R. A. Deane, "CCRS C-Band Airborne Radar: System Description and Test Results," *Proceedings of the 11th Canadian Symposium on Remote Sensing*, pp. 503–515, 1987.

[42] L. D. Teany and R. K. Hawkins, "The CCRS Airborne SAR STC Function," *SAR Calibration Workshop Proceedings*, pp. 177–184, 20–24 Sep. 1993.